

Faculty of Engineering of the University of Porto



**Development of a new computational approach
to simulate blood flow**

Mariana Sousa Santos

Dissertation carried out under the
Integrated Master in Bioengineering
Major Biomedical Engineering

Supervisor: Jorge Belinha, PhD
Co-Supervisor: Renato Natal Jorge, PhD

July 2017

© Mariana Sousa Santos, 2017

Abstract

Cardiovascular diseases are a leading cause in mortality worldwide. Diseases like atherosclerosis and aneurysms disturb the blood flow, leading to clinical complications. The simulation of blood flow is very important to understand the function of the cardiovascular system under normal and abnormal conditions, designing cardiovascular devices, and diagnosing and treating disease.[1] This process has been studied, however, in certain types of blood vessels, like veins, there are few studies.

This project proposes to simulate blood flow using a fully developed meshless method software in two dimension (2D) models and three dimension (3D) models. In opposition to the Finite Element Method (FEM), meshless methods are new discrete numerical methods much more flexible and accurate. Thus, to determine the velocity field, a numerical tool is required. In this work two meshless numerical methods are used, the Radial Point Interpolation Method (RPIM) and the Natural Neighbour Radial Point Interpolation Method (NNRPIM). The velocity profiles and the discharge are used to compare the numerical methods. In end, it is expected to conclude if meshless methods are suited to explicitly simulate blood flow.

For this work, the blood was simulated being a Newtonian fluid, since in large vessels, the non-Newtonian effects are not significant. The work analysed six different 2D models, representing different possible geometries for vessels, and three 3D models, showing different geometries. In the end, several benchmark examples were extracted from literature and compared with FEM and meshless methods. The results show that the meshless methods are suited to simulate blood flow.

Resumo

As doenças cardiovasculares são uma das principais causas de mortalidade no mundo. Doenças como a arteriosclerose e aneurismas causam um distúrbio no fluxo sanguíneo, levando a complicações clínicas. A simulação do fluxo sanguíneo é então muito importante para perceber a função do sistema cardiovascular sobre condições normais e patológicas, desenhar dispositivos cardiovasculares, e diagnosticar e tratar patologias. [1] Este processo já tem vindo a ser estudado, no entanto, em certos tipos de vasos, como veias, ainda existem poucos estudos.

Este projeto propõe simular o fluxo sanguíneo usando um *software* de métodos numéricos sem malha em modelos a duas dimensões (2D) e a três dimensões (3D). Em oposição ao método dos elementos finitos (MEF), os métodos sem malha são novos métodos numéricos discretos muito mais flexíveis e precisos. Portanto, é necessário utilizar uma ferramenta numérica para determinar o campo de velocidades. Neste trabalho dois métodos numéricos irão ser usados, o *Radial Point Interpolation Method* (RPIM) e o *Natural Neighbour Radial Point Interpolation Method* (NNRPIM). Os perfis de velocidades e os caudais são usados para comparar os métodos numéricos. No final, é esperado concluir se os métodos sem malha são adequados para explicitamente simular o fluxo sanguíneo.

Neste trabalho, o sangue foi simulado sendo um fluido Newtoniano, visto que em vasos de alto calibre os efeitos não-Newtonianos são desprezíveis. Este trabalho analisa seis modelos 2D diferentes, representando diferentes geometrias para vasos, e três exemplos 3D, representando diferentes geometrias. No fim, vários exemplos de referência foram retirados da literatura e comparados com FEM e os métodos numéricos sem malha. Os resultados mostram que os métodos sem malha são adequados para simular o fluxo sanguíneo.

Acknowledgements

Um muito obrigado ao orientador, o Professor Jorge Belinha por todo o tempo que dispensou a ajudar-me e por estar sempre pronto a esclarecer quaisquer dúvidas que tivesse.

Estes cinco anos na Faculdade de Engenharia, a qual foi a minha segunda casa, não tinham sido tão fantásticos se não fossem as pessoas que encontrei pelo caminho. Por isso, um grande obrigado os amigos de Bioengenharia que me acompanharam ao longo do tempo.

Um grande obrigado também ao BEST Porto, por todo o crescimento que me proporcionou, em especial neste último ano em que tive o prazer de fazer parte da XXI direção. Queria agradecer em especial ao *management* da associação, por estar sempre presente neste último ano, que sem dúvida tem tido muitos desafios.

Um grande obrigado aqueles que me ajudaram a chegar até aqui, os meus pais, que sempre apoiaram as minhas decisões.

Institutional acknowledgements

The author truly acknowledges the work conditions provided by the Applied Mechanics Division (SMAp) of the department of mechanical engineering (DEMec) of FEUP and by the inter-institutional project “BoneSys - Bone biochemical and biomechanic integrated modeling: addressing remodeling, disease and therapy dynamics” funded by the “Laboratório Associado de Energia Transportes e Aeronáutica” (UID/EMS/50022/2013) and by the project NORTE-01-0145-FEDER- 000022 - SciTech - Science and Technology for Competitive and Sustainable Industries, co-financed by Programa Operacional Regional do Norte (NORTE2020), through Fundo Europeu de Desenvolvimento Regional (FEDER).

“We choose to go to the Moon! ... We choose to go to the Moon in this decade and do the other things, not because they are easy, but because they are hard; because that goal will serve to organize and measure the best of our energies and skills, because that challenge is one that we are willing to accept, one we are unwilling to postpone, and one we intend to win ...”

-John F. Kennedy

Table of contents

Abstract	iii
Resumo	v
Acknowledgements.....	vii
Institutional acknowledgements	ix
Table of contents	xiii
List of figures.....	xv
List of Tables	xxi
Abbreviations and symbols	xxiii
Chapter 1.....	1
Introduction.....	1
1.1 - Motivation.....	1
1.2 - Objectives.....	2
1.3 - Document Structure	2
Chapter 2.....	1
Blood Flow	1
2.1 - Biological description of circulation.....	1
2.2 - Blood constitution	2
2.3 - Mechanical properties	3
2.4- Constitutive/rheological models to simulate blood	4
Chapter 3.....	7
Numerical methods.....	7

3.1 - Finite element method	7
3.2 - Meshless method	7
3.2.1. General meshless method procedure	8
3.2.2. RPIM Formulation.....	9
4.2.3- NNRPIM Formulation	12
3.3 - Discretized formulation flow	17
3.4 - Numerical analysis applied to blood flow	20
Chapter 4	23
Preliminary studies.....	23
4.1- 2D convergence studies	23
4.1.1- Linear model	26
4.1.2- Crescent cone model	35
4.1.3- Cone decrescent model	44
4.1.4- Quarter of a circular crown model	54
4.1.5- Half of a circular crown model.....	63
4.1.6- Double curve model.....	75
4.2- 3D studies.....	82
4.2.1- Linear model	83
4.2.2- Quarter of a crown model	88
4.2.3- Double curve model.....	93
4.2.4- General remarks	97
Chapter 5	99
Case studies	99
5.1 - Comparison with another constitutive model for blood	99
5.2 - Bifurcation.....	101
5.3 - Spastic middle cerebral arteries.....	104
5.4 - Cerebral aneurysm	108
5.5 - Aortic aneurysm	109
5.6 - Real bifurcation.....	112
Chapter 6	113
Conclusions and future work	113
References.....	115

List of figures

Figure 2.1 - Human blood viscosity as a function of shear rate for a range of hemaocrit concentrations on a log-log plot [21][22][23][19]	4
Figure 2.2 - The non-Newtonian fluid models that are commonly used to describe blood rheology [19]	5
Figure 3.1 - a. Problem domain with the essential and natural boundaries applied. b. Regular nodal discretization. c. Irregular nodal discretization.[40]	8
Figure 3.2 - a. Fixed rectangular shaped influence-domain. b. Fixed circular shaped influence-domain. c. Flexible circular shaped influence-domain [40]	9
Figure 3.3 - a. Fitted Gaussian integration mesh. b. General Gaussian integration mesh. c. Voronoï diagram for nodal integration [40]	10
Figure 3.4 - a. Initial quadrilateral from the grid-cell. b. Transformation of the initial quadrilateral into an isoparametric square shape and application of the 2 x 2 quadrature point rule. c Return to the initial quadrilateral shape [40].....	10
Figure 3.5 - a. Initial nodal set of potential neighbour nodes of node n_0 . b. First trial plane. c. Second trial plane. d. Final trial cell containing just the natural neighbours of node n_0 . e. Node n_0 Voronoï cell V_0 . f. Voronoï diagram [40].....	12
Figure 3.6 - a. First degree influence-cell b. Second degree influence-cell [40]	14
Figure 3.7 - a. Voronoï diagram, b. Delaunay triangulation and c. Natural neighbour circumcircles [40]	14
Figure 3.8 - Triangular shape and quadrilateral shape and the respective integration points x_I using the Gauss-Legendre integration scheme [40].....	15
Figure 3.9 - Finite Element and Meshless Analysis Software (FEMAS) - Print-screen of an artery bifurcation and corresponding velocity field.	21

Figure 4.1 - Laminar velocity profile in a tube [45].....	24
Figure 4.2 - Example of the boundary conditions applied.....	25
Figure 4.3- Representation of the nodes in a cross section.....	26
Figure 4.4 - Linear model with different meshes	27
Figure 4.5 - Linear model (21 nodes) analysed with different methods	28
Figure 4.6 - Linear model (65 nodes) analysed with different methods	29
Figure 4.7 - Linear model (255 nodes) analysed with different methods.....	30
Figure 4.8 - Linear model (833 nodes) analysed with different methods.....	31
Figure 4.9 - Linear model (3201 nodes) analysed with FEM (triangular elements with 6 nodes).....	32
Figure 4.10 - Discharge in every cross section of the models	32
Figure 4.11 - Discharge in each cross session with different methodologies	34
Figure 4.12 - Velocity profiles in each cross session with different methodologies	35
Figure 4.13 - Crescent cone model with different meshes	36
Figure 4.14 - Cone crescent model (21 nodes) analysed with different methods.....	37
Figure 4.15 - Cone crescent model (65 nodes) analysed with different methods.....	38
Figure 4.16 - Cone crescent model (255 nodes) analysed with different methods	39
Figure 4.17 - Cone crescent model (833 nodes) analysed with different methods	40
Figure 4.18 - Cone crescent model (3201 nodes) analysed with FEM (triangular elements with 6 nodes)	41
Figure 4.19 - Discharge in every cross section of the models	41
Figure 4.20 - Discharge in each cross session with different methodologies	43
Figure 4.21 - Velocity profiles in each cross session with different methodologies	44
Figure 4.22 - Decrescent cone model with different meshes.....	45
Figure 4.23 - Cone decrescent model (21 nodes) analysed with different methods	46
Figure 4.24 - Cone decrescent model (65 nodes) analysed with different methods	47
Figure 4.25 - Cone decrescent model (225 nodes) analysed with different methods	48

Figure 4.26 - Cone decrescent model (833 nodes) analysed with different methods	49
Figure 4.27 - Cone decrescent model (3201 nodes) analysed with FEM (triangular elements with 6 nodes).....	49
Figure 4.28 - Discharge in every cross section of the models	50
Figure 4.29 - Discharge in each cross session with different methodologies.....	52
Figure 4.30 - Velocity profiles in each cross session with different methodologies	53
Figure 4.31 - Quarter of a circular crown model with different meshes.....	54
Figure 4.32 - Quarter of a circular crown model (21 nodes) analysed with different methods.....	55
Figure 4.33 - Quarter of a circular crown model (65 nodes) analysed with different methods.....	56
Figure 4.34 - Quarter of a circular crown model (255 nodes) analysed with different methods.....	57
Figure 4.35 - Quarter of a circular crown model (833 nodes) analysed with different methods.....	58
Figure 4.36 - Quarter of a circular crown model (3201 nodes) analysed with FEM (triangular elements with 6 nodes)	59
Figure 4.37 - Discharge in every cross section of the models	59
Figure 4.38 - Cross sections	60
Figure 4.39 - Discharge in each cross session with different methodologies.....	61
Figure 4.40 - Velocity profiles in each cross session with different methodologies	63
Figure 4.41 - Distortion of the axial velocity profile as a result of tube curvature [47]	63
Figure 4.42- Half of a circular crown model with different meshes	64
Figure 4.43 - Half of a circular crown model (75 nodes) analysed with different methods ..	66
Figure 4.44 - Half of a circular crown model (125 nodes) analysed with different methods	66
Figure 4.45 - Half of a circular crown model (441 nodes) analysed with different methods	67
Figure 4.46 - Half of a circular crown model (1659 nodes) analysed with different methods	68

Figure 4.47 - Discharge in every cross section of the models	69
Figure 4.48 - Cross sections in half of a crown model	69
Figure 4.49 - Velocity profiles in each cross session with different methodologies	72
Figure 4.50 - Discharge in each cross session with different methodologies	74
Figure 4.51 Double curve model with different meshes.....	75
Figure 4.52 - Double curve model (75 nodes) analysed with different methods	76
Figure 4.53 - Double curve model (245 nodes) analysed with different methods.....	77
Figure 4.54 - Double curve model (873 nodes) analysed with different methods.....	78
Figure 4.55 - Double curve model (3281 nodes) analysed with different methods	79
Figure 4.56 - Cross sections in the double curve model	79
Figure 4.57 - Discharge in every cross section of the models	80
Figure 4.58 - Velocity profiles in each cross session with different methodologies.....	81
Figure 4.59 - Discharge in each cross session with different methodologies	82
Figure 4.60 - Linear 3D model.....	83
Figure 4.61 - Linear 3D model FEM analysis.....	85
Figure 4.62 - Linear 3D model FEM analysis - cross section views	85
Figure 4.63 - Linear 3D model NNRPIM analysis	86
Figure 4.64 - Linear 3D model NNRPIM analysis	86
Figure 4.65 - Linear 3D model RPIM analysis.....	87
Figure 4.66 - Linear 3D model NNRPIM analysis	87
Figure 4.67 - Quarter circular crown model	88
Figure 4.68 - Quarter circular crown model analysed with FEM.....	90
Figure 4.69 - Quarter circular crown model analysed with NNRPIM	91
Figure 4.70 - Quarter circular crown model analysed with RPIM.....	92
Figure 4.71 - Double curve model	93
Figure 4.72 - Double curve model analysed with FEM.....	94

Figure 4.73 - Double curve model analysed with RPIM	95
Figure 4.74 - Double curve model analysed with RPIM	96
Figure 5.1 - Velocity field for the Carreau model for inlet centre line velocities of 0.8 m/s [48].....	99
Figure 5.2 - Reproduced model	100
Figure 5.3 - Comparison in [48] between the velocity profiles expected	100
Figure 5.4 - Numerical analysis of model	100
Figure 5.5 - Bifurcation models	101
Figure 5.6 - Numerical analysis of model with the initial constant velocity.....	103
Figure 5.7 - Numerical analysis of model with the parabolic initial velocity.....	104
Figure 5.8 - Results presented in literature	105
Figure 5.9 - Numerical analysis of model	107
Figure 5.10 - Numerical analysis of model.....	107
Figure 5.11 - Results presented in paper	108
Figure 5.12 - Numerical analysis of model.....	109
Figure 5.13 - Results presented in paper	110
Figure 5.14 - Numerical analysis of model.....	111
Figure 5.15 - Numerical analysis of model.....	112

List of Tables

Table 2.1 - Human blood composition [18].....	2
Table 4.1 - Default RPIM and NNPIM used in the analysis	25
Table 4.2 - RPIM and NNPIM parameters in the linear 3D model	84
Table 4.3 - RPIM and NNPIM parameters in the quarter circular crown 3D model	89
Table 4.4 - RPIM and NNPIM parameters in the half circular crown 3D model	94
Table 5.1 - RPIM and NNPIM parameters in the bifurcation model with constant velocity profile	102
Table 5.2 - RPIM and NNPIM parameters in the bifurcation model with parabolic velocity profile	102
Table 5.3 - RPIM and NNPIM parameters in the spastic middle cerebral artery model (a)..	105
Table 5.4 - RPIM and NNPIM parameters in the spastic middle cerebral artery model (b) .	106
Table 5.5 - RPIM and NNPIM parameters in cerebral aneurism	108
Table 5.6 - RPIM and NNPIM parameters in aortic aneurism.....	110

Abbreviations and symbols

List of abbreviations

DVT	Deep Venous Thrombosis
FEM	Finite Element Methods
FEMAS	Finite Element and Meshless Analysis Software
FPM	Finite Point Methods
MLPG	Meshless Local Petrov-Galerkin
MQ	Multiquadric
NNRPIM	Natural Neighbor Radial Point Interpolation Method
RPI	Radial Point Interpolation Method
RBF	Radial Basis Functions
RPI	Radial Point Interpolation
RPI	Real Property Information Model
SPH	Smooth Particle Hydrodynamics
CVD	Cardiovascular diseases

List of symbols

α	penalty factor
γ	fluidity parameter
δ	Identity matrix
ε	strain
μ	viscosity
ρ	density
σ	stress
τ	torsion
ω	weight of the integration points
$\dot{\gamma}$	shear rate

$\dot{\gamma}_c$	characteristic shear rate
$\dot{\gamma}$	rate of strain tensor
λ	characteristic time constant
λ_1	relaxation time
λ_2	retardation time
μ	fluid viscosity
μ_p	plasma viscosity
μ_0	zero-shear-rate viscosity
μ_∞	infinite-shear-rate viscosity τ
τ	shear stress
$\boldsymbol{\tau}$	stress tensor
τ_c	characteristic shear stress
τ_0	yield-stress
Φ	volume concentration
a	Carreau-Yasuda index
k	consistency coefficient
k_0	maximum volume fraction for zero shear rate
k_∞	maximum volume fraction for infinite shear rate
m	Cross model index
n	power law index
∇	upper convected time derivative

Chapter 1

Introduction

1.1 - Motivation

The cardiovascular system and its well function is vital for human beings to carry their daily lives. But, despite the development in healthcare systems over the past few decades, cardiovascular disease is still a worrying problem.

Cardiovascular disease (CVD) is the leading cause of death worldwide[2], accounting for one-third of global deaths. [3] Just in Europe, CVD causes 3.9 million deaths and over 1.8 million deaths in the European Union (EU).[4]

Besides the mortality, there are several life conditions that can affect the quality of life of people with chronic CVD.[5][6][7] This results in substantial disability and loss of productivity and contributes to the escalating costs of health care.[4]

Due to the aging population and to classical risk factors, namely diets high in saturated fats, elevated serum cholesterol and blood pressure (BP), diabetes, and smoking, [8] in 2015, more than 85 million people in Europe were living with CVD and almost 49 million people were living with CVD in the EU. [4]

Overall CVD is estimated to cost the EU economy €210 billion a year. Of the total cost of CVD in the EU, around 53% (€111 billion) is due to health care costs, 26% (€54 billion) to productivity losses and 21% (€45 billion) to the informal care of people with CVD.[4]

The aging population and the unhealthy habits have brought some challenges to the national health systems from all over the world, so it is necessary to develop strategies to make prevention, diagnosis and treatment more efficient.

The simulation of blood flow is very important to understand the function of the cardiovascular system under normal and abnormal conditions, designing cardiovascular devices, diagnosing and treating disease.[1] It is established that blood disturbances can lead to clinical complications in areas of complex flow, like in coronary and carotid bifurcations or stenosed arteries. [9] This methods allow, in a non-intrusive virtual manner, the estimation of a multitude of blood flow characteristics.[10]

There are some cases where this study can be important. Cerebral aneurysm rupture, leading to subarachnoidal hemorrhage accounts for approximately 7% of all strokes. [10] Aortic aneurysms are a main cause of death in the elderly population throughout the western world [11] and deep vein thrombosis is also the leading cause of preventable hospital death[12], [13] and a leading cause of maternal mortality in the U.S. [14] Coronary heart disease caused by

atherosclerosis is the major cause of mortality from cardiovascular disease in much of the world's population, which is the leading cause of death in the United States[15][16]

Understanding how the blood flow works in several situations has been studied with several numerical methods, however, the study with meshless methods is still much unexplored. Hence this thesis aims to create a reliable biomechanical simulation of the blood flow with RPIM and NNRPIMM.

1.2 - Objectives

The main objective of this project is to develop a new computational approach to simulate blood flow.

Therefore, to accomplish this goal, several secondary objectives were stipulated, such as:

- Perform a steady flow analysis of the blood flow, using the two of the most recent meshless models nowadays, the RPIM and NNRPIM;
- Study the effect of different geometries in the velocity map of blood flow
- Draw comparisons between FEM and the meshless methods used.

1.3 - Document Structure

This thesis is composed of seven major chapters: Introduction, Blood Flow, Numerical methods, The modelling and analysis process, Preliminary studies, Case studies and Conclusions and future work.

In Chapter 1, **Introduction**, a brief introduction and the motivation to carry this work is explained. The goals of this work are as well stated in this chapter.

In Chapter 2, **Blood Flow**, a biological description of the cardiovascular system, the blood constitution and its mechanical properties is given and different constitutive and rheological models to simulate blood.

In Chapter 3, **Numerical methods**, it is explained the two meshless methods in this work and the flow formulation for viscoplastic materials used in this work.

In Chapter 4, **Preliminary studies**, it is performed a study to compare the different numerical methods, different levels of discretization and different geometries. Afterwards, it was performed a 3D study with the three methods.

In Chapter 5, **Case studies**, some examples found in scientific papers are reproduced and compared with the results from FEM and meshless methods.

In Chapter 6, **Conclusions and future work**, the main conclusion of this work is presented and some recommendations for future work in the topic are given.

Chapter 2

Blood Flow

2.1 - Biological description of circulation

The circulatory system is a system that permits blood to circulate and transport essential molecules for the well-functioning of the human body. It needs to provide adequate continuous flow and regulate it according to the body's needs [17]. The cardiovascular system consists of the heart, blood vessels, and blood.

The heart is a muscle pumping blood throughout the entire cardiovascular system. It is composed of two separate pumps that work to transport blood through the vascular system. One of these pumps (left side) delivers oxygenated blood to the body, while the other pump (right side) delivers deoxygenated blood to the lungs. [18]

The vasculature consists of arteries, arterioles, capillaries, venules, and veins. The vasculature is normally divided into two parts: the pulmonary and systemic circulations. The network of blood vessels from the right heart to the lungs and back to the left heart is referred to as the pulmonary circulation system, and the rest of the blood flow loop is called the systemic circulation system. Blood is pumped at a rate of 5.2 litres per minute [17].

Blood flows through large arteries, then branches into smaller arteries, before reaching arterioles and capillaries. After capillaries, and before reaching the right heart, the blood enters the venules before joining smaller veins first and then larger veins. The pressure gradient developed between the arterial and the venous end of the circulation is the driving force causing blood flow through the blood vessels. [17]

The main functions of the cardiovascular system are the distribution of oxygen (acquired from the lungs) and nutrients (acquired from the intestine) to the cells in all parts of the body, elimination of cellular wastes and carbon dioxide from the cells (excreted through the kidneys) and maintain the homeostasis. [17]

2.2 - Blood constitution

Blood is composed of two major components: the cellular component and the plasma component (see Table 2.1). In an average adult, the blood volume is approximately 5 L, of which approximately 55% to 60% is plasma and the remaining portion is cellular. More than 99% of the cellular component is composed of red blood cells. [18] The remaining portion of the cellular volume (less than 1%) is composed of white blood cells and platelets.

Table 2.1 - Human blood composition [18]

Cellular Component (~ 40%)	Cell type	Cell concentration	Characteristic Shape/Dimensions
	Red Blood Cell (Erythrocyte - ~99.7%)	~5,000,000/ μ L	Biconcave Discs 8 μ m Diameter 2.5 μ m Thickness
	White Blood Cell (Leukocyte - ~0.2%)	~7,500/ μ L	Spherical 20-100 μ m Diameter
	Platelet (Thrombocyte - ~0.1%)	~250,000/ μ L	Ellipsoid 4 μ m Long Axis 1.5 μ m Short Axis
Plasma component (~ 60%)	Composition	Major contributors	Function
	Water (~92%)	H ₂ O	Reduce Viscosity
	Plasma Proteins (~7%)	Albumin (~60%) Globulins (~35%) Fibrinogen (~3%) Others (~2%)	Osmotic Pressure Immune Function Clotting Enzymes/Hormones
	Other Solutes (~1%)	Electrolytes Nutrients Wastes	Homeostasis Cellular Energy Excretion

Red blood cells (or erythrocytes) are responsible for the delivery of oxygen and the removal of carbon dioxide from all cells of the body through hemoglobin and the maintenance of the blood pH, using hemoglobin as a buffer. The shape of red blood cells can change for these cells to squeeze through capillaries. [18]

White blood cells (or leukocytes) are the primary cells that protect the body from foreign particles. They can directly destroy foreign particles or produce antibodies that aid in the immune response. There are six types of white blood cells (neutrophils, lymphocytes, monocytes, eosinophils, basophils, and plasma cells) in the body, each with its own specialized function. [18]

Of those cells, neutrophils account for more than 60% of them, lymphocytes account for approximately 30%, monocytes account for approximately 5%, eosinophils account for approximately 2.5%, basophils account for 0.5%, and plasma cells approximately 0.1%. [18]

Platelets (or thrombocytes) are the primary cells for hemostasis. They are cellular fragments of megakaryocytes, which are derived from hematopoietic stem cells. Platelets do not contain nuclei or many of the other common cellular organelles, and contain anti-thrombotic proteins that cleave activated zymogens. The shear stress can alter the platelet physiology significantly. Under disturbed blood flow conditions (e.g., high shear stresses, recirculation zones, oscillating stresses), platelets may accelerate cardiovascular disease progression. [18] An abnormal number of platelets can lead to coagulation problems.

Plasma is the second major component of blood. Its main composition is water, electrolytes, sugars, urea, phospholipids, cholesterol, and proteins. [18]

Approximately 2% of this is accounted for by sugars within the plasma. Cholesterol contributes 4% to 5% of those (in a normal diet) and phospholipids are approximately 6% to 7% of those. Proteins account for 7% of the total composition of plasma. The most crucial and most abundant protein within the blood is albumin, which accounts for over 60% of the total plasma protein concentration. Albumin has the primary function of maintaining the osmotic pressure of blood. It acts to balance the mass transfer across the capillary wall. Antibodies play a role in immunology and transport globulins can bind to hormones, metallic ions, and steroids, among others, to transport these molecules throughout the body. The remaining plasma protein composition is made up of fibrinogen (approximately 3%) and all the other proteins. Fibrinogen is the precursor to fibrin and forms a mesh during clot formation. [18]

In general, the water portion of plasma is used to reduce the viscosity of the cellular component of blood, reducing the flow resistance and allowing blood flow to occur. A major function of the remaining plasma components is to maintain equilibrium with the interstitial space, which aids in homeostasis. Sugars are used as the nutrient source for cells. Cholesterol can be used within the cell membrane to increase its rigidity so the cell can withstand forces better. Proteins have specific functions and each protein may have a different task. Therefore, plasma has a very critical function for the human body. [18]

2.3 - Mechanical properties

Blood is a special non-Newtonian fluid that is also composed of at least two phases. The rheological characteristics of blood are determined by all its properties and their interaction with each other, as well as with the surrounding structures. The properties of a non-Newtonian fluid include deformation rate dependency, viscoelasticity, yield stress and thixotropy. Most non-Newtonian effects originate from red blood cells due to their high concentration and distinguishes mechanical properties such as elasticity and ability to aggregate forming three-dimensional structures at low deformation rates. [19]

Blood is a thixotropic fluid because its apparent viscosity decreases under a constant shear stress. [18]

Non-Newtonian effects in general are seen in certain flow regimes, such as low shear rates and are influenced by the type of deformation.[19]

Blood is a predominantly shear thinning fluid, especially under steady flow conditions. At low shear rates or shear stresses the apparent viscosity is high, whereas the apparent viscosity decreases with increasing shear. [20]

Yield stress contributes to the blood clotting following injuries and subsequent healing, and may also contribute to the formation of blood clots (thrombosis) and vessel blockage in some pathological cases such as strokes.[19]

The viscosity of whole blood varies with shear rate, haematocrit (see Figure 2.1), temperature, and disease conditions, and this is predominantly due to the presence of cells and other compounds within the fluid.[18]

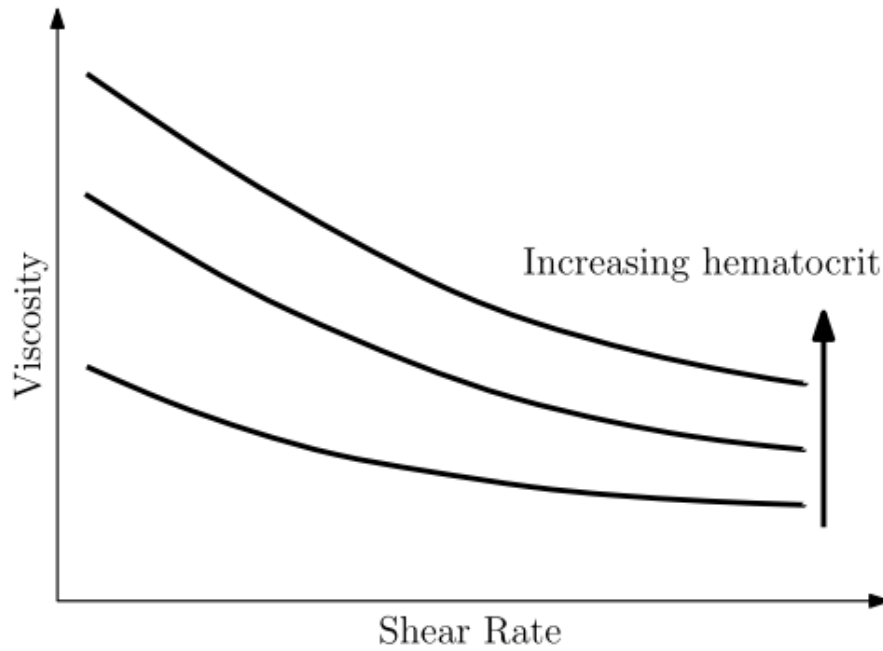


Figure 2.1 - Human blood viscosity as a function of shear rate for a range of hemaocrit concentrations on a log-log plot [21][22][23][19]

At stasis, normal blood has a yield stress of about 2 to 4 mPa [24][20]. The value of blood viscosity ranges from 3.01 to 5.53 cP [17], corresponding to 3.01 to 5.53 mPa.s, and has a density 1060 kg/m³[25][26].

These values result from experimental studies. There are several models that can modulate the behaviour of blood. The model used will be presented later in the chapter “Numerical analysis of blood and coagulation”.

2.4- Constitutive/rheological models to simulate blood

As discussed before, blood is a non-Newtonian fluid. In literature, there were several models used including Carreau-Yasuda, Casson, power law, Cross, Herschel, Oldroyd-B, Quemada, Yelleswarapu, Bingham, Eyring-Powell, and Ree-Eyring. The more frequent used models are Casson and Carreau-Yasuda models. [19]

Blood can be modulated as a Newtonian fluid, which can be applied in large vessels at medium and high shear rates under non-pathological conditions. This is due to the fact that blood is exposed to relatively high shear rates and non-Newtonian effects are induced at low shear rates ($<100 \text{ s}^{-1}$). In the venous part of the circulatory system, the Newtonian effects are more significant than in the arterial part due to low deformation rates.[19]

None of the mentioned models are capable to reproduce accurately all the features and properties of blood flow.[44]

The Figure 2.2 represents the equations of the rheological models and the non-Newtonian properties that are used in literature to simulate the blood flow.

Model	Equation	Non-Newtonian Properties
Carreau-Yasuda	$\mu = \mu_{\infty} + \frac{\mu_0 - \mu_{\infty}}{[1 + (\lambda\dot{\gamma})^a]^{1-\frac{1}{a}}}$	shear thinning
Casson	$\tau^{1/2} = (k\dot{\gamma})^{1/2} + \tau_o^{1/2}$	yield stress
Power law	$\tau = k\dot{\gamma}^n$	shear thinning
Cross	$\mu = \mu_{\infty} + \frac{\mu_0 - \mu_{\infty}}{1 + \lambda\dot{\gamma}^m}$	shear thinning
Herschel-Bulkley	$\tau = k\dot{\gamma}^n + \tau_o$	shear thinning, yield stress
Oldroyd-B	$\boldsymbol{\tau} + \lambda_1 \overset{\nabla}{\boldsymbol{\tau}} = \mu_0 \left(\dot{\boldsymbol{\gamma}} + \lambda_2 \overset{\nabla}{\dot{\boldsymbol{\gamma}}} \right)$	viscoelasticity
Quemada	$\mu = \mu_p \left(1 - \frac{k_0 + k_{\infty} \sqrt{\dot{\gamma}/\dot{\gamma}_c}}{2(1 + \sqrt{\dot{\gamma}/\dot{\gamma}_c})} \phi \right)^{-2}$	shear thinning
Yeleswarapu	$\mu = \mu_{\infty} + (\mu_0 - \mu_{\infty}) \frac{1 + \ln(1 + \lambda\dot{\gamma})}{1 + \lambda\dot{\gamma}}$	shear thinning
Bingham	$\tau = k\dot{\gamma} + \tau_o$	yield stress
Eyring-Powell	$\mu = \mu_{\infty} + \frac{(\mu_0 - \mu_{\infty}) \sinh^{-1}(\lambda\dot{\gamma})}{\lambda\dot{\gamma}}$	shear thinning
Ree-Eyring	$\tau = \tau_c \sinh^{-1} \left(\frac{\mu_0 \dot{\gamma}}{\tau_c} \right)$	shear thinning

Figure 2.2 - The non-Newtonian fluid models that are commonly used to describe blood rheology [19]

The symbols present in Figure 2.2 - are the following:

- $\dot{\gamma}$ shear rate
- $\dot{\gamma}_c$ characteristic shear rate
- $\dot{\boldsymbol{\gamma}}$ rate of strain tensor
- λ characteristic time constant
- λ_1 relaxation time
- λ_2 retardation time
- μ fluid viscosity
- μ_p plasma viscosity
- μ_0 zero-shear-rate viscosity
- μ_{∞} infinite-shear-rate viscosity
- τ shear stress
- $\boldsymbol{\tau}$ stress tensor
- τ_c characteristic shear stress
- τ_o yield-stress
- Φ volume concentration
- a Carreau-Yasuda index
- k consistency coefficient
- k_0 maximum volume fraction for zero shear rate
- k_{∞} maximum volume fraction for infinite shear rate
- m Cross model index
- n power law index
- $\overset{\nabla}{\boldsymbol{\tau}}$ upper convected time derivative

In this work, the focus were large vessels so, the Newtonian formulation of blood flow was used. Other limitations were found while trying to explore the models mentioned earlier, such as the kind of formulation allowed in the software used and lack of information on the values of the variables to fit the models.

$$\tau = \mu\dot{\gamma} \quad (2.1)$$

where μ is the viscosity coefficient.

Chapter 3

Numerical methods

3.1 - Finite element method

Today, the finite-element method is very used in industry and biomechanics [27], in simulating deformable models and flow [28]. In fluid analysis is particularly useful in surgical simulation.

The technique consists in dividing the flow domain into smaller regions (elements), in which governing equations are applied. These equations are rewritten in algebraic form to represent the changes that occur in variables due to incremental changes in position and time. These solutions are adapted each cycle over the entire mesh until a converged value for the viscosity is achieved. The time of the analysis depends on the geometry, mesh configuration and boundary conditions imposed. The major advantage of the FEM is the discretization procedure for simple geometric shapes.[17]

However, mesh-based algorithms, when faced with complex models, irregular geometries, or analyses dealing with large deformations (such as fluid flow), require significant amounts of computation in remeshing tasks.

Applied to fluid mechanics, in the 70's there were published the first FEM articles for the Navier-Stokes equations (Chung[29], Temam[30], Thomasset[31]).[28]

To try to overcome the problem of high computation time, in recent years, several algorithms were developed for 3D flows (multigrid, (Brandt[32], Hackbush[33]), domain decomposition (Glowinski[33]), vectorization (Woodward et al[34]), the development of specialized methods to reach certain objectives (spectral methods, (Orszag[35]), particle methods (Chorin [36]). [28]

3.2 - Meshless method

The problems associated with FEM have created the need to develop a numerical technique capable of reducing the computational time. Meshless methods are used to analyse more complex physics on a set of non-ordered points. These methods were proved to be valid in solid mechanics, fluid dynamics and heat transfer.[37], [38]

There are several types of meshless methods used in fluid dynamics, including Smooth Particle Hydrodynamics (SPH), the Meshless Local Petrov-Galerkin (MLPG) method, methods based on Radial Basis Functions (RBF), and Finite Point Methods (FPM).[39]

This work will be developed using two of the most recently developed meshless methods: the Radial Point Interpolation Method (RPIM) and the Natural Neighbour Radial Interpolation Method (NNRPIM). In this chapter, after a brief description of the general meshless method procedure, both methods are presented and thoroughly explained. The chapter ends with the presentation of the radial point interpolation (RPI) shape functions, which construction procedure is used by both methods.

3.2.1. General meshless method procedure

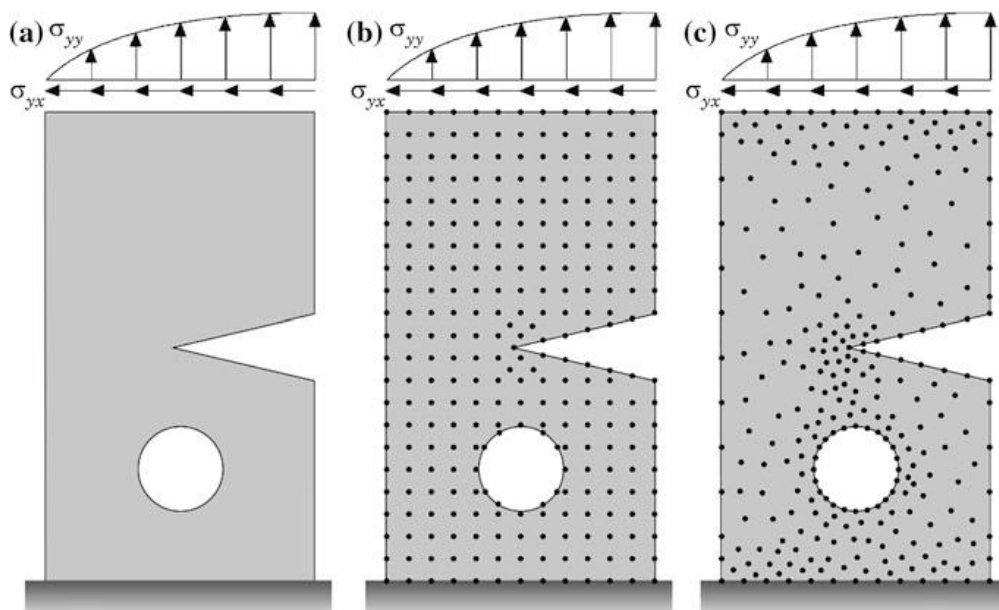


Figure 3.1 - a. Problem domain with the essential and natural boundaries applied. b. Regular nodal discretization. c. Irregular nodal discretization.[40]

First, it is necessary to identify the outline of the solid problem, then is possible to define the natural and essential boundaries (Figure 3.1). After these two requirements are met, it is possible to discretize the domain problem using a nodal set (regular or irregular). An irregular mesh has low accuracy in the regions with low nodal concentration, but is possible to overcome this problem adding more nodes. The addition of new points does not increase the computational cost of the meshing task, since there is no pre-established relation between nodes (as the one existing in FEM).

After this step, the next one is to obtain the nodal connectivity. In FEM, there is a finite element mesh and the nodes that belong to the same element interact directly between themselves and the boundary nodes interact with boundary nodes of nearby elements. In meshless methods, the connectivity between nodes is given by the overlapping of influence-domains, when it comes to RPIM, and influence-cells, when it comes to NNRPIM.

The next step is to set the numerical integration scheme. So, it is required to construct a background integration mesh which can be nodal dependent or independent, the later having a higher accuracy. To have more accurate results with nodal dependent meshes, a stabilization

method is required but this increases the computational time. Next, it is possible to obtain the field variables under study by using approximation or interpolation shape functions. Both methods studied in this work use interpolation shape functions, with radial basis functions (RBF) with polynomial basis functions combined.

3.2.2. RPIM Formulation

3.2.2.1- Influence-domains and nodal connectivity

The first step is to perform an initial nodal discretization of the problem domain, and then ensure the nodal connectivity between each node. First, areas or volumes are defined, depending if the problem is 2D or 3D, with a certain number of nodes.

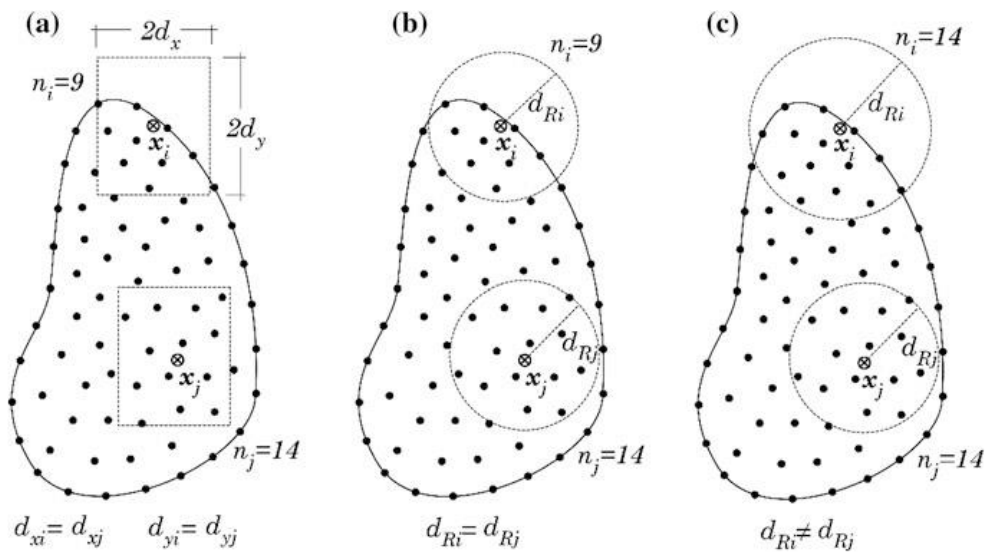


Figure 3.2 - a. Fixed rectangular shaped influence-domain. b. Fixed circular shaped influence-domain. c. Flexible circular shaped influence-domain [40]

As shown in Figure 3.2, influence-domains can have a fixed or variable size, however the latter is recommended since, fixed sized influence domains can lead to an uneven number of nodes inside the influence-domain of different nodes, which reduces the accuracy of the results. The second assures that every node's influence-domain contains the same number of nodes, allowing to have shape functions with the same degree of complexity.

3.2.2.2- Numerical integration

The RPIM uses the Gauss-Legendre integration scheme. So, first a background mesh must be created. This mesh can be created by the connection of the nodes discretizing the problem domain or a mesh larger than the problem domain. If the background integration mesh is larger than the problem domain, the points that are outside of the problem domain must be removed from the computation. The meshes can be quadrilateral or triangular.

Inside of each one is possible to distribute the integration points, as shown in Figure 3.3.

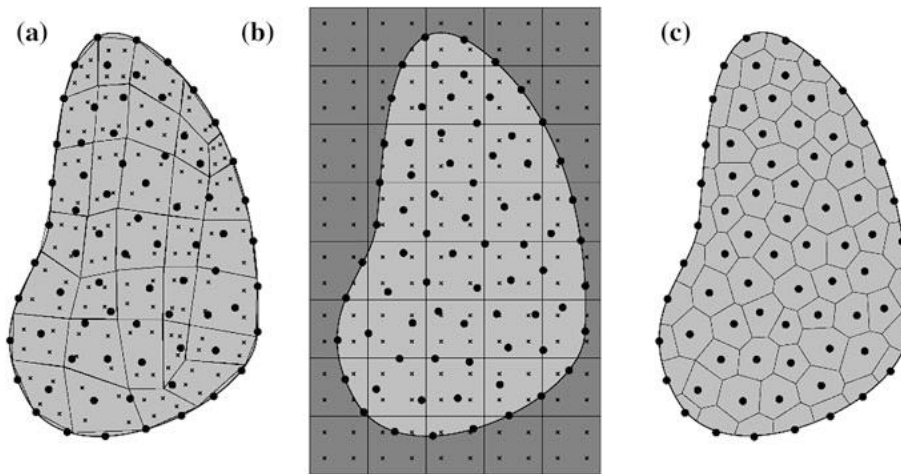


Figure 3.3 - a. Fitted Gaussian integration mesh. b. General Gaussian integration mesh. c. Voronoi diagram for nodal integration [40]

Afterwards, it is used the Gauss-Legendre quadrature technique to obtain the background integration mesh (see Figure 3.4).

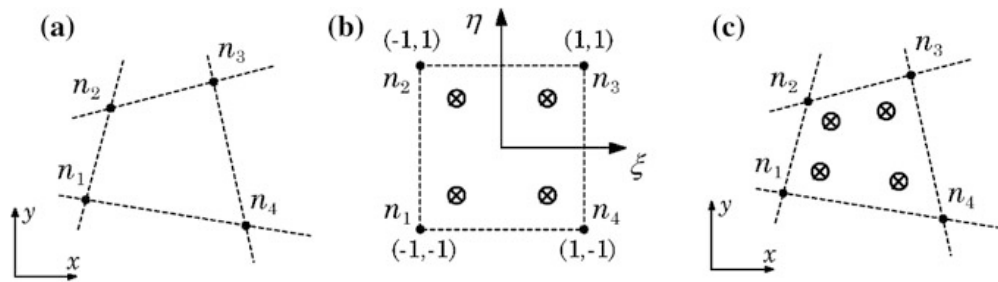


Figure 3.4 - a. Initial quadrilateral from the grid-cell. b. Transformation of the initial quadrilateral into an isoparametric square shape and application of the 2 x 2 quadrature point rule. c Return to the initial quadrilateral shape [40]

First, the isoparametric weights and coordinates of each integration point are defined. Afterwards, the Cartesian coordinates of the integrated points are calculated using isometric interpolation functions.

$$\begin{aligned}
 x &= \sum_{i=1}^m N_i(\xi, \eta) \cdot x_i \\
 y &= \sum_{i=1}^m N_i(\xi, \eta) \cdot y_i
 \end{aligned}
 \tag{3.1}$$

where m represents the number of nodes in the element, and x_i and y_i represent the Cartesian coordinates of the cell nodes.

For the quadrilateral integration cells:

$$\begin{aligned}
 N_1 &= \frac{1}{4}(1 - \xi)(1 - \eta); \\
 N_2 &= \frac{1}{4}(1 + \xi)(1 - \eta); \\
 N_3 &= \frac{1}{4}(1 + \xi)(1 + \eta); \\
 N_4 &= \frac{1}{4}(1 - \xi)(1 + \eta)
 \end{aligned} \tag{3.2}$$

For triangular integration cells:

$$\begin{aligned}
 N_1(\xi, \eta) &= 1 - \xi - \eta; \\
 N_2(\xi, \eta) &= \eta; \\
 N_3(\xi, \eta) &= \xi;
 \end{aligned} \tag{3.3}$$

The integration weight of the integration point is obtained by multiplying the isoparametric weight, of the integration point with the determinant of the Jacobian matrix of the respective cell.

$$J = \begin{bmatrix} \frac{\partial x}{\partial \xi} & \frac{\partial y}{\partial \xi} \\ \frac{\partial x}{\partial \eta} & \frac{\partial y}{\partial \eta} \end{bmatrix} \tag{3.4}$$

Afterwards, the numerical integration is performed using,

$$\int_{-1}^1 \int_{-1}^1 f(\xi, \eta) d\xi d\eta = \sum_{i=1}^m \sum_{j=1}^n \omega_i \omega_j f(\xi, \eta) \tag{3.5}$$

where ω_i is the weight of the integration point x in natural coordinates.

4.2.3- NNRPIM Formulation

3.2.3.1- Natural neighbours

This method uses the natural neighbour concept to determine the nodal connectivity, to obtain influence-cells. The natural neighbour geometric construction is based on the Voronoï diagram of the nodal distribution, from which it can be obtained the geometric and spatial relations between Voronoï cells.

The Voronoï diagram is a partition of the domain composed of N closed and convex sub-regions (Voronoi cells), being N the number of nodes in the discretization mesh, in which, each partition is associated with the node i in a way that any point in the interior of V_i is closer to n_i than to any other node n_j .

Considering a set of N distinct nodes, discretizing a certain space domain $\Omega \in \mathbb{R}^2$,

$$N = \{n_1, n_2, \dots, n_N\} \in \mathbb{R}^2 \tag{3.6}$$

The Figure 3.5 shows the construction of a Voronoï cell of an interest node n_0 .

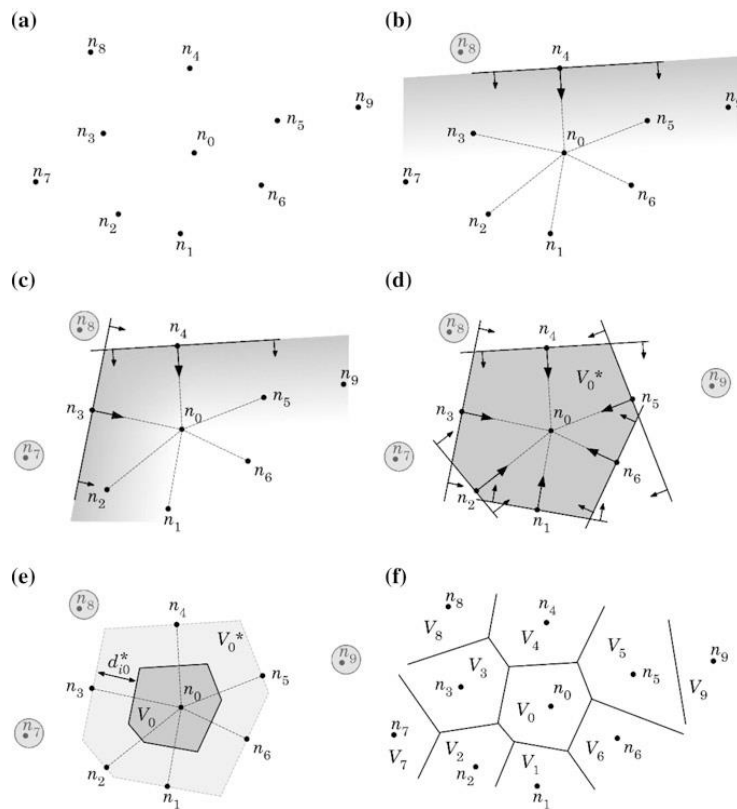


Figure 3.5 - a. Initial nodal set of potential neighbour nodes of node n_0 . b. First trial plane. c. Second trial plane. d. Final trial cell containing just the natural neighbours of node n_0 . e. Node n_0 Voronoï cell V_0 . f. Voronoï diagram [40]

A Voronoï cell is obtained for each node in the mesh and is defined as the geometric place for which all belonging points are closer to that node than to any other. The process to achieve a Voronoï cell is shown in Figure 3.5.

Using figure 3.5 and n_0 as an example, it is possible to obtain a provisional Voronoï cell, which contains all the neighbour's nodes of n_0 . Nodes located outside the ones contained in the provisional Voronoï cell are discarded. First, a potential neighbour must be chosen, for example n_3 and determining vector u_{30} ,

$$u_{30} = \frac{(x_0 - x_3)}{\|x_0 - x_3\|} \quad (3.7)$$

Being $u_{50} = \{u_{30}, v_{30}, w_{30}\}$. All nodes that follow this relationship,

$$u_{30}x + v_{30}y + w_{30}z \geq (u_{30}x_3 + v_{30}y_3 + w_{30}z_3) \quad (3.8)$$

are discarded.

Now, obtained the provisional Voronoï cell for node n_0 , it is possible to obtain the Voronoï cell, V_0 . As shown in Figure 3.5, the distance between node n_0 and the boundary of Voronoï cell, V_0 is half the Euclidian norm of node n_0 and the neighbour node in question.

Using n_3 as example, the distance between n_0 and the boundary referring to node n_3 is given by,

$$d_{n_0n_3} = \frac{E(x_0, x_3)}{2} \quad (3.9)$$

Then, following the same reasoning for each node, it is possible to obtain the Voronoï diagram.

3.2.3.2- Influence cells and nodal connectivity determination

In NNRPIM the nodal connectivity is imposed using the information coming from the Voronoï diagram. There are two types of influence-cells, accordingly to their level of nodal connectivity, as shown in Figure 3.6. The first-degree influence-cell of a point of interest consists of its natural neighbours (directly obtained by the Voronoï diagram). Concerning the second-degree influence-cell of a point of interest, it consists of the first natural neighbours considered in the first-degree influence-cell added to their own natural neighbours.

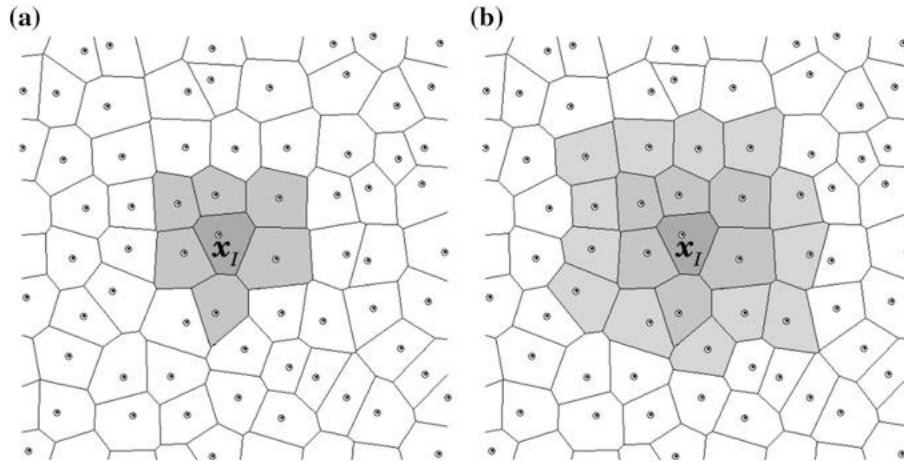


Figure 3.6 - a. First degree influence-cell b. Second degree influence-cell [40]

3.2.3.3- Numerical integration

After constructing the Voronoï diagram, it is possible to obtain a nodal dependent integration mesh based on the nodal distribution special information. Primarily, the Voronoï cells are divided in sub-cells by the lines intersecting the central node and each neighbourhood node. For a regular mesh, the partition results are triangles and for irregular meshes the result are quadrilaterals.

Using the Delaunay tessellation (see Figure 3.7), the nodes of Voronoï cells sharing common boundaries are connected, and the overlap of both the Delaunay tessellation and the influence-cell boundaries leads to a smaller sub-cell.

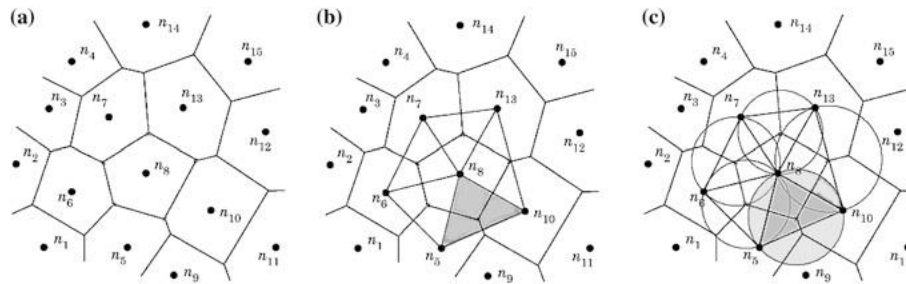


Figure 3.7 - a. Voronoï diagram, b. Delaunay triangulation and c. Natural neighbour circumcircles [40]

Thus, the cell is divided in several sub-cells (in equal to number of neighbour nodes of its central node), being that its area, A_v , is equivalent to the sum of the areas of the sub-cells, $A_{S_{li}}$, given by

$$A_{V_I} = \sum_{i=1}^n A_{S_{li}}, \quad \forall A_{S_{li}} \geq 0 \quad (3.10)$$

Based on the Gauss-Legendre numerical integration numerical integration, integration points are inserted in the barycentre of each sub-cell (Figure 3.8).

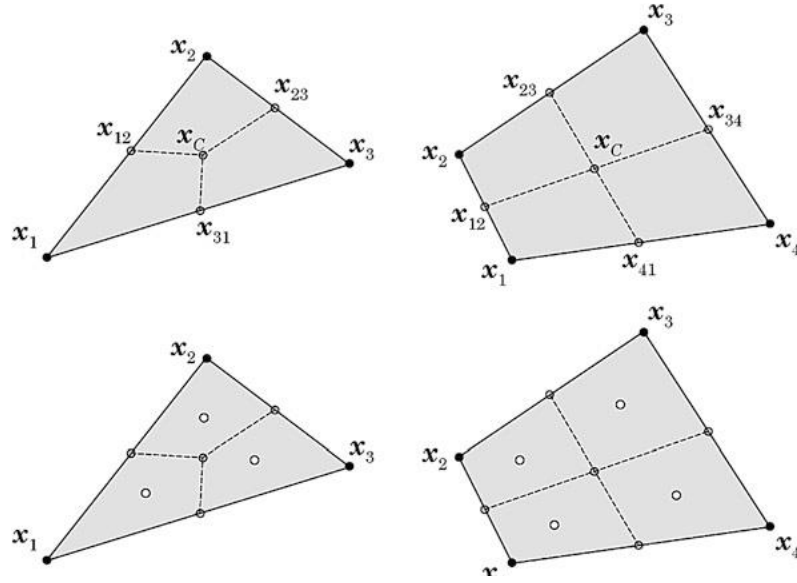


Figure 3.8 - Triangular shape and quadrilateral shape and the respective integration points x_I using the Gauss-Legendre integration scheme [40]

This is an example for 1 integration point for each sub-cell. To use more integration points, each sub-cell is divided again into small quadrilateral sub-cells and the process is equal to the RPIM using quadrilateral cells. This process is repeated to all the other Voronoi cells, to obtain the domain integration.

3.2.3.4- Shape functions

Both numerical methods presented in this work use the same methodology to construct the shape functions, using a combination of radial basis functions with polynomial functions.

Consider a function $u(x)$, defined in a certain influence-domain, discretizing by a set of N distinct nodes,

$$u(x_I) = \sum_{i=1}^n R_i(x_I) a_i(x_I) + \sum_{j=1}^m p_j(x_I) b_j(x_I) = \mathbf{R}^T(x_I) \mathbf{a} + \mathbf{p}^T(x_I) \mathbf{b} \quad (3.11)$$

which can be rewritten as,

$$u(x_I) = \sum_{i=1}^n R_i(x_I) a_i(x_I) + \sum_{j=1}^m p_j(x_I) b_j(x_I) = \{\mathbf{R}^T(x_I), \mathbf{p}^T(x_I)\} \begin{Bmatrix} \mathbf{a} \\ \mathbf{b} \end{Bmatrix} \quad (3.12)$$

where $R_i(x_I)$ is the RBF, $p_j(x_I)$ is the polynomial basis function, n is the number of nodes inside the influence-domain of the interest point x_I and $a_i(x_I)$ and $b_j(x_I)$ are non-constant coefficients of $R_i(x_I)$ and $p_j(x_I)$ respectively.

$$\mathbf{a}^T(x_I) = [a_1(x_I), a_2(x_I), \dots, a_n(x_I)] \quad (3.13)$$

$$b^T(\mathbf{x}_I) = [b_1(x_I), b_2(x_I), \dots, b_n(x_I)] \quad (3.14)$$

$$R^T(\mathbf{x}_I) = [R_1(x_I), R_2(x_I), \dots, R_n(x_I)] \quad (3.15)$$

$$p^T(\mathbf{x}_I) = [p_1(x_I), p_2(x_I), \dots, p_n(x_I)] \quad (3.16)$$

This method uses the Multiquadric (MQ) function presented obtaining a MQ-RBF:

$$R_{ij} = (r_{ij}^2 + c^2)^p \quad (3.17)$$

where c and p are two parameters whose optimal values were found as 0,0001 and 1,0001 [41], respectively, and r_{ij} the Euclidian norm between the integration point x_I and a certain node \mathbf{x}_i ,

$$r_{ij} = \sqrt{(x_i - x_I)^2 + (y_i - y_I)^2} \quad (3.18)$$

The polynomial basis are for 2D problems are:

$$\text{Null basis} - \mathbf{x}^T = \{x, y\}; p^T(\mathbf{x}) = \{0\}; m = 0 \quad (3.19)$$

$$\text{Constant basis} - \mathbf{x}^T = \{x, y\}; p^T(\mathbf{x}) = \{1\}; m = 1 \quad (3.20)$$

$$\text{Linear basis} - \mathbf{x}^T = \{x, y\}; p^T(\mathbf{x}) = \{1, x, y\}; m = 3 \quad (3.21)$$

$$\text{Quadratic basis} - \mathbf{x}^T = \{x, y\}; p^T(\mathbf{x}) = \{1, x, y, x^2, xy, y^2\}; m = 6 \quad (3.22)$$

To assure a unique approximation, the polynomial term must follow the rule:

$$\sum_{i=1}^n p_j(x_i) a_i = 0, \quad j = 1, 2, \dots, m \quad (3.23)$$

The function can be reformulated to

$$\begin{bmatrix} \mathbf{R} & \mathbf{p} \\ \mathbf{p}^T & \mathbf{0} \end{bmatrix} \begin{Bmatrix} \mathbf{a} \\ \mathbf{b} \end{Bmatrix} = \begin{Bmatrix} \mathbf{u}_s \\ \mathbf{0} \end{Bmatrix} = \mathbf{G} \begin{Bmatrix} \mathbf{a} \\ \mathbf{b} \end{Bmatrix} \quad (3.24)$$

Solving equation 2.24,

$$\begin{Bmatrix} \mathbf{a} \\ \mathbf{b} \end{Bmatrix} = \mathbf{G}^{-1} \begin{Bmatrix} \mathbf{u}_s \\ \mathbf{0} \end{Bmatrix} \quad (3.25)$$

Substituting equation 3.25 in eq. 3.11, the shape function is obtained:

$$u(x_I) = \{\mathbf{R}^T(x_I), \mathbf{p}^T(x_I)\} \mathbf{G}^{-1} \begin{Bmatrix} \mathbf{u}_s \\ \mathbf{0} \end{Bmatrix} = \varphi(x_I) \mathbf{u}_s \quad (3.26)$$

which $\varphi(x_I)$ is the shape function defined by

$$\varphi(x_I) = \{\mathbf{R}^T(x_I), \mathbf{p}^T(x_I)\} \mathbf{G}^{-1} = [\varphi_1(x_I), \varphi_2(x_I), \dots, \varphi_n(x_I)] \quad (3.27)$$

Since they respect the Kronecker delta property,

$$\varphi(x_j) = \begin{cases} 1, & i = j, j = 1, 2, \dots, n \\ 0, & i \neq j, j = 1, 2, \dots, n \end{cases} \quad (3.28)$$

which means they pass through every single node within the influence-domain (or influence-cell), in opposition to approximation shape functions which do not.

3.3 - Discretized formulation flow

In this section, it will be explained the flow formulation for viscoplastic materials. This deduction was extracted from Zienkiewicz et al. [42]. The problem variables are \mathbf{u} , the velocity, $\dot{\boldsymbol{\varepsilon}}$, the rate of strain defined by the operator \mathbf{S} as

$$\dot{\boldsymbol{\varepsilon}} = \mathbf{S} \mathbf{u} \text{ (or } \dot{\varepsilon}_{ij} = \frac{u_{i,j} + u_{j,i}}{2}) \quad (3.29)$$

Being \mathbf{S} matrix is defined by

$$[\mathbf{S}]_I = \begin{bmatrix} \left. \begin{array}{cc} \frac{d\varphi_1}{dx} & 0 \\ 0 & \frac{d\varphi_1}{dy} \end{array} \right| & \dots & \left. \begin{array}{cc} \frac{d\varphi_n}{dx} & 0 \\ 0 & \frac{d\varphi_n}{dy} \end{array} \right| \\ \left. \begin{array}{cc} \frac{d\varphi_1}{dy} & \frac{d\varphi_1}{dx} \end{array} \right| & & \left. \begin{array}{cc} \frac{d\varphi_n}{dy} & \frac{d\varphi_n}{dx} \end{array} \right| \end{bmatrix} \quad (3.30)$$

Where φ is the shape function and n is the number of nodes of the element in study that have the integration point x_I or the number of nodes inside the influence domain of the integration point x_I . The \mathbf{u} vector is defined by $\mathbf{u} = \{u_x \ u_y\}^T$. As the “pressure” p is equal to the mean stress, the constitutive law defines stress as

$$\boldsymbol{\sigma} = \mu \mathbf{D}_0 \dot{\boldsymbol{\varepsilon}} + \mathbf{m} p \text{ (or } \sigma_{ij} = 2\mu \left(\dot{\varepsilon}_{ij} - \frac{\delta_{ij} \varepsilon_{kk}}{3} \right) + \delta_{ij} p) \quad (3.31)$$

where μ is the viscosity, $\boldsymbol{\sigma}$ is the stress, δ_{ij} is the delta Kronecker and \mathbf{D}_0 and \mathbf{m} are matrices avoiding the need for tensorial notation. Notice that it can be verified that the matrix \mathbf{D}_0 has the following form:

$$\mathbf{D}_0 = \begin{bmatrix} \frac{4}{3} & -\frac{2}{3} & -\frac{2}{3} & 0 & 0 & 0 \\ -\frac{2}{3} & \frac{4}{3} & -\frac{2}{3} & 0 & 0 & 0 \\ -\frac{2}{3} & -\frac{2}{3} & \frac{4}{3} & 0 & 0 & 0 \\ 0 & 0 & 0 & 1 & 0 & 0 \\ 0 & 0 & 0 & 0 & 1 & 0 \\ 0 & 0 & 0 & 0 & 0 & 1 \end{bmatrix} \quad (3.32)$$

Although the inverse of \mathbf{D}_0 does not exist, the inverse relation can be written as,

$$\dot{\boldsymbol{\varepsilon}} = \frac{1}{\mu} \mathbf{D}^{-1}(\boldsymbol{\sigma} - \mathbf{m}p) \quad (3.33)$$

With

$$\mathbf{D}^{-1} = \begin{bmatrix} 2 & 0 & 0 & 0 & 0 & 0 \\ 0 & 2 & 0 & 0 & 0 & 0 \\ 0 & 0 & 2 & 0 & 0 & 0 \\ 0 & 0 & 0 & 1 & 0 & 0 \\ 0 & 0 & 0 & 0 & 1 & 0 \\ 0 & 0 & 0 & 0 & 0 & 1 \end{bmatrix} \quad (3.34)$$

And $\mathbf{m} = \{1 \ 1 \ 0\}$ for a 2D problem. In general μ is dependent from the strain rate and the total accumulated strain, so the system is non-linear. For many viscoplastic materials the viscosity follows this relation:

$$\mu = (\sigma_y + \gamma \dot{\boldsymbol{\varepsilon}}^m) / 3 \dot{\boldsymbol{\varepsilon}} \quad (3.35)$$

Where σ_y is the uniaxial yields stress which, for strain hardening, is a function of the accumulated second strain invariant $\tilde{\boldsymbol{\varepsilon}}$ and temperature T . γ is the fluidity parameter

$$\sigma_y = \sigma_y(\tilde{\boldsymbol{\varepsilon}}, T) \quad (3.36)$$

and $\tilde{\boldsymbol{\varepsilon}}$ is the second invariant of the strain rate

$$\dot{\boldsymbol{\varepsilon}} = \left(\frac{2}{3} \dot{\boldsymbol{\varepsilon}}_{ij} \cdot \dot{\boldsymbol{\varepsilon}}_{ij} \right)^{1/2} \quad (3.37)$$

Assuming pure elasticity, γ is considered null: $\gamma = 0$.

The governing equations of the problem are now momentum conservation (with $\boldsymbol{\sigma}$ defined by equations 3.8 and 3.9 and \mathbf{b} the body force).

$$\mathbf{S}^T \boldsymbol{\sigma} + \mathbf{b} = 0 \quad (\text{or } \sigma_{ij,i} + b_i = 0) \quad (3.38)$$

where \mathbf{S} is the strain operator, pointed in equation 3.7, and incompressibility

$$\mathbf{m}^T \mathbf{S} \mathbf{u} = 0 \quad (\text{or } \frac{du}{dx} + \frac{dv}{dy} = 0) \quad (3.39)$$

In the problem domain Ω with the right boundary conditions on tractions (on Γ_t) or velocities (on Γ_u). The standard Galerkin discretization process with

$$\mathbf{u} \approx \hat{\mathbf{u}} = N_u \bar{\mathbf{u}} \text{ and } p = N_p \bar{p} \quad (3.40)$$

where N_u is the shape functions of velocity and N_p are the shape functions of pressure:

$$N_* = \left[\begin{array}{c|c} \varphi_1^* & 0 \\ \hline 0 & \varphi_1^* \end{array} \right] \cdots \left[\begin{array}{c|c} \varphi_n^* & 0 \\ \hline 0 & \varphi_n^* \end{array} \right] \quad (3.41)$$

Notice that the shape functions for the velocities are obtained in the integration points, considering the full integration mesh, and the shape functions for pressures are obtained in the reduced integration mesh (considering the integration point coincident with the nodes). This leads to

$$\begin{bmatrix} \mathbf{K} & \mathbf{Q} \\ \mathbf{Q}^T & \mathbf{0} \end{bmatrix} \begin{bmatrix} \bar{\mathbf{u}} \\ \bar{p} \end{bmatrix} = \begin{bmatrix} \mathbf{f} \\ \mathbf{0} \end{bmatrix} \quad (3.42)$$

in which

$$\mathbf{K} = \int_{\Omega} (\mathbf{S}N_u)^T \mu \mathbf{D}_0 (\mathbf{S}N_u) d\Omega \quad (3.43)$$

$$\mathbf{Q} = \int_{\Omega} (\mathbf{S}N_u)^T \mathbf{m} N_p d\Omega \quad (3.44)$$

$$\mathbf{f} = \int_{\Omega} N_u^T \mathbf{b} d\Omega + \int_{\Gamma_t} N_u^T \mathbf{t} d\Gamma \quad (3.45)$$

where \mathbf{K} is the stiffness matrix, \mathbf{Q} is matrix imposing the incompressible condition and \mathbf{f} is the force. In the preceding discretization it is necessary to assure that the resulting equations are never singular so that convergence is assured by the Babuska-Brezzi condition.

$$\begin{bmatrix} \mathbf{K}_e & \mathbf{Q}_e \\ \mathbf{Q}_e^T & \mathbf{I}/\alpha \end{bmatrix} \begin{bmatrix} \bar{\mathbf{u}}_e \\ \bar{p}_e \end{bmatrix} = \begin{bmatrix} \mathbf{f}_e \\ \mathbf{0} \end{bmatrix} \quad (3.46)$$

where \mathbf{I} is the identity matrix and α the penalty number taken as $\alpha = 10^7 \mu$. This results in a single matrix element stiffness matrix

$$\bar{\mathbf{K}}_e \bar{\mathbf{u}}_e = (\mathbf{K}_e - \mathbf{Q}_e \mathbf{Q}_e^T) \bar{\mathbf{u}}_e = \mathbf{f}_e \quad (3.47)$$

and the final assembled non-linear system of equations

$$\bar{\mathbf{K}} \bar{\mathbf{u}} = \mathbf{f} \quad (3.48)$$

$$\bar{\mathbf{K}} = \bar{\mathbf{K}}(\mathbf{u}), \quad \mu(\dot{\boldsymbol{\varepsilon}}) = \mu(\mathbf{u}) \quad (3.49)$$

Which is solved iteratively

3.4 - Numerical analysis applied to blood flow

The blood flow studies are in arteries, such as hemodynamics of bypass graft for stenosed arteries, hemodynamics of stented aneurysm at the aortic arch and hemodynamics of bypass treatment for DeBakey III aortic dissection. [1]

The main methods to simulate blood flow in this vessel are one-dimensional Navier-Stokes finite element model for elastic networks and the Hagen-Poiseuille model for rigid networks. These models are Newtonian, but the second can be used like a Poiseuille-like non-Newtonian flow through the inclusion of time-independent non-Newtonian effects using a vessel-dependent non-Newtonian effective, which is computed and updated iteratively to reach a consistent flow solution over the whole network. [19]

Using meshless methods in blood flow analysis is still unusual; The most used methods are Smooth Particle Hydrodynamics (SPH) and localized meshless method (LCMM). [38], [43]

In order to simulate the blood flow with the three methods described before (FEM, RPIM and NNRPIM), it was necessary to use a software that could run those formulations.

FEMAS is a Finite Element and Meshless Analysis Software fully developed by Prof. Dr. Jorge Belinha. FEMAS possesses a graphical user interface (GUI) running in Matlab environment (see Figure 3.9). This software allows to analyse a model with FEM, RPIM and NNRPIM.

Other functionality of this software is to design 2D and 3D models. It is possible to select the material properties and perform geometrical transformations on the models.

It permits to study structural problems considering 3D approaches, assuming one of the following analysis:

- Linear Elasto-static analysis
- Free Vibration linear elastic analysis
- Buckling linear elastic analysis
- Elasto-plastic non-linear analysis
- Bone tissue remodelling analysis
- Fluid flow analysis (low velocities)

It allows to use Finite element method (2D triangular elements with 3, 4 and 6 nodes and 2D quadrangular elements with 4, 8 and 9 nodes, and 3D tetrahedral elements with 4, 8 and 10 nodes and 3D hexahedral elements with 9, 20 and 27 nodes) and meshless methods (2D and 3D). To design more complex models, it was used a finite element mesh generator commercial code.

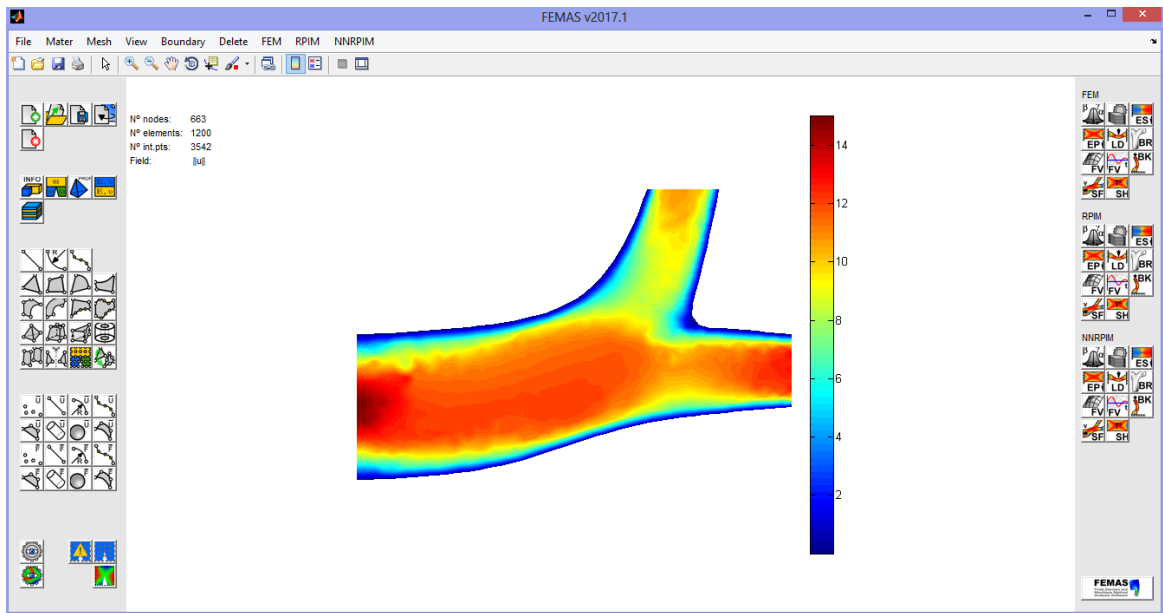


Figure 3.9 - Finite Element and Meshless Analysis Software (FEMAS) - Print-screen of an artery bifurcation and corresponding velocity field.

Chapter 4

Preliminary studies

In every new technique applied to a specific field, it is important to study its limitations and its advantages. Since there is not previous studies with the meshless methods described earlier, it is important to perform a thorough study in several geometries.

This chapter presents studies in 2D and 3D and aims to compare FEM with NNRPIM and RPIM. In this chapter, all the figures have the maximum and minimum velocity explicated, to help reading the colour scale.

4.1- 2D convergence studies

The work in this chapter aims to compare each numerical method and determine which level of discretization is necessary to have the most accurate results in different geometries. In this convergence study, there were build 6 different models with different geometries, each with different 4 meshes. These were successively refined following a rule on 2^n . For each mesh, there were made 4 analysis: FEM with 2D triangular elements with 3 nodes and another with triangular elements with 6 nodes, RPIM and NNRPIM. The models were built using FEMAS.

Another goal of this convergence study is to evaluate the maintenance of the discharge though the model. Assuming that there is mass conservation, the discharge should be constant throughout the model. The last goal is to compare the different velocity profile in sections of the model.

In these simulations, blood was simulated as a Newtonian isotropic fluid. The viscosity is $3,5 \times 10^{-6}$ N.ms/mm² and the density is 1,05 kg/mm³.

Before running an analysis, it is necessary to define the boundary conditions (natural and essential). To assess the best boundary conditions preliminary tests were performed: it was tested a normal boundary condition (for all nodes in the boundary walls it was allowed displacements along the wall line/surface) and a fully clamped boundary condition (all nodes in the boundary walls were constrained both in x and y direction).

It was verified that the first condition was not suited for models with some degree of curvature (the velocity in the walls was different from 0). Therefore, all models used in convergence tests used the second condition. With this technique, the fluid is unable to pass beyond the artery's walls. Moreover, in end of the vessel, no boundary conditions were applied, allowing the fluid to freely exit the domain.

At the entry, it was applied a velocity profile. The velocity profile of a fluid in laminar regime is described by a parabolic equation, as shown in Figure 4.1.

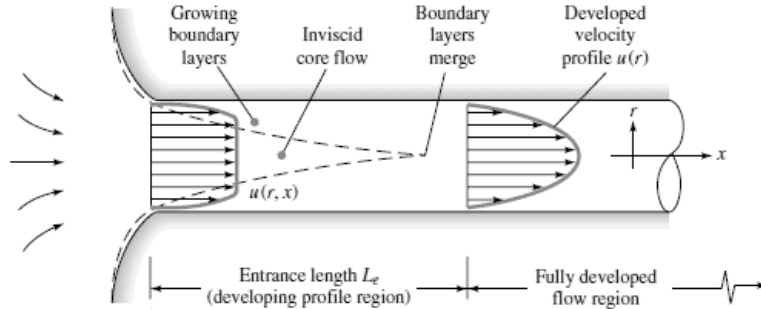


Figure 4.1 - Laminar velocity profile in a tube [45]

The equation of a parabola can be generically written as:

$$u(r) = a(r)^2 + br + c \quad (4.1)$$

Assuming the velocity profile in the walls is 0 and $H/2$ is maximum:

$$\begin{cases} a(H)^2 + bH + c = 0 \\ a(0)^2 + b \times 0 = 0 \\ a(H/2)^2 + b \times H/2 = V_{max} \end{cases} \quad (4.2)$$

It is possible to obtain the non-constant parameters of the parabolic expression:

$$\begin{cases} a = \frac{-4V_{max}}{h^2} \\ b = \frac{4V_{max}}{h} \\ c = 0 \end{cases} \quad (4.3)$$

The values for the maximum velocity in the convergence tests is 0.15 mm/ms.[46] This value was based on the maximum velocity in veins and the height is based on a credible diameter for a deep vein of the pelvis.

The Figure 4.2 shows how the boundary conditions are represented in FEMAS.

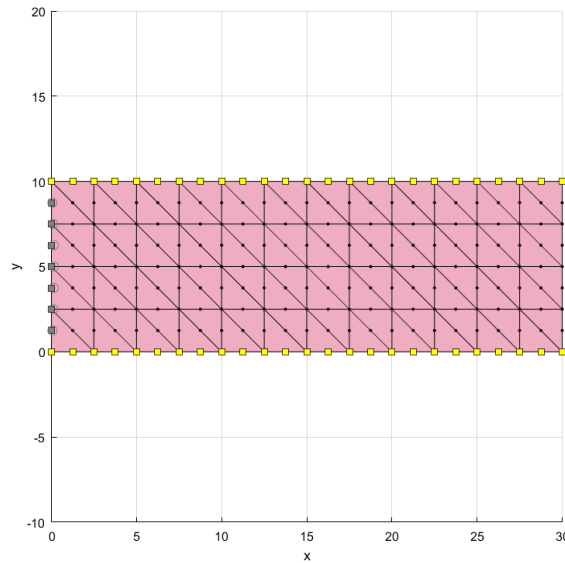


Figure 4.2 - Example of the boundary conditions applied

As presented in previous sections, the performance of the NNRPIM and RPIM formulation depends on some parameters, such as the size of the influence domain, the MQ-RBF shape parameters, the polynomial basis and the integration scheme.

The parameters presented in Table 4.1, are the standard values used in the analysis. In some models and meshes, these parameters had to be adjusted to have more accurate results. These changes will be mentioned in the examples that didn't used the parameters in Table 4.1.

Table 4.1 - Default RPIM and NNRPIM used in the analysis

RPIM			NNRPIM		
Influence domain	Number of nodes inside the influence domain	16	Influence cells	Order	Second
	Parameter c	1.42		Parameter c	0.0001
RPI shape functions	Parameter p	1.03	RPI shape functions	Parameter p	0.9999
	Polynomial	Constant		Polynomial	Constant
Integration scheme	Gauss points	1	Integration scheme	Integration	1 (full integration)

The quantitative comparison between the three techniques is the most suited comparison methodology. Thus, three types of charts were created:

- The discharge in each cross section on a given model with a certain discretization level, for each numerical method;
- The discharge for each discretization level on a given cross section, for each numerical method;

- The velocity profile in a given cross section

As mentioned before, the discharge must be constant. Thus, after obtaining the velocity for each node, this variable was calculated, as follows:

$$Q_e = \sum_i^N v_e^i A_e^i \quad (4.4)$$

Where Q_e is the discharge, v_e^i is the velocity in each node of the cut and A_e^i area occupied by the node.

In order to calculate the area that each node represents, the next methodology was followed. Considering that Figure 4.3 represents the area occupied by each node, it is perceptible that the area is calculated differently for the nodes in the border and nodes in the middle.

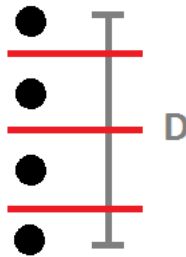


Figure 4.3- Representation of the nodes in a cross section

Assuming the thickness of the model is 1 mm, the area of the lateral nodes and the interior nodes is respectively

$$A_e^i = \frac{D}{2(n-1)} \quad (4.5)$$

$$A_e^i = \frac{D}{n-1}$$

where n is the number of nodes in the cross section. Theoretically, the result should be the integration of the velocity profile. The comparison is always made between models with the same number of nodes, rather than the same number of elements.

4.1.1- Linear model

The Figure 4.4 presents the first model. The meshes (a), (b), (c) and (d) with triangular elements with 3 nodes have, respectively, 21, 65, 255 and 833 elements. The same meshes with triangular elements with 6 nodes have, respectively, 65, 225, 833 and 3201 nodes.

The model has 30 mm of length and 10 mm of height. Following equation 7.3, the initial velocity profile is:

$$u(r) = 0.06(r)^2 - 0.006r \quad (4.6)$$

and therefore, the theoretical discharge should be:

$$\int_0^{10} (0.06x - 0.006x^2) dx = 1 \quad (4.7)$$

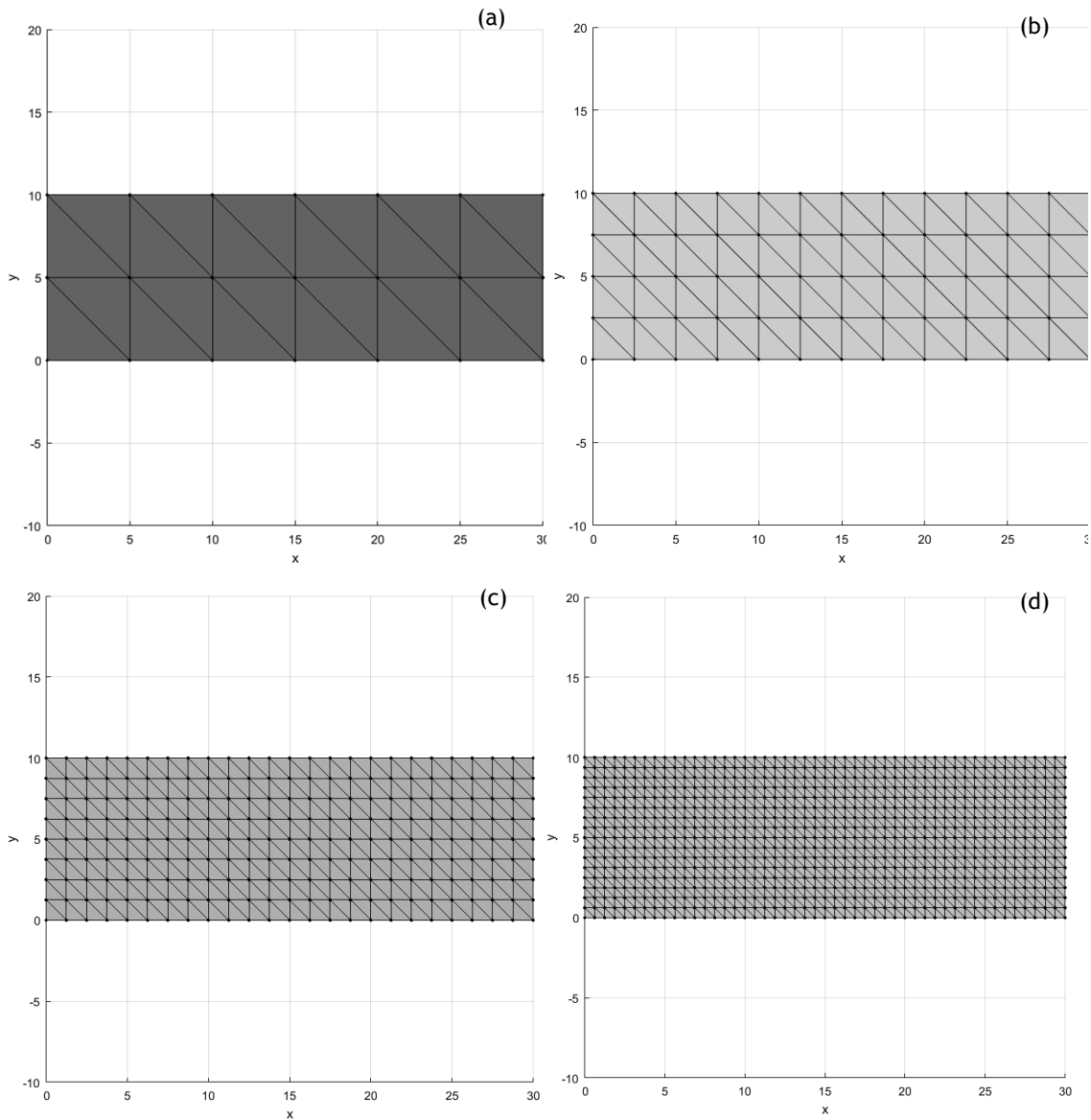


Figure 4.4 - Linear model with different meshes

a. 24 elements b. 96 elements c. 384 elements d. 1536 elements

4.2.3- Results

The velocity maps are presented in the Figure 4.5, Figure 4.6, Figure 4.7, Figure 4.8 and Figure 4.9.

Figure 4.5 represents the analysis of the linear model with 21 nodes.

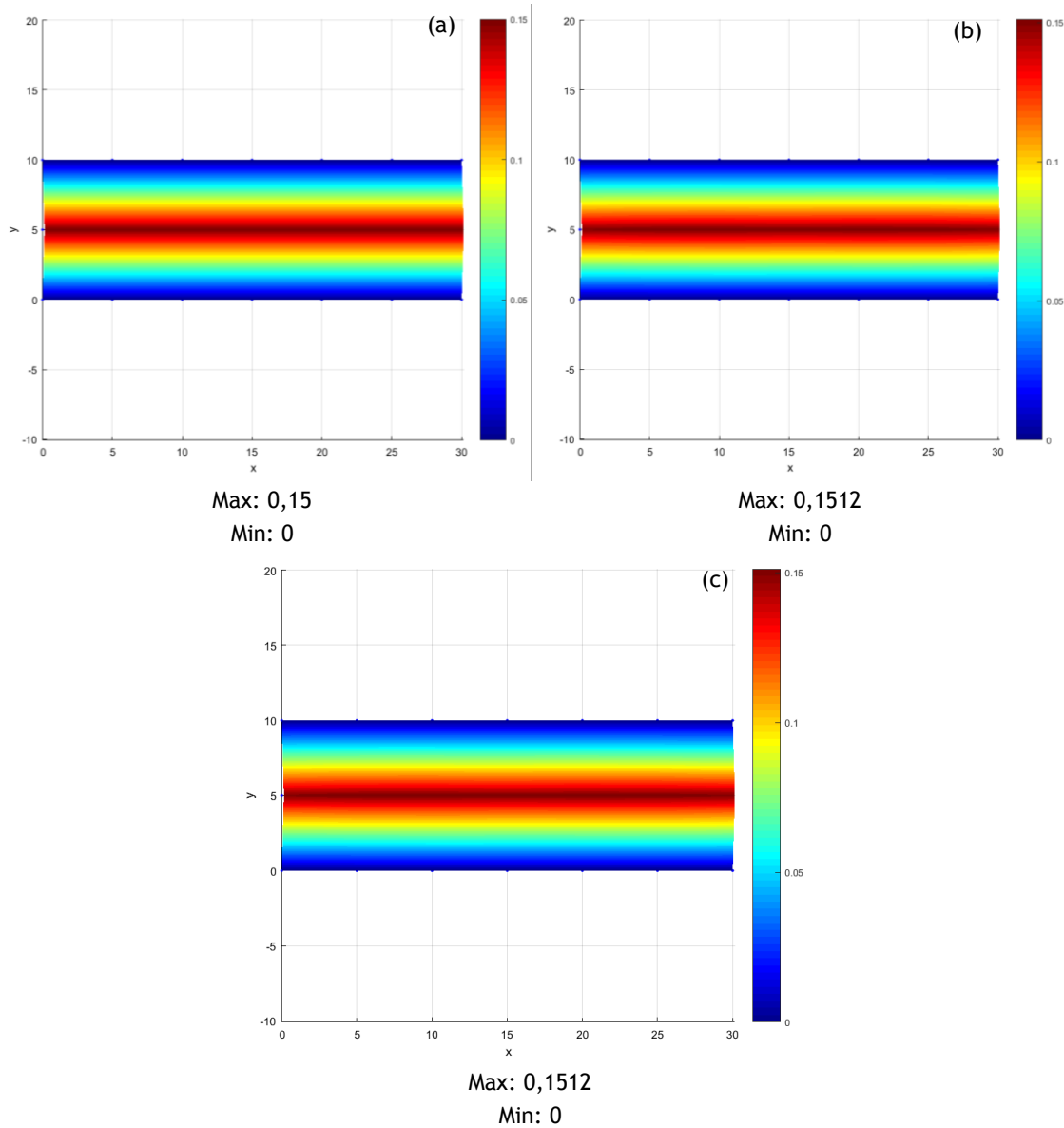


Figure 4.5 - Linear model (21 nodes) analysed with different methods
a. FEM (triangular elements with 3 nodes) b. NNRPIM c. RPIM

In Figure 4.5, the results are similar between FEM with triangular elements with 3 nodes, NNRPIM and RPIM, with the same maximum velocity.

Figure 4.6 represents the analysis of the linear model with 65 nodes.

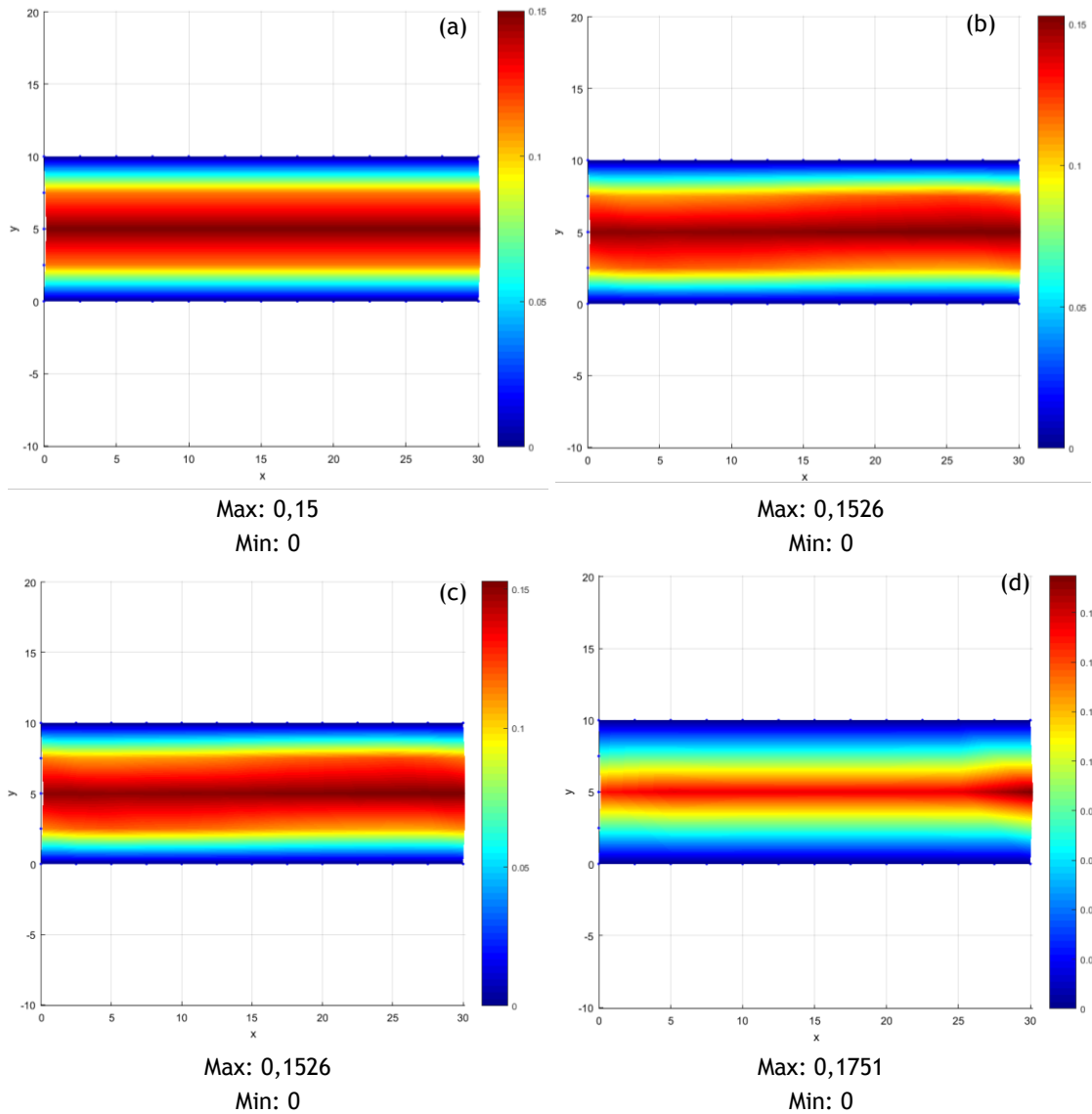


Figure 4.6 - Linear model (65 nodes) analysed with different methods

a. FEM (triangular elements with 3 nodes) b. NNRPIM c. RPIM d. FEM (triangular elements with 6 nodes)

In Figure 4.6, the results are similar, with NNRPIM and RPIM with a slightly higher velocity. The FEM with 6 nodes per element, the maximum velocity is higher (above 0,16 mm/mms) and the velocity increases in the end of the model.

Figure 4.7 represents the analysis of the linear model with 65 nodes.

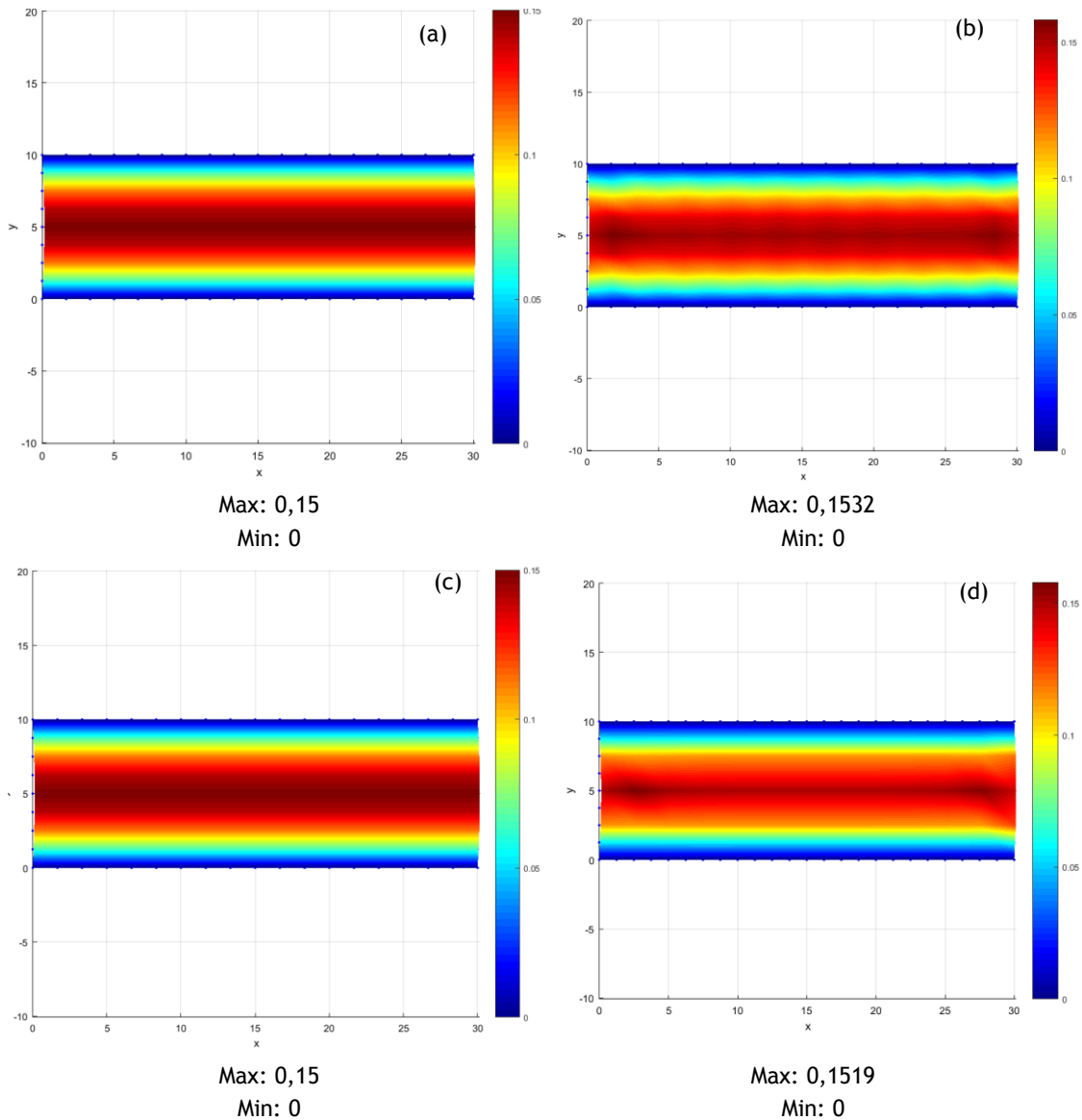


Figure 4.7 - Linear model (255 nodes) analysed with different methods
 a. FEM (triangular elements with 3 nodes) b. NNRPIM c. RPIM d. FEM (triangular elements with 6 nodes)

In Figure 4.7, it is possible to observe that the FEM with elements with 3 nodes and RPIM is similar. NNRPIM has a slightly higher maximum velocity and it is possible to observe that the flow is not as constant as FEM with 3 nodes and RPIM. FEM with a 6 nodes triangular element is much more different.

With the increase of nodes, it is possible to see more differences in the images. To achieve these results, it was necessary to change the standard parameters. For RPIM, the number of nodes inside the influence domain is 27, the parameter c is 0,0001, the parameter p is 0,9999 and the number of Gauss points is 3. For NNRPIM, the parameter c is 1,42 and the parameter c is 1.03. If these parameters were not changed NNRPIM results would be inconsistent and RPIM results would have a significant increase in the velocity in the end of the model.

Figure 4.7 represents the analysis of the linear model with 833 nodes.

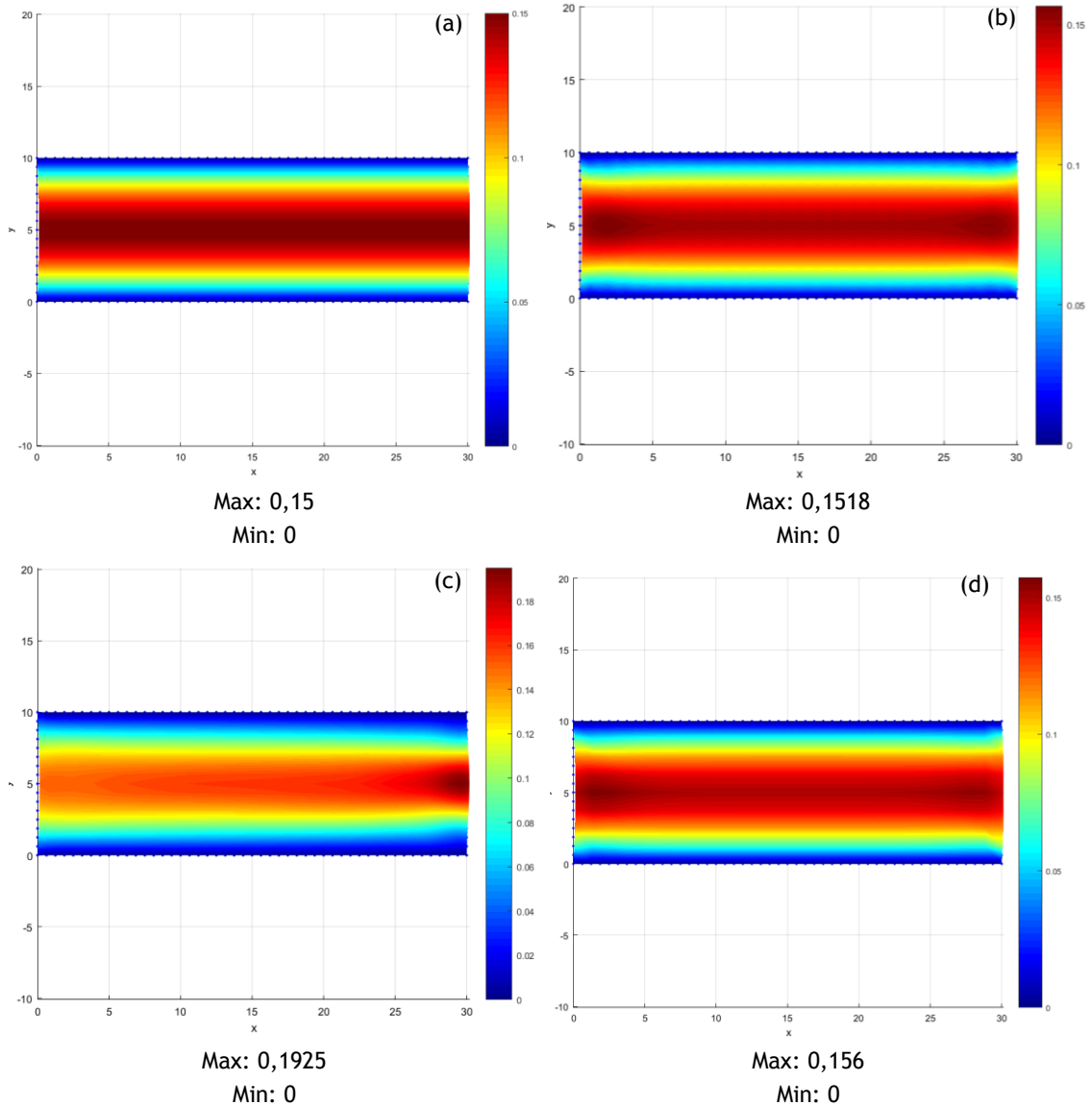
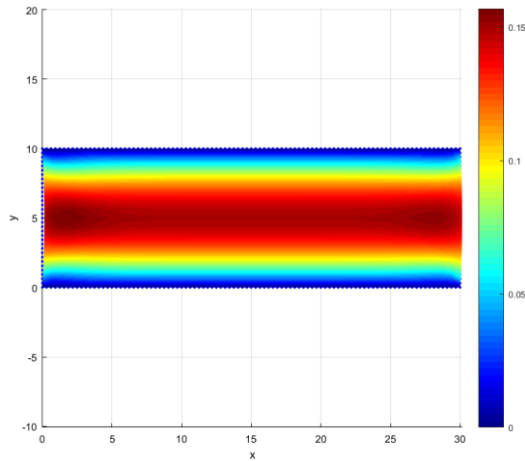


Figure 4.8 - Linear model (833 nodes) analysed with different methods
 a. FEM (triangular elements with 3 nodes) b. NNRPIM c. RPIM d. FEM (triangular elements with 6 nodes)

In Figure 4.8 and comparing to the rest of the figures, the NNRPIM seems to be more stable, and the RPIM seems to have an increase of velocity in the end of the model, despite changing parameters. At this level of discretization, FEM with a 6 nodes element, seems to have more similarities with the rest of the analysis with the same number of nodes. For RPIM, the number of nodes inside the influence domain is 27, the parameter c is 0,0001, the parameter p is 0,9999 and the number of Gauss points is 3. This did not change significantly the results in RPIM.

At last, Figure 4.9, represents the last mesh, but with a 6 nodes element.



Max: 0,156 / Min: 0

Figure 4.9 - Linear model (3201 nodes) analysed with FEM (triangular elements with 6 nodes)

Having numerical comparison is essential to withdraw conclusions. Figure 4.10 evaluates the variations in discharge in the several meshes and numerical methods.

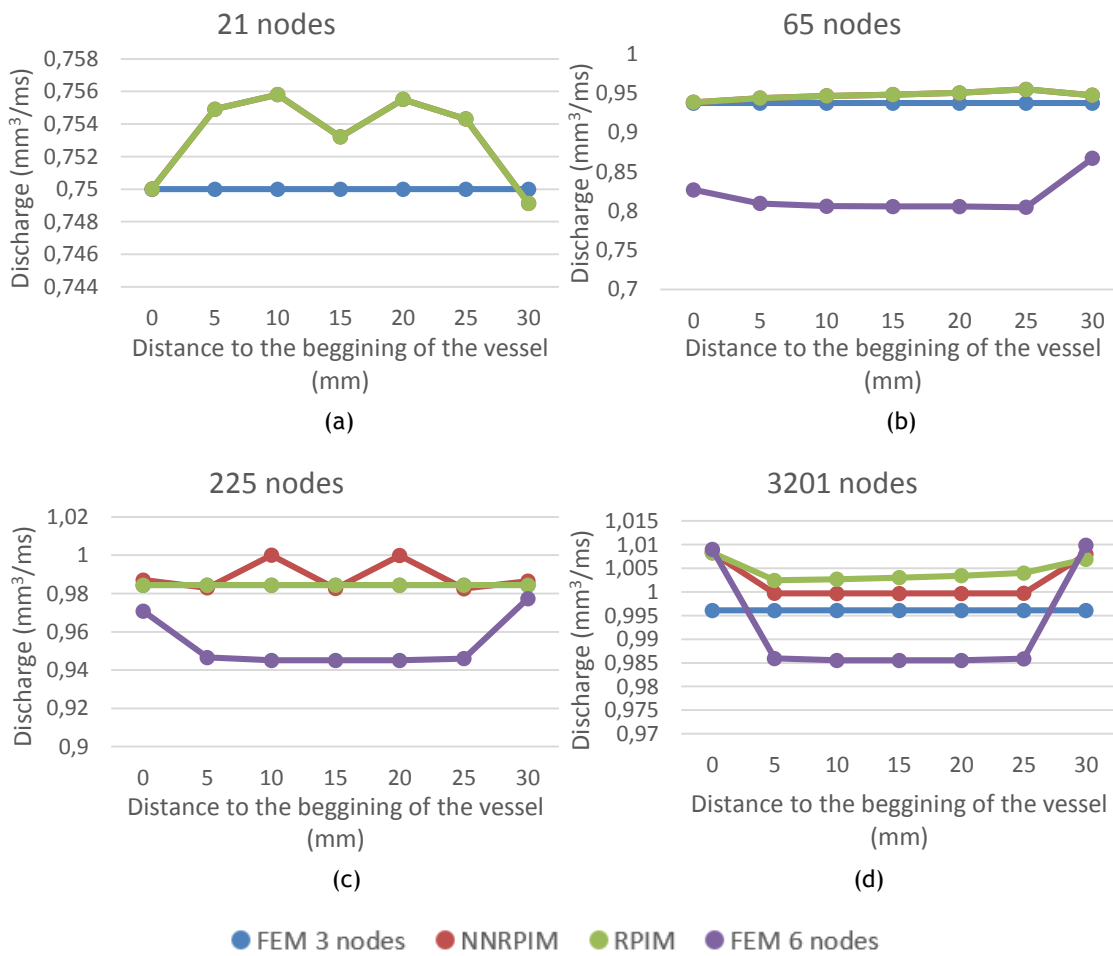
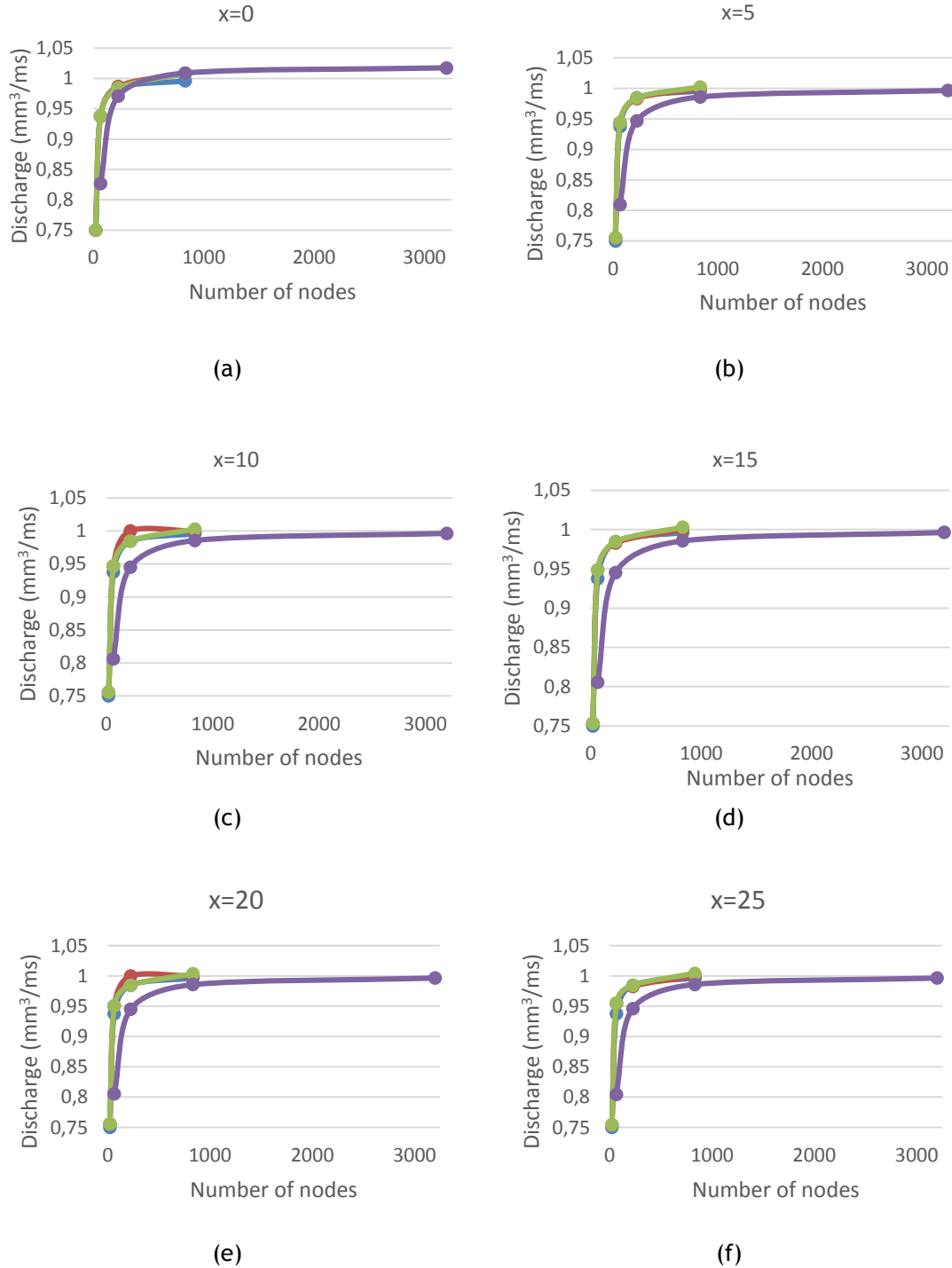


Figure 4.10 - Discharge in every cross section of the models
 a. 21 nodes b. 65 nodes c. 225 nodes d. 833 nodes

Comparing the discharge along the model, it is possible to observe that FEM with a 6-node element has an overall low discharge. The method that maintains a more constant discharge is FEM with a triangular element with 3 nodes. However, in the mesh with 3201 nodes analysed with NRPIM, the result is the closest to the theoretical and in the initial and last node, the difference is only 0,01 mm³/ms.

Figure 4.11 allows to compare the convergence of the discharge to the theoretical value.



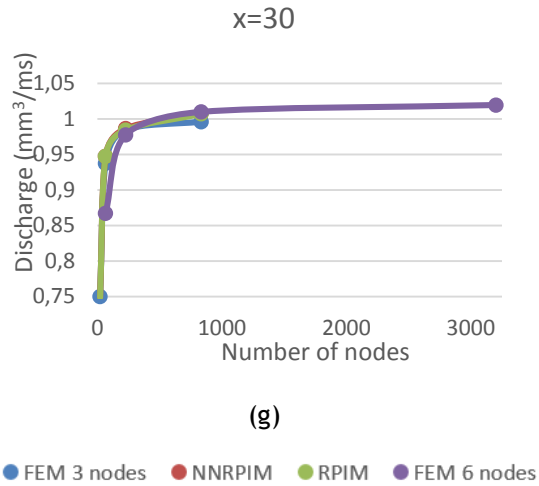
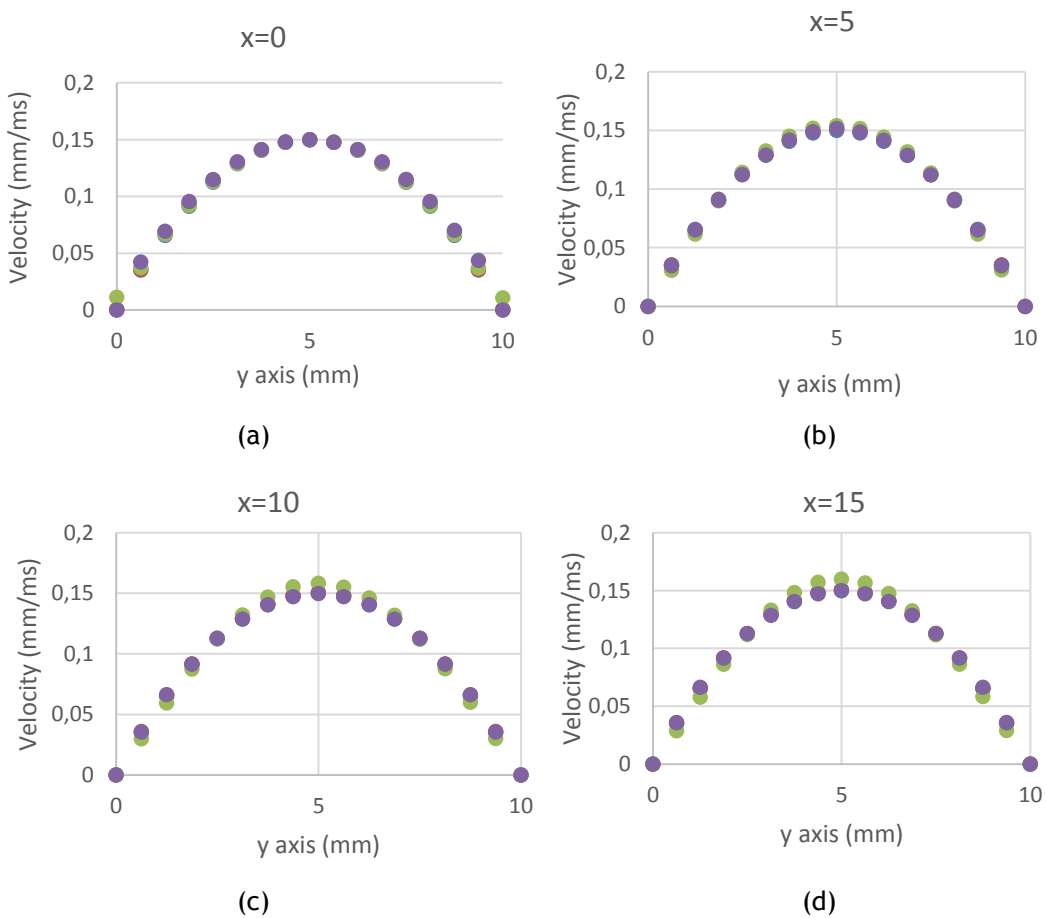


Figure 4.11 - Discharge in each cross session with different methodologies

a. x=0 b. x=5 c. x=10 d. x=15 e. x=20 f. x=25 g. x=30

The main conclusion withdrawn from these figures is that FEM with an element with 6 nodes is the one that converges more slowly.

Figure 4.12 illustrates the different velocity profiles.



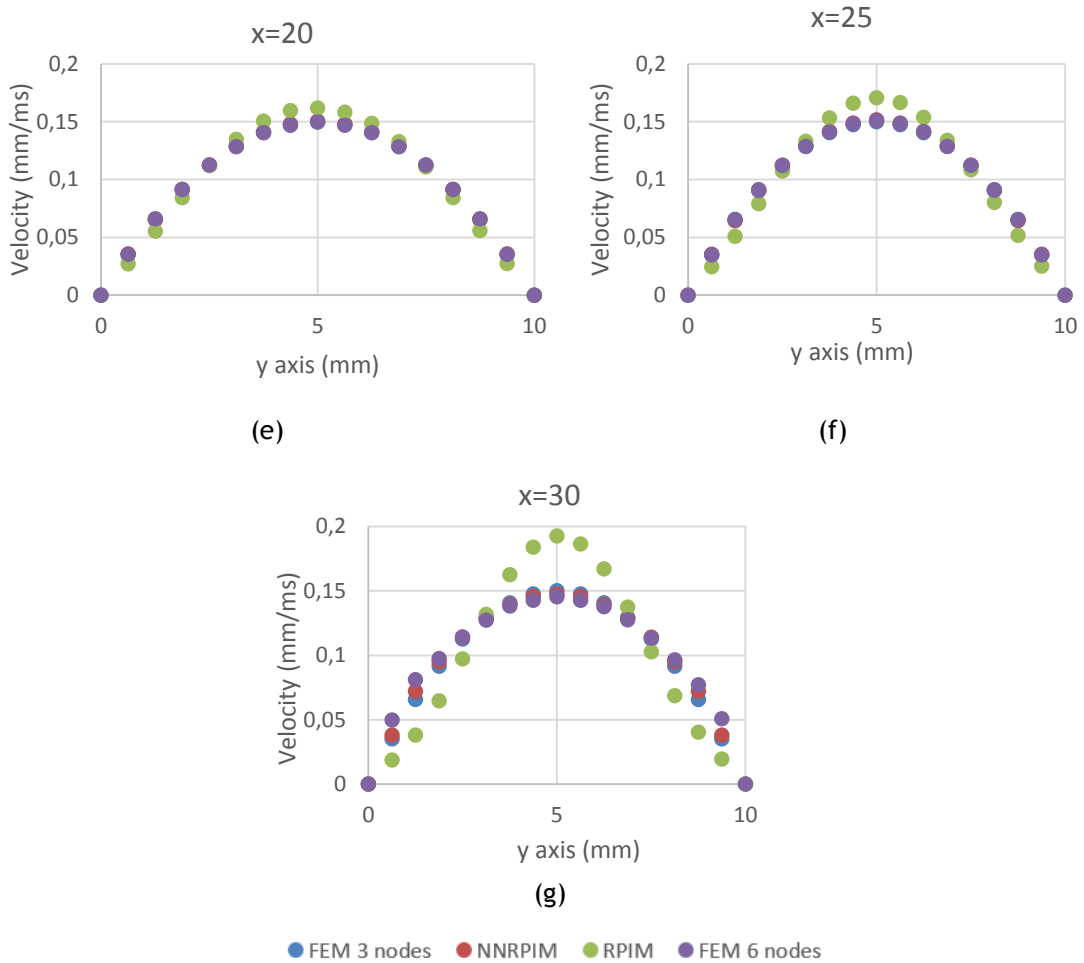


Figure 4.12 - Velocity profiles in each cross section with different methodologies

a. x=0 b. x=5 c. x=10 d. x=15 e. x=20 f. x=25 g. x=30

The velocity profiles do not differ significantly from each other, except in the last cross section, where RPIM is significantly different from the other methodologies.

As a final remark, in a linear model, FEM with a 3 nodes triangular element and NNRPIM have the best performance and prove to be efficient methods to simulate blood flow in this geometry.

4.1.2- Crescent cone model

The Figure 4.13 presents the first model. The meshes (a), (b), (c) and (d) with triangular elements with 3 nodes have, respectively, 21, 65, 255 and 833 elements. The same meshes with triangular elements with 6 nodes have, respectively, 65, 225, 833 and 3201 nodes.

The model has 30 mm of length and 10 mm of initial height, which increases to 14 mm. Following equation 7.3, the initial velocity profile is:

$$u(r) = 0.06r - 0.006(r)^2 \quad (4.8)$$

and therefore, the theoretical discharge should be:

$$\int_0^{10} (0.06x - 0.006x^2) dx = 1 \quad (4.9)$$

The Figure 4.13 shows the different levels of discretization studied.

4.1.2.1 Results

The results of the analysis with the different numerical methods are represented in Figure 4.14,

Figure 4.15, Figure 4.16, Figure 4.17 and Figure 4.18.

Since the discharge is supposed to be constant, with the increase of the height of the model, the maximum velocity is expected to decrease.

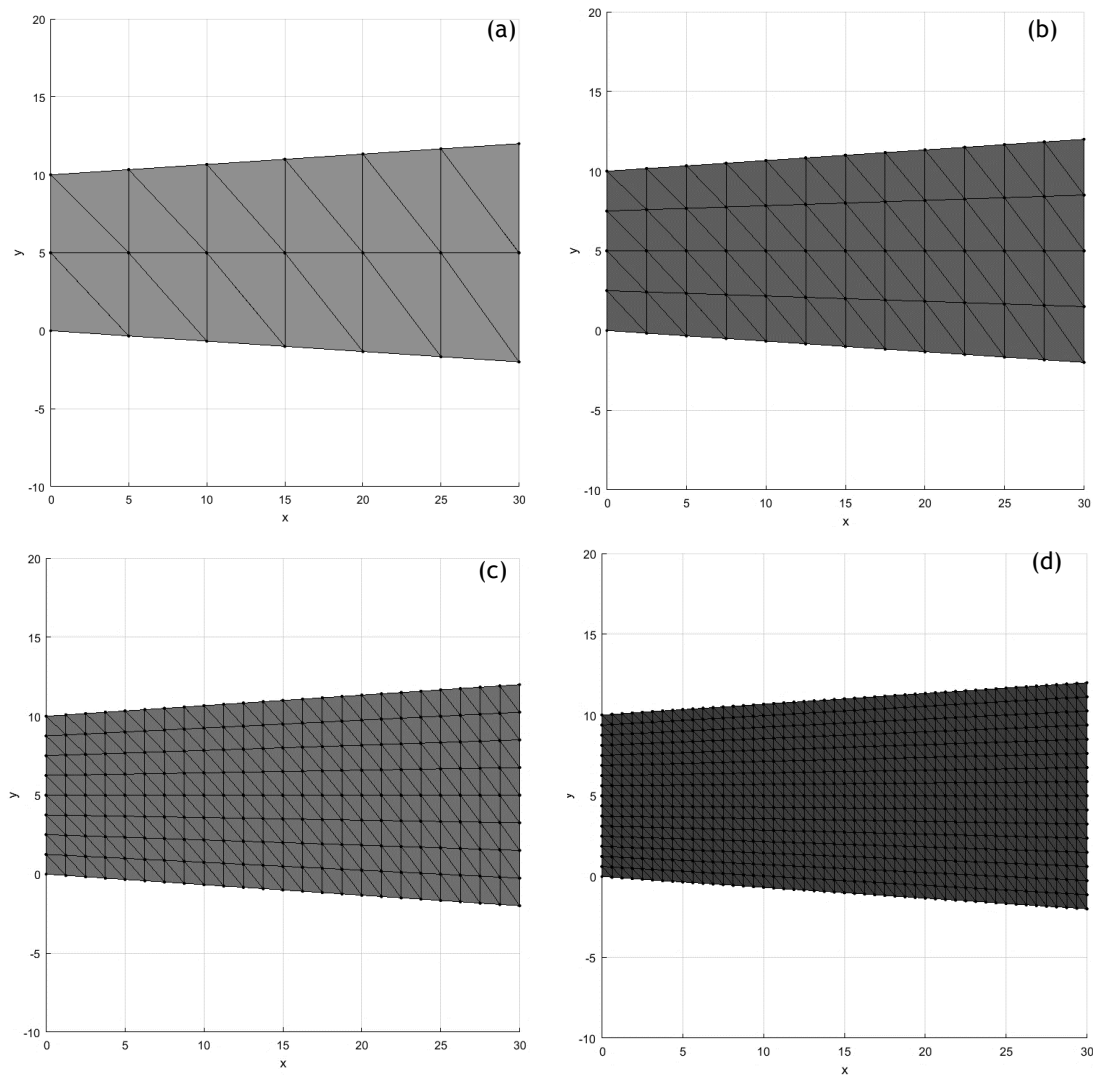


Figure 4.13 - Crescent cone model with different meshes

a. 24 elements b. 96 elements c. 384 elements d. 1536 elements

In

Figure 4.14 is presented the analysis with 21 nodes. The NNRPIM parameters are different from the default ones because the results with those parameters are not characteristic of a fluid flow. In this analysis, the parameter c is 1,42 and the parameter p is 1,03.

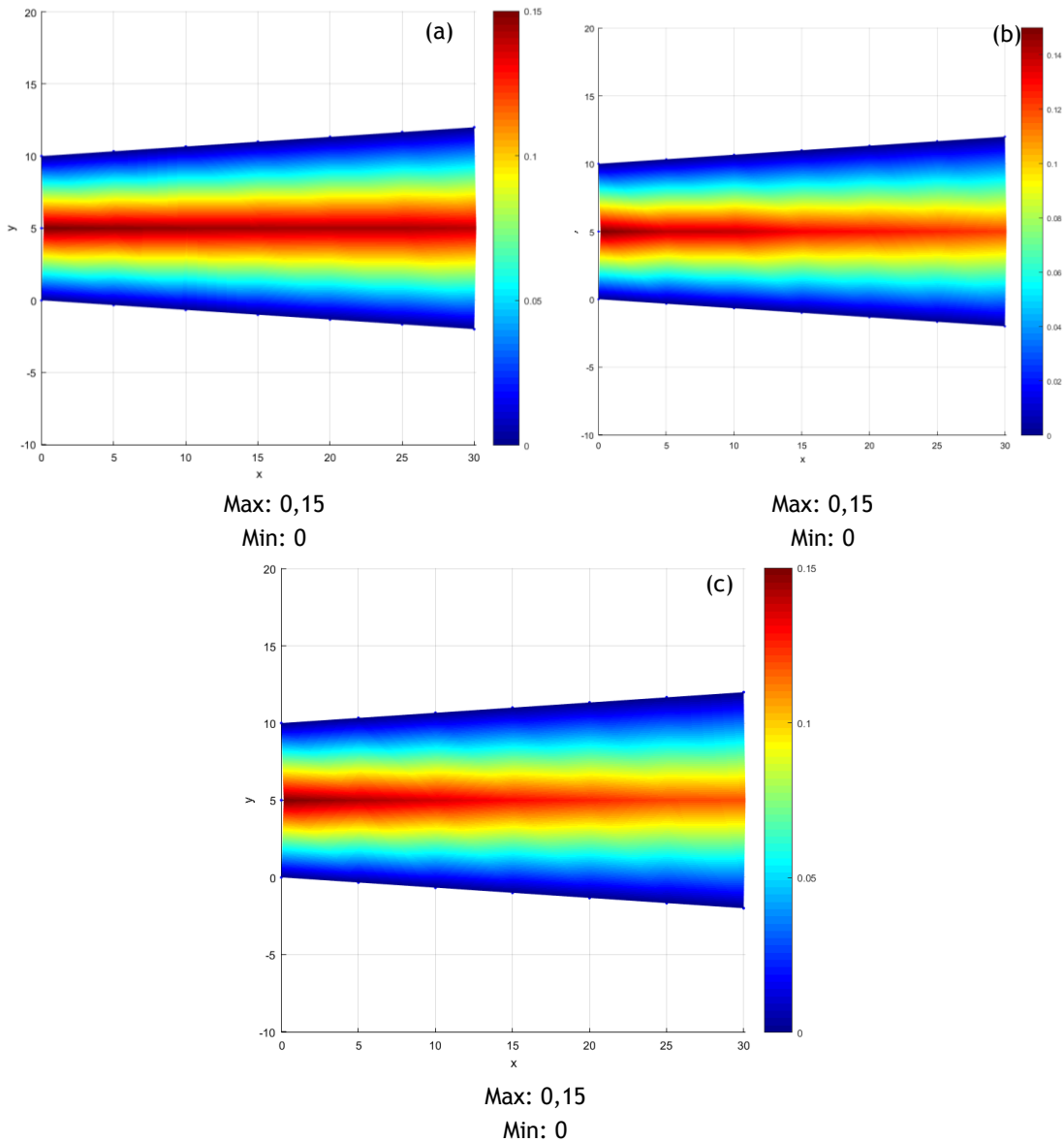


Figure 4.14 - Cone crescent model (21 nodes) analysed with different methods
a. FEM (triangular elements with 3 nodes) b. NNRPIM c. RPIM

In

Figure 4.15 is presented the velocity maps with 65 nodes. In this case the parameters of the RPIM and NNRPIM had to be adjusted as well. In NNRPIM, the parameter c is 1,42 and parameter p is 1.03 and in RPIM, the number of nodes inside the influence domain is 27 the

parameter c is 0,0001, parameter p is 0,9999 and Gauss number is 2. These parameters were changed after analysing the discharge with the default parameters was not constant.

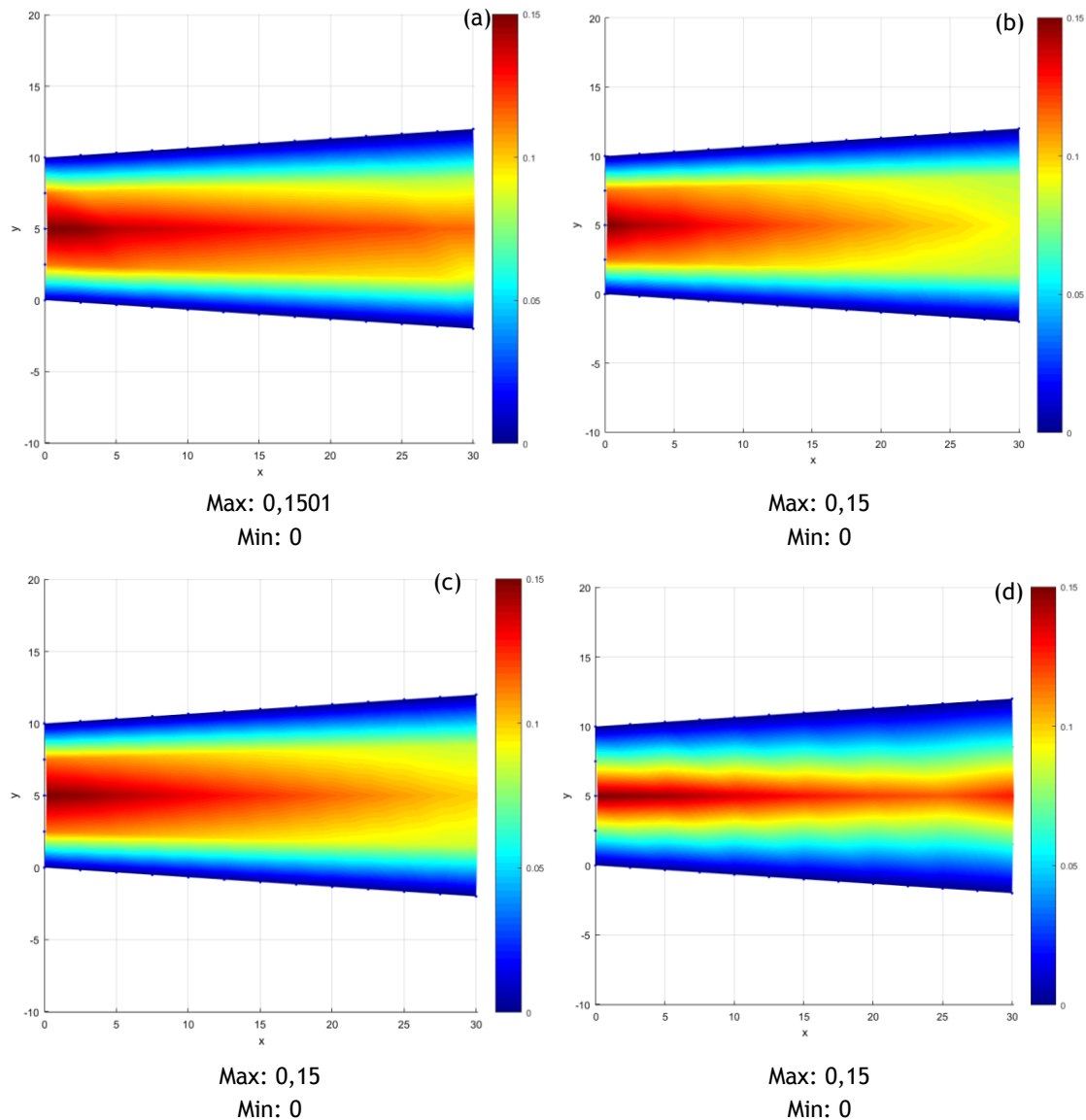


Figure 4.15 - Cone crescent model (65 nodes) analysed with different methods
 a. FEM (triangular elements with 3 nodes) b. NNRPIM c. RPIM d. FEM (triangular elements with 6 nodes)

Without numerical comparisons is not possible to take precise conclusions, but FEM with 6 nodes is significantly different from the other analysis.

In Figure 4.16 is represented the analysis with 255 nodes. In this case the NNRPIM parameters had to be adjusted, in resemblance with the analysis before. The parameter c is 1,42 and the parameter p is 1,03. The results with the default parameters were not typical of a fluid flow.

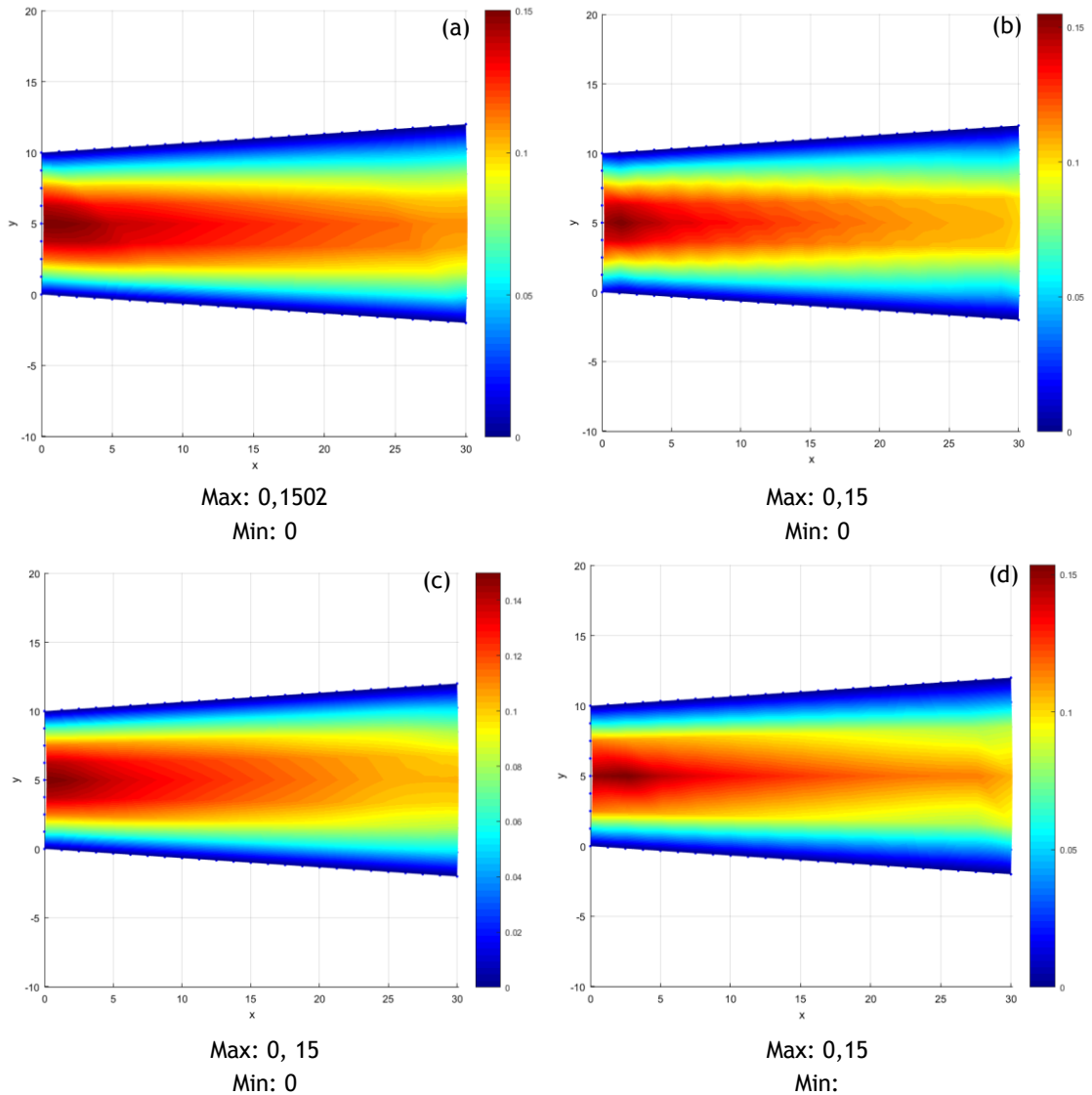


Figure 4.16 - Cone crescent model (255 nodes) analysed with different methods
 a. FEM (triangular elements with 3 nodes) b. NNRPIM c. RPIM d. FEM (triangular elements with 6 nodes)

In this analysis is possible to observe that the NNRPIM analysis has fluctuations compared with the other methods. In both FEM analysis, the images are not symmetrical, as they should be.

Figure 4.17 represents the numerical analysis with 833 nodes. In this case the parameters of the RPIM analysis had to be adjusted. The number of nodes inside the influence domain is 16, the parameter c is 0,0001, the parameter p is 0,9999 and the Gauss number is 2.

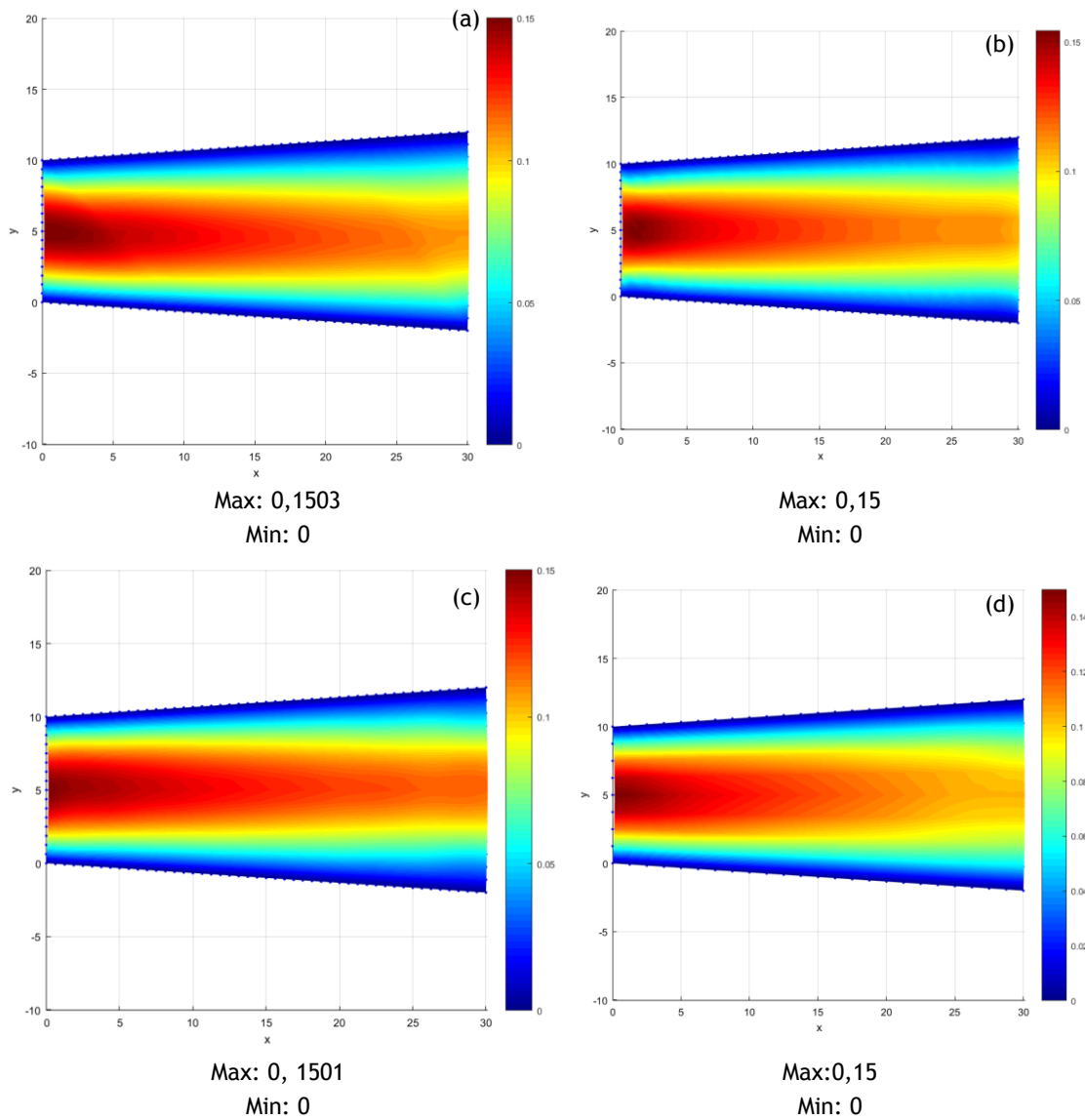
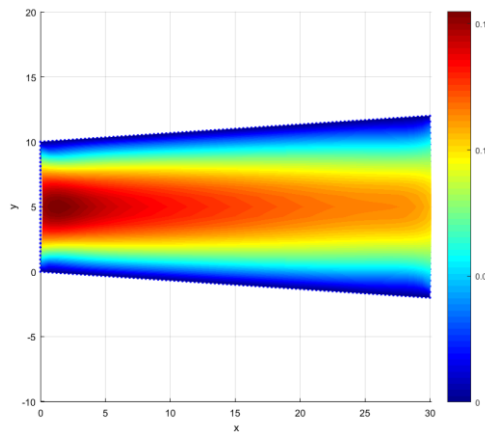


Figure 4.17 - Cone crescent model (833 nodes) analysed with different methods
 a. FEM (triangular elements with 3 nodes) b. NNRPIM c. RPIM d. FEM (triangular elements with 6 nodes)

Figure 4.18 represents the analysis with 6 nodes triangular FEM, with 3201 nodes.



Max: 0,15
Min: 0

Figure 4.18 - Cone crescent model (3201 nodes) analysed with FEM (triangular elements with 6 nodes)

The Figure 4.19 represents the discharge along the model.

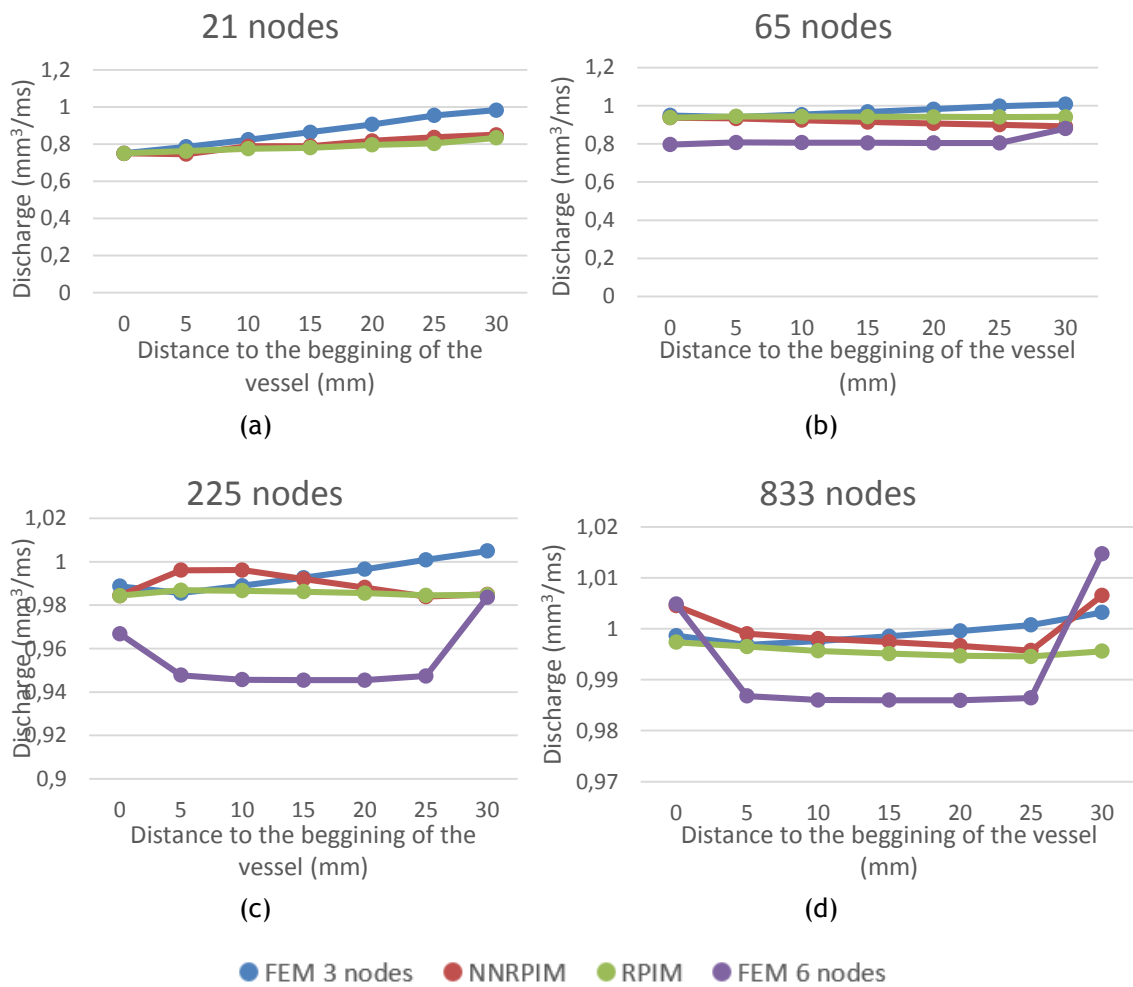
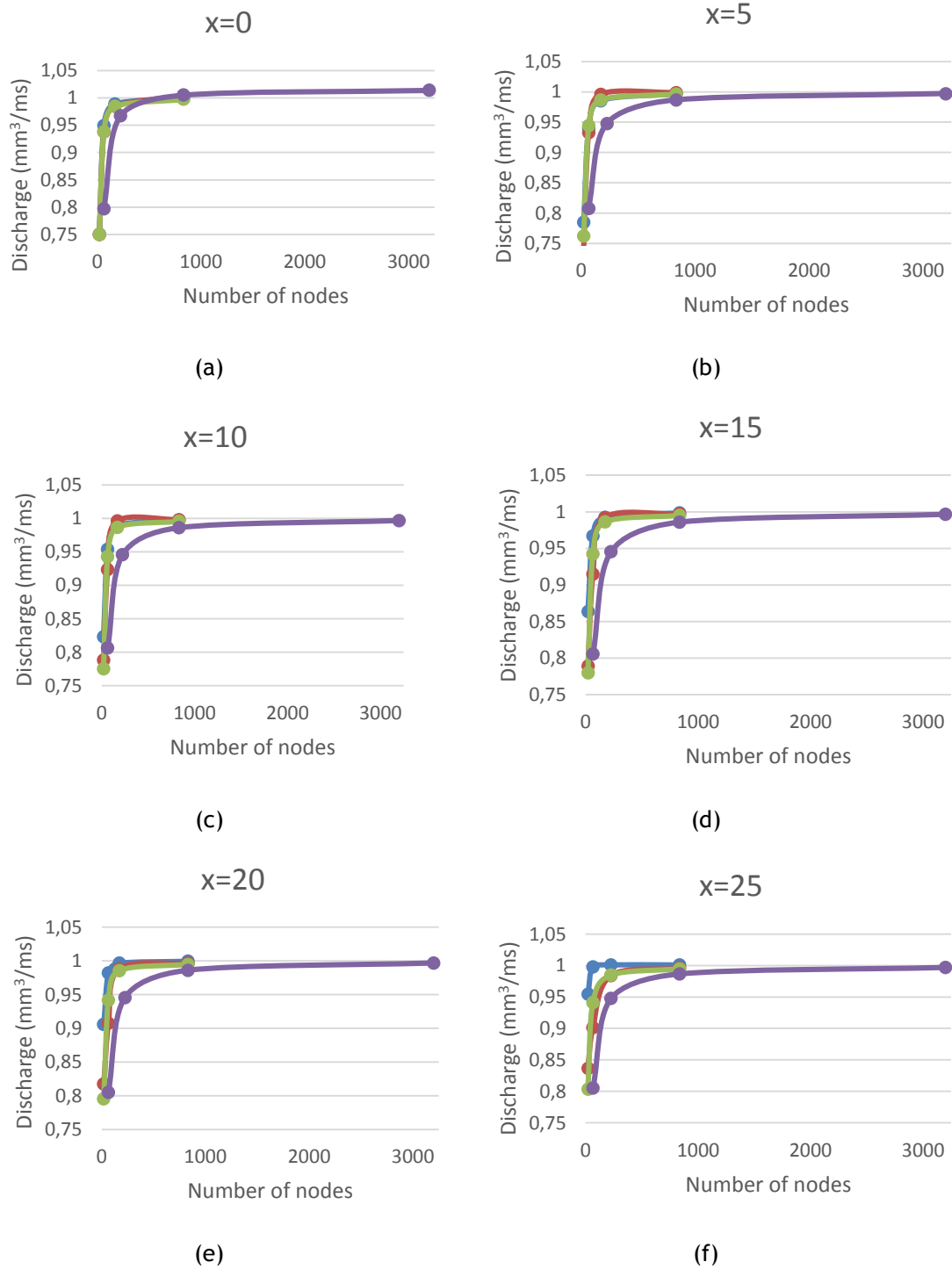


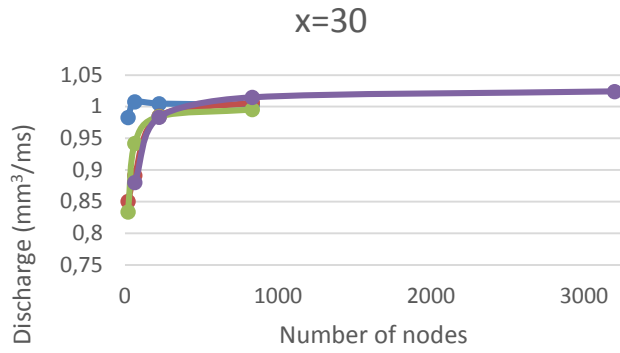
Figure 4.19 - Discharge in every cross section of the models

21 nodes b. 65 nodes c. 225 nodes d. 833 nodes

The goal of this study is to verify if the discharge is constant along the model. The results are very satisfying. In figure (a) the discharge is almost constant except FEM. In figure (b), the results are very close to the ones expected, except FEM with 6 nodes. In figure (c), the discharge of RPIM is almost constant and the discharge of FEM with 6 nodes is significantly below the other analysis. In (c) RPIM is the analysis more reliable, since is very close to 1 and is almost constant. FEM with 6 nodes is the analysis with the worst performance.

Figure 4.20 shows the discharge with each discretization level, for each methodology.





(g)

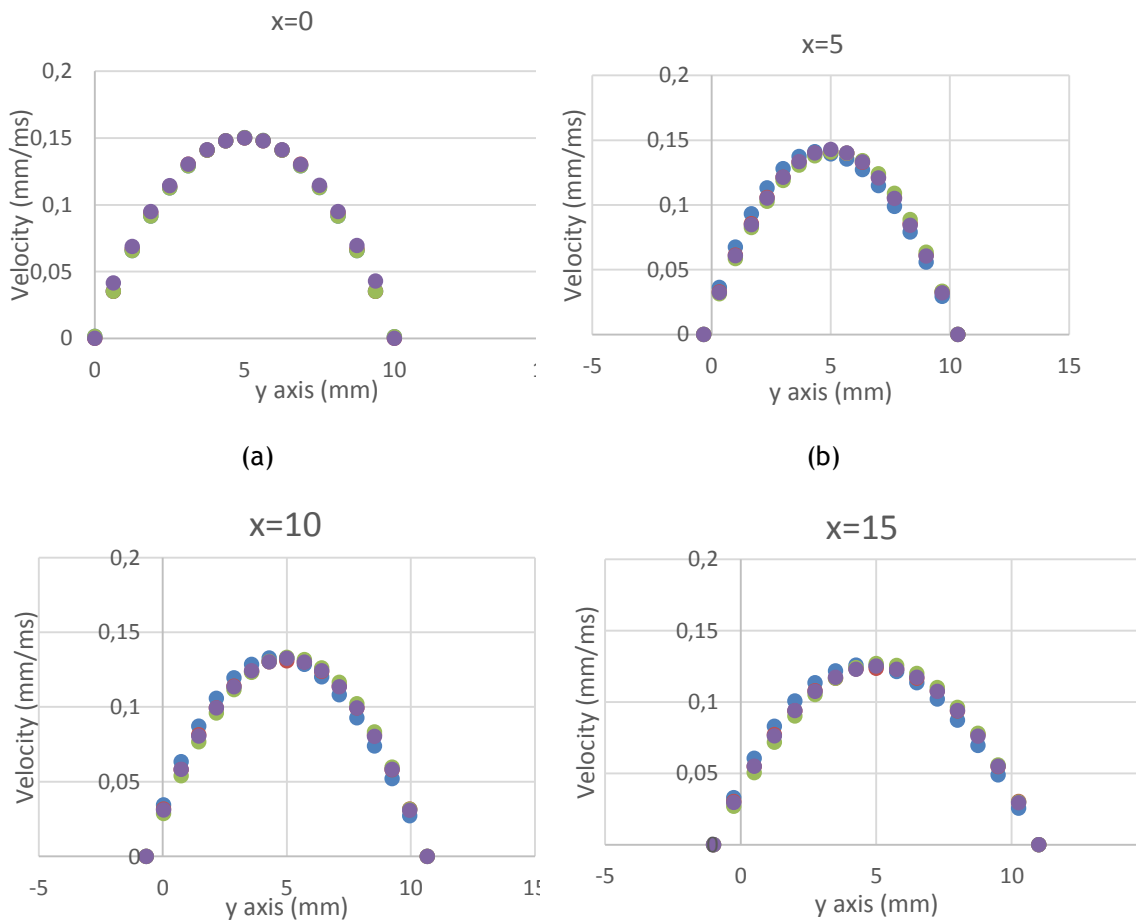
● FEM 3 nodes ● NNRPIM ● RPIM ● FEM 6 nodes

Figure 4.20 - Discharge in each cross session with different methodologies

a. x=0 b. x=5 c. x=10 d. x=15 e. x=20 f. x=25 g. x=30

Looking for the figures, it is possible to conclude that the FEM with 6 nodes elements is the last one to converge.

The Figure 4.21 presents the velocity profiles with 833 nodes, which was the level of discretization with the discharge closer to the theoretical.



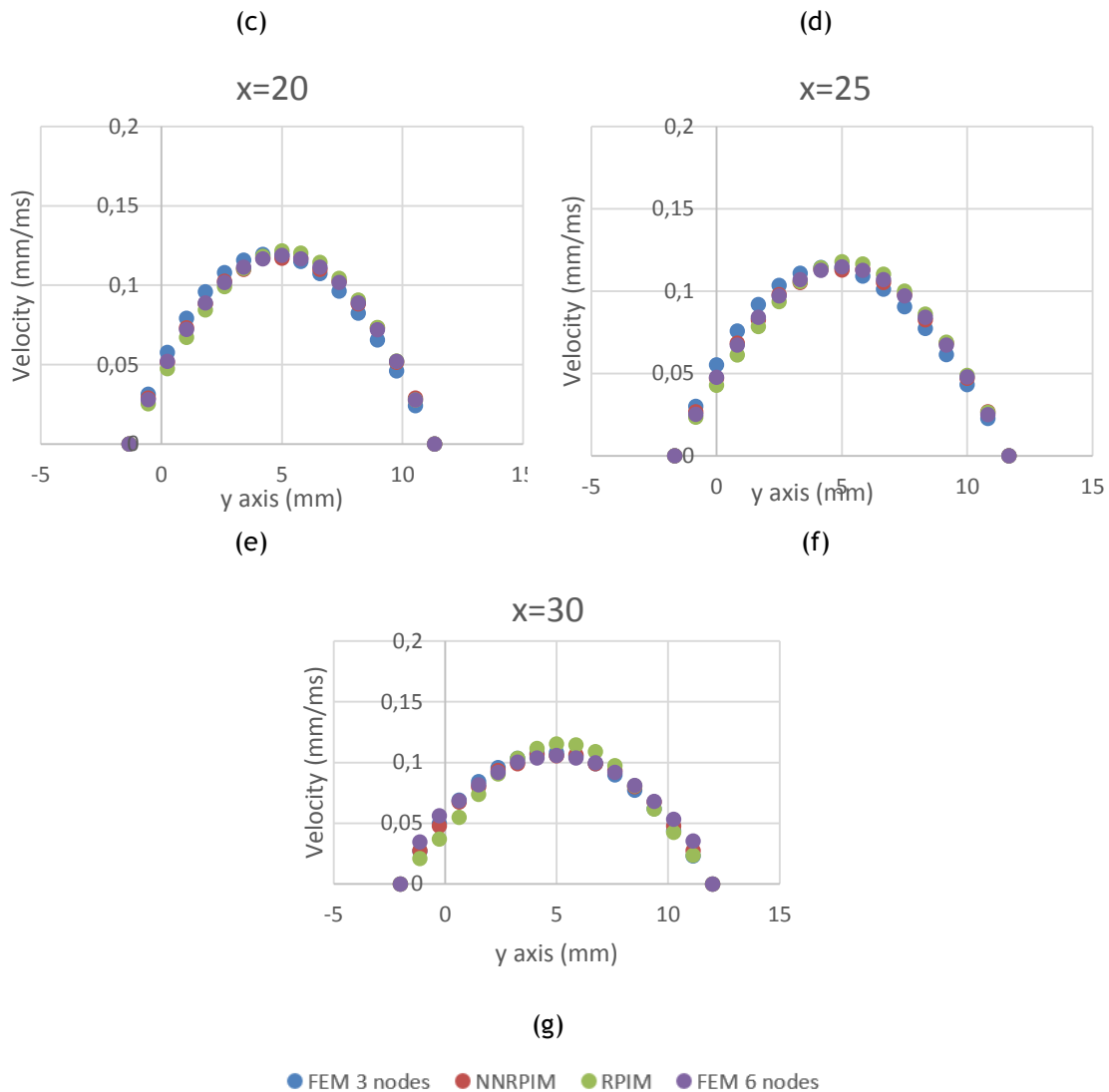


Figure 4.21 - Velocity profiles in each cross session with different methodologies

a. x=0 b. x=5 c. x=10 d. x=15 e. x=20 f. x=25 g. x=30

The velocity profiles are very similar.

Conjugating the three comparisons, it is possible to conclude that FEM with a 3 nodes element, NNRPIM and RPIM are viable solutions to simulate blood flow in this geometry.

4.1.3- Cone decrescent model

The Figure 4.22 presents the first model. The meshes (a), (b), (c) and (d) with triangular elements with 3 nodes have, respectively, 21, 65, 255 and 833 elements. The same meshes with triangular elements with 6 nodes have, respectively, 65, 225, 833 and 3201 nodes. The model has 30 mm of length and 14 mm of initial height, which decreases to 10 mm. Following equation 7.3, the initial velocity profile is:

$$u(r) = 0.0429r - 0.0031r^2 \quad (4.10)$$

and therefore, the theoretical discharge should be:

$$\int_0^{14} (0.0429x - 0.0031x^2) dx = 1.36873 \quad (4.11)$$

The Figure 4.22 shows the different levels of discretization studied.

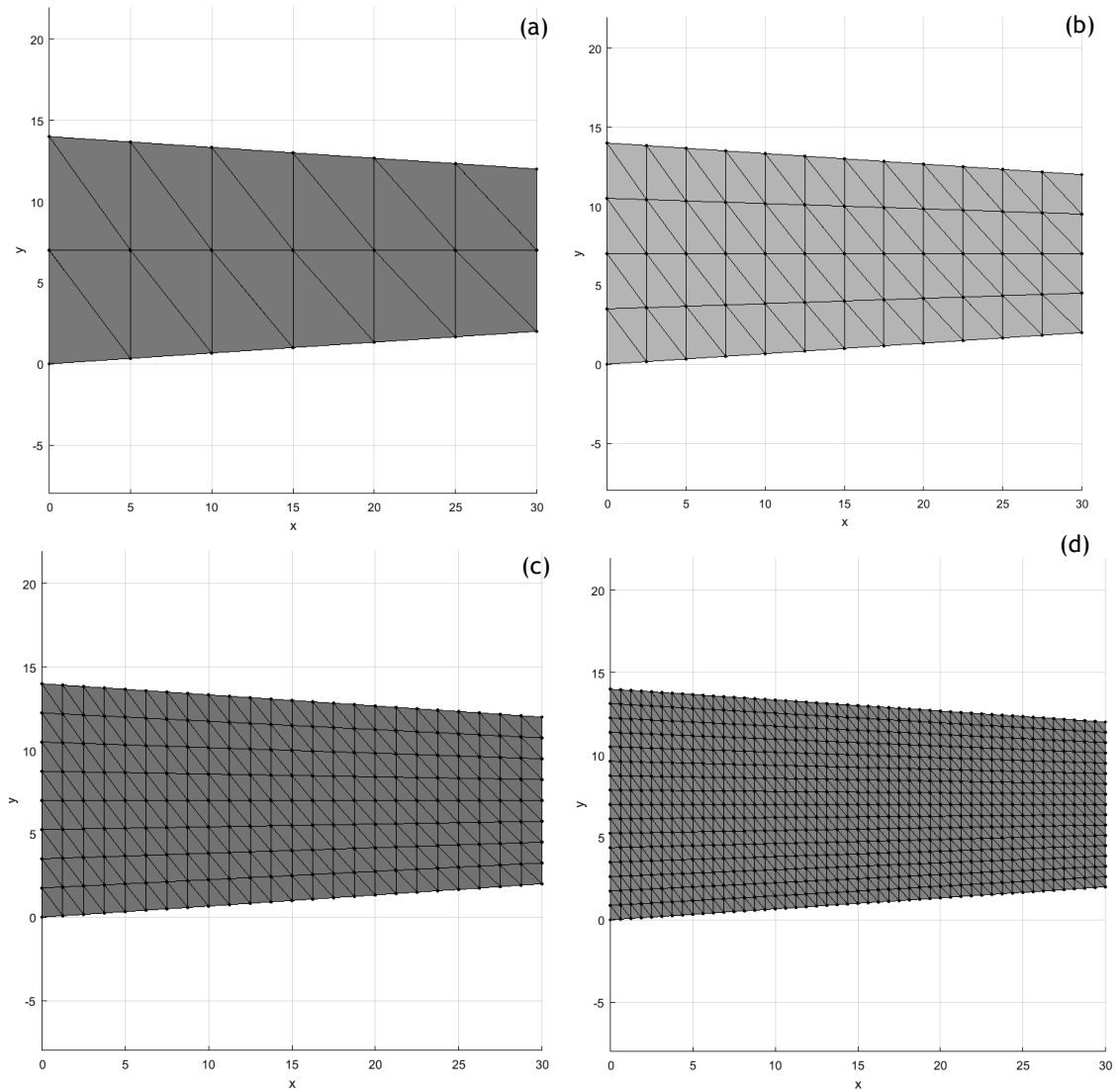


Figure 4.22 - Decrescent cone model with different meshes

a. 24 elements b. 96 elements c. 384 elements d. 1536 elements

4.1.5.1 - Results

The results of the analysis with the different numerical methods are represented in Figure 4.23, Figure 4.24,

Figure 4.25 and Figure 4.26.

Since the discharge is supposed to be constant, with the increase of the height of the model, the maximum velocity is expected to decrease.

In Figure 4.23 is presented the analysis with 21 nodes. In this analysis, for NNRPIM, the parameter c is 1,42 and parameter c is 1.03.

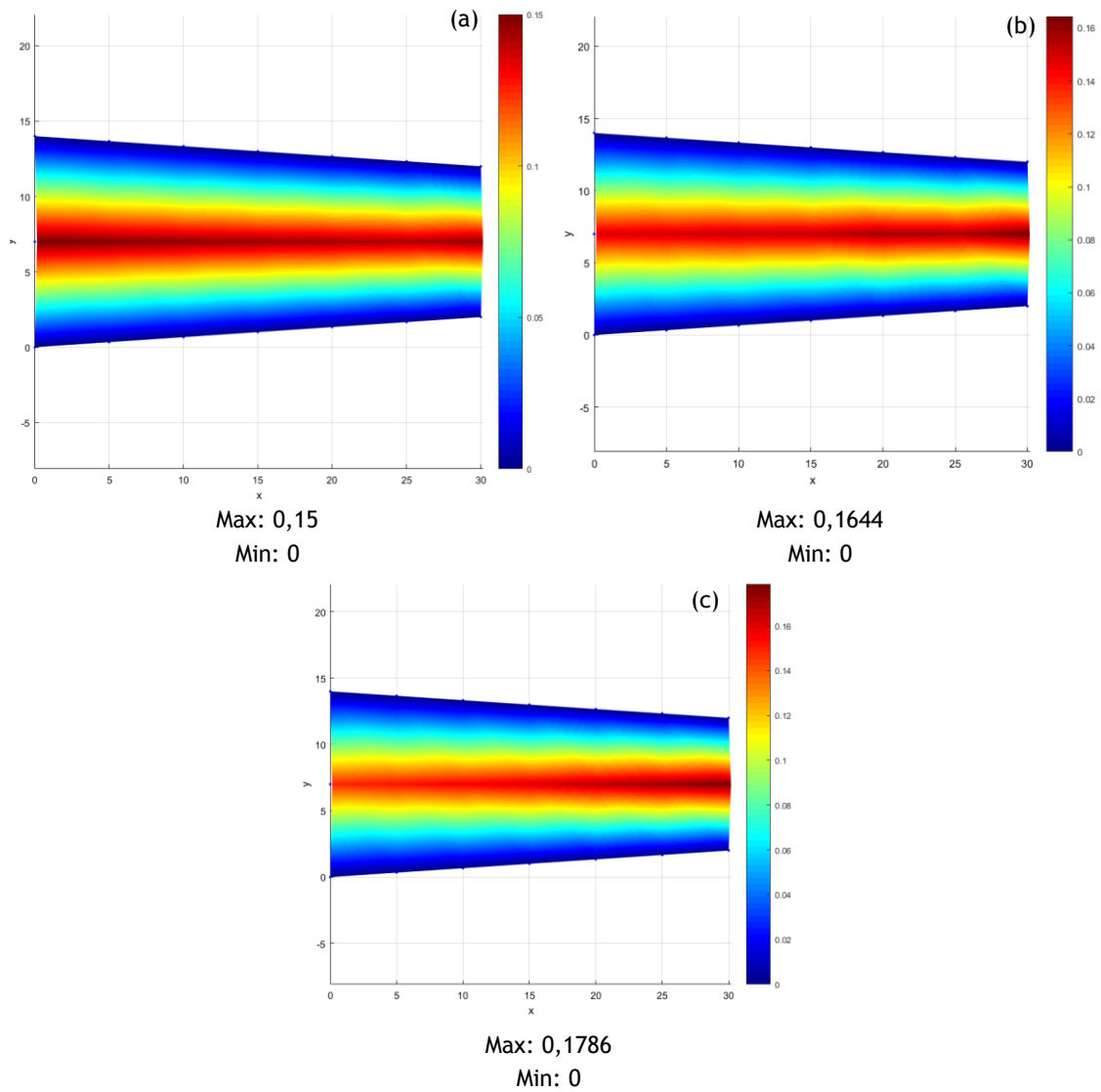
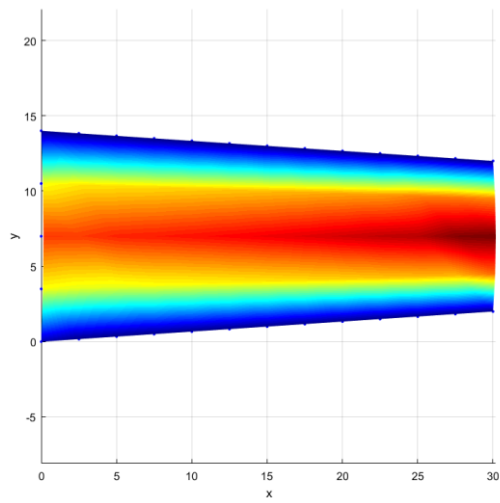


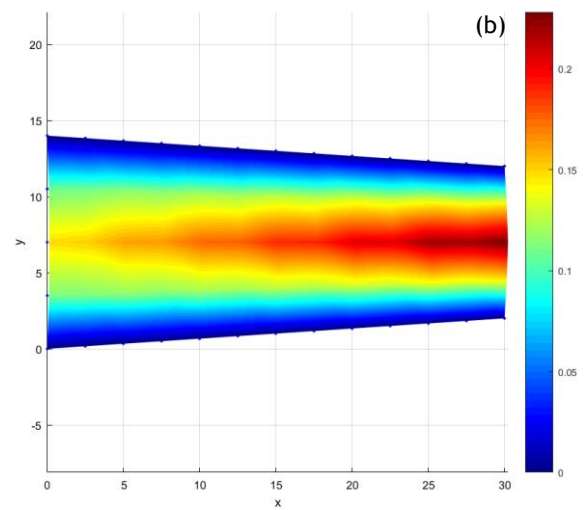
Figure 4.23 - Cone decreasing model (21 nodes) analysed with different methods
 a. FEM (triangular elements with 3 nodes) b. NNRPIM c. RPIM d. FEM (triangular elements with 6 nodes)

In Figure 4.24 is presented the analysis with 65 nodes.

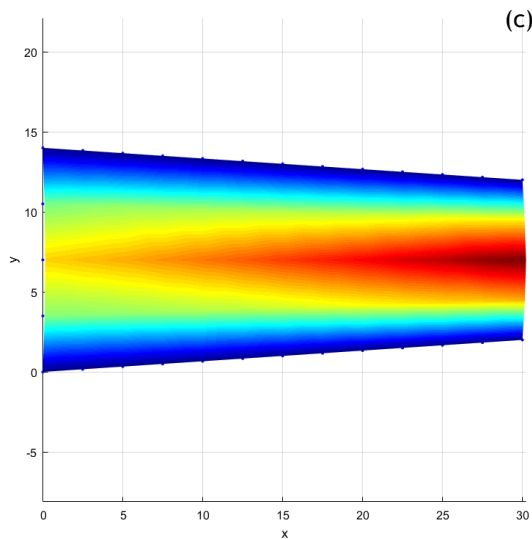
(a)



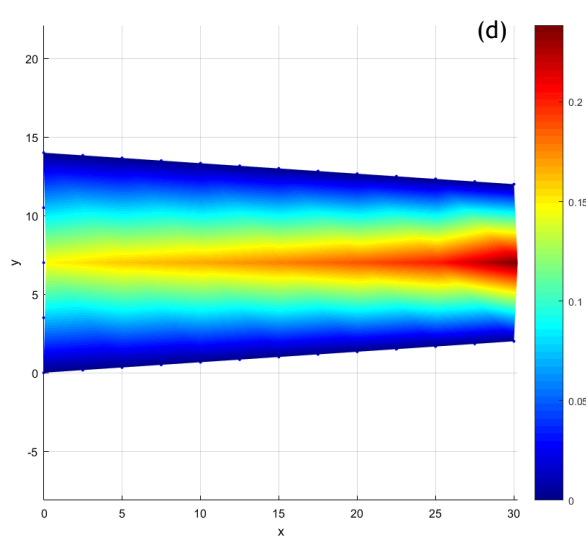
Max: 0,1843
Min: 0



Max: 0,2282
Min: 0



Max: 0,2248
Min: 0



Max: 0,2385
Min: 0

Figure 4.24 - Cone decrescent model (65 nodes) analysed with different methods

a. FEM (triangular elements with 3 nodes) b. NNRPIM c. RPIM d. FEM (triangular elements with 6 nodes)

In

Figure 4.25 is presented the analysis with 225 nodes. In this analysis, RPIM parameters were adjusted. The number of nodes inside the influence domain is 27, the parameter c is 0,0001, parameter p is 0,9999 and gauss number is 2.

In Figure 4.26 is presented the analysis with 833 nodes. In this analysis, RPIM parameters were adjusted. The number of nodes inside the influence domain is 27, the parameter c is 0,0001, parameter p is 0,9999 and gauss number is 2.

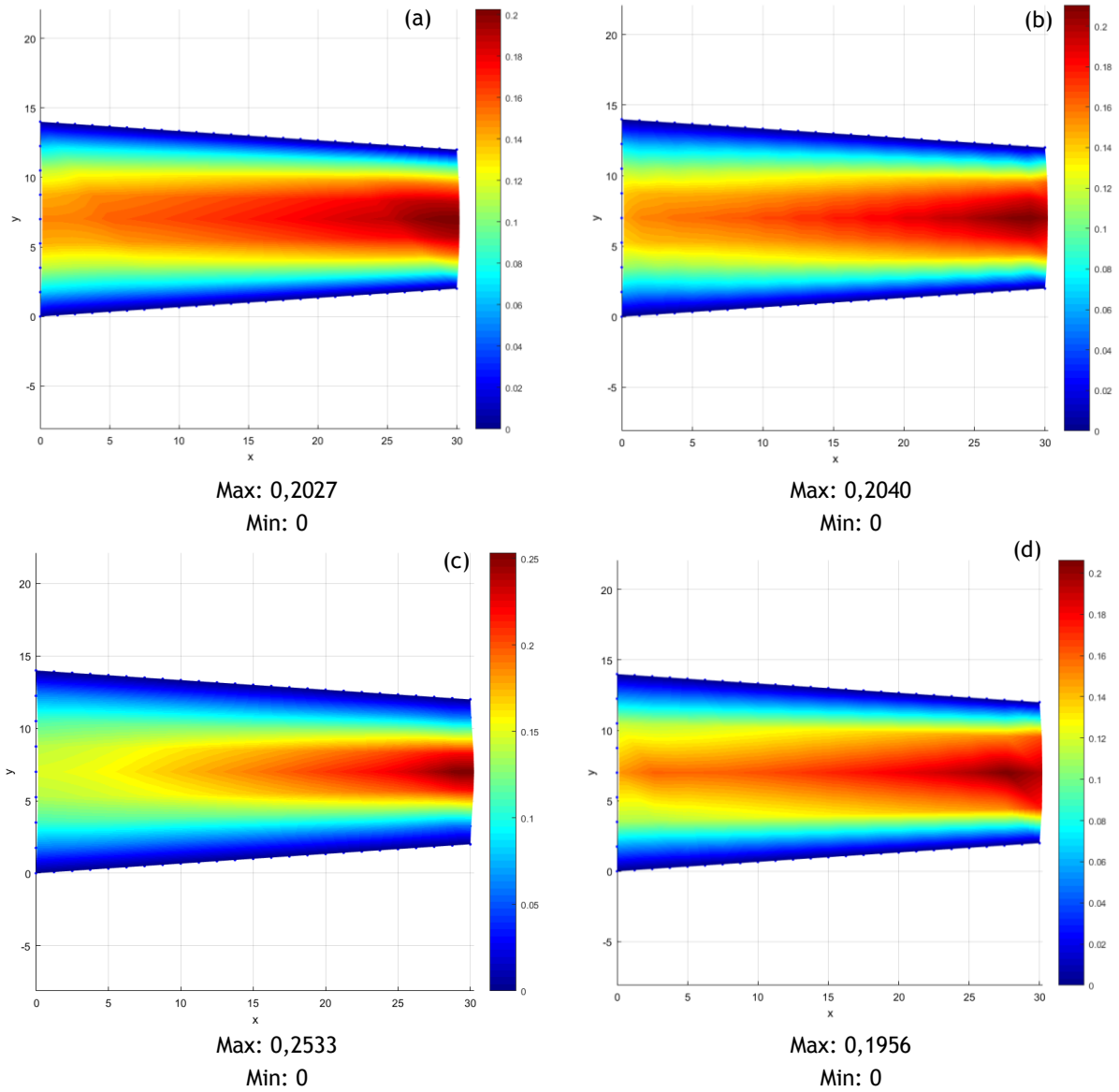


Figure 4.25 - Cone descent model (225 nodes) analysed with different methods
 a. FEM (triangular elements with 3 nodes) b. NNRPIM c. RPIM d. FEM (triangular elements with 6 nodes)

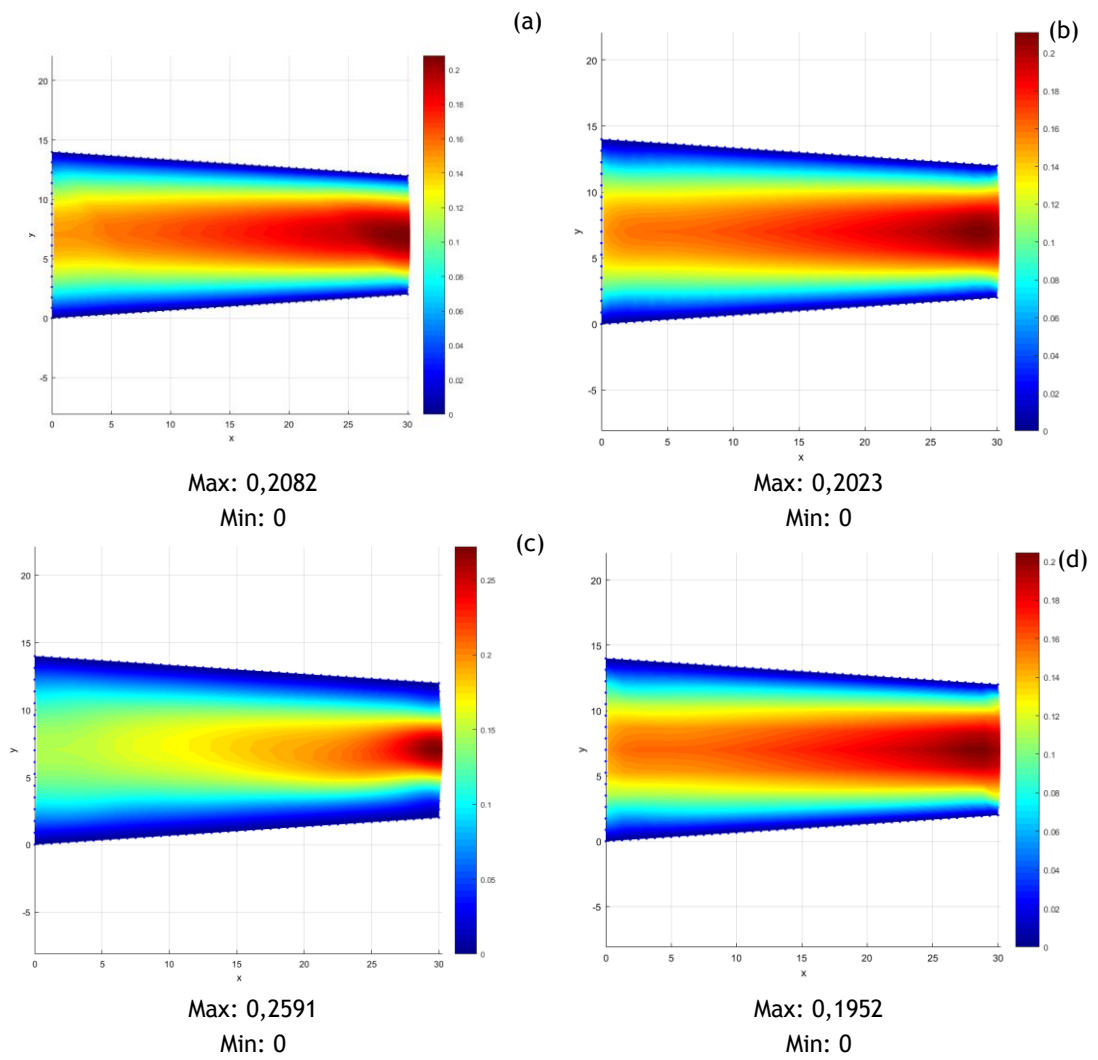


Figure 4.26 - Cone decrescent model (833 nodes) analysed with different methods
a. FEM (triangular elements with 3 nodes) b. NNRPIM c. RPIM d. FEM (triangular elements with 6 nodes)

In Figure 4.27 is presented the analysis with 3201 nodes

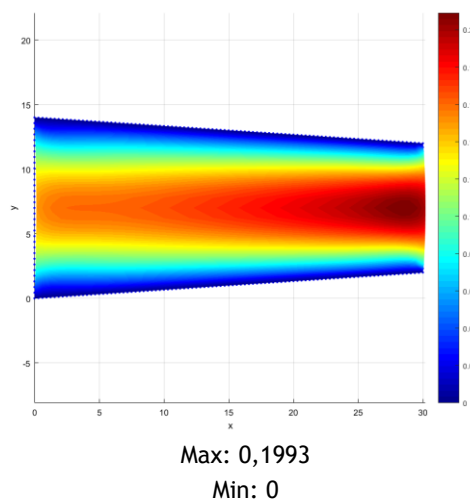


Figure 4.27 - Cone decrescent model (3201 nodes) analysed with FEM (triangular elements with 6 nodes)

The Figure 4.28 represents the discharge along the model.

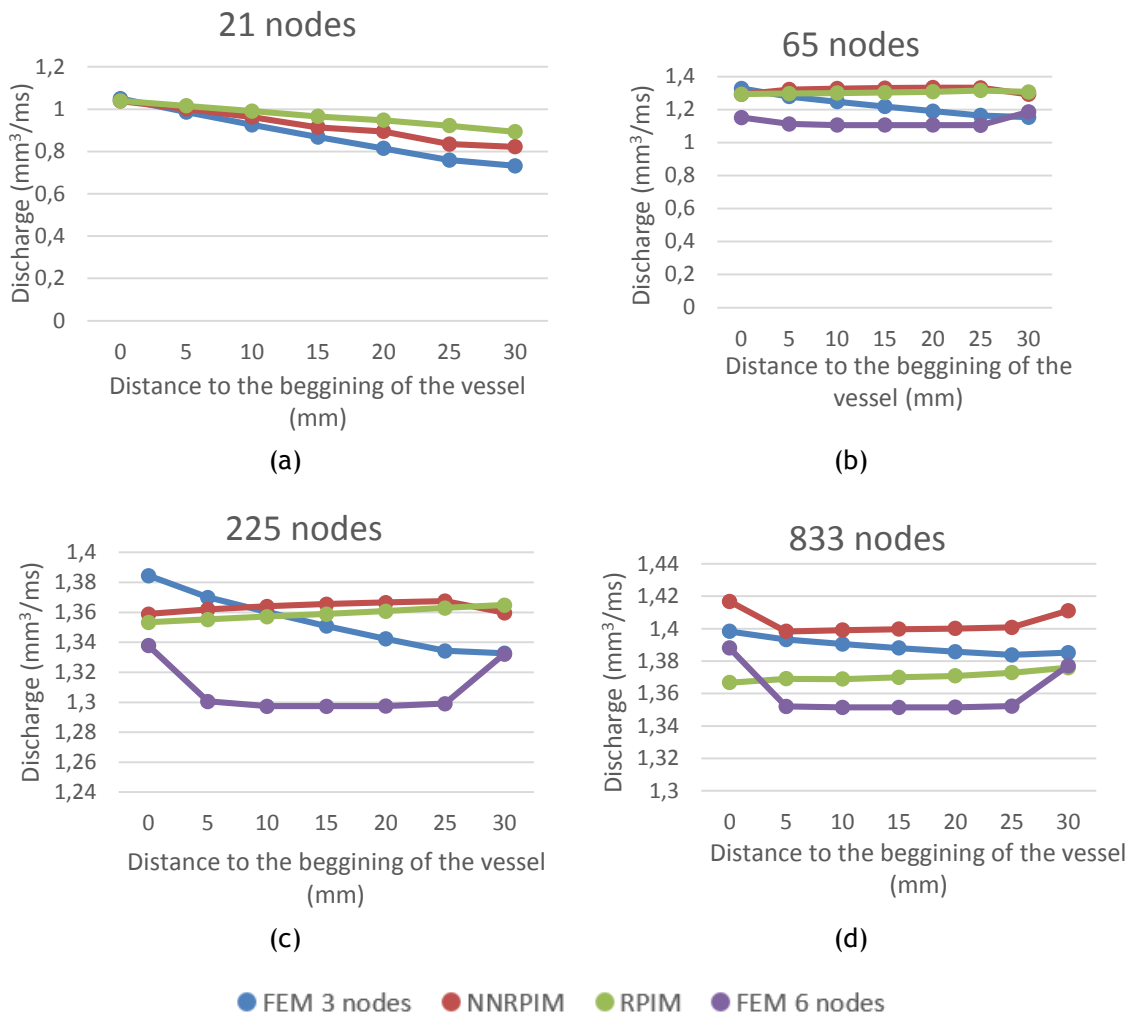
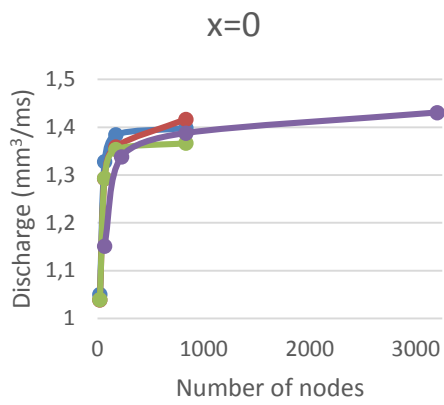


Figure 4.28 - Discharge in every cross section of the models

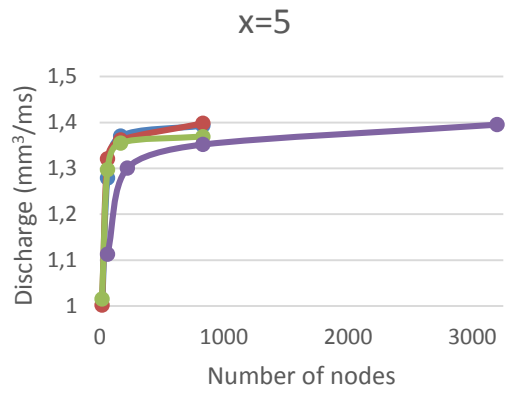
21 nodes **b.** 65 nodes **c.** 225 nodes **d.** 833 nodes

As mentioned before, the expected discharge is 1,369 mm³/ms. It is possible to observe that with only 65 nodes, the results are very close to the ones expected. NNRPIM and RPIM are very constant with 65 nodes, 225 nodes and 833 nodes and this last one is closest to the expected value. 6 elements FEM is the least constant and NNRPIM is the least close to the expected value.

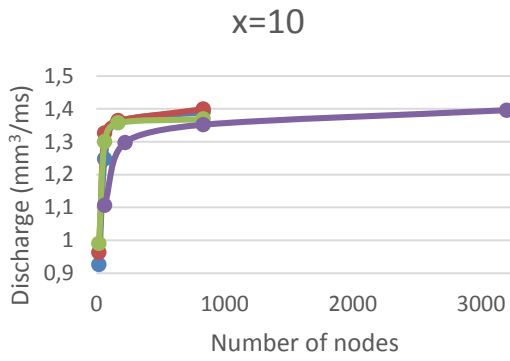
Figure 4.29 shows the discharge with each discretization level, for each methodology.



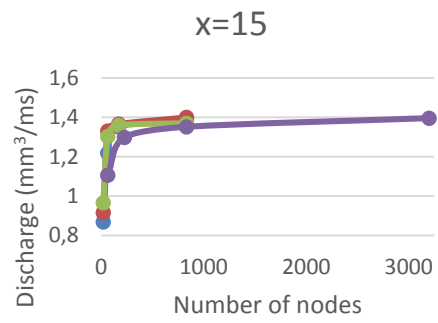
(a)



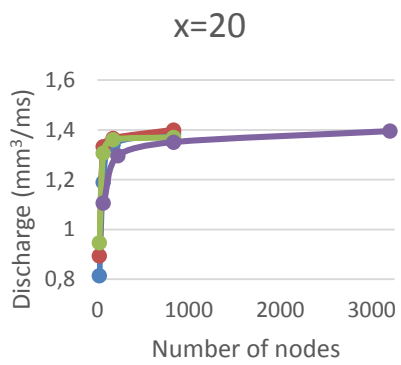
(b)



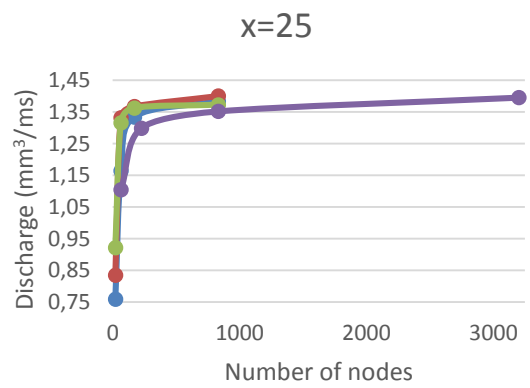
(c)



(d)



(e)



(f)

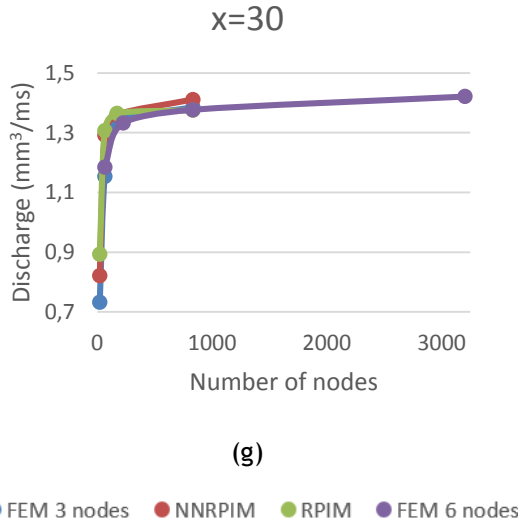
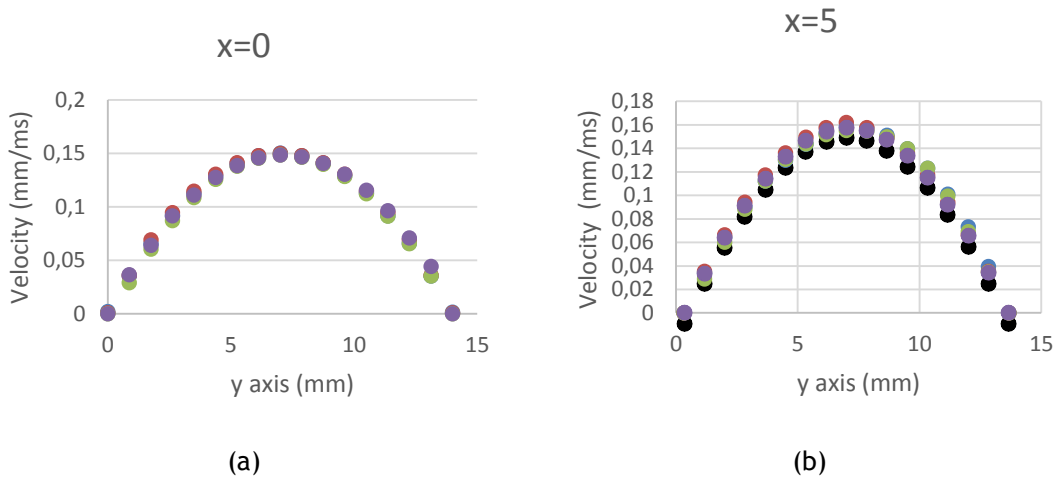


Figure 4.29 - Discharge in each cross session with different methodologies

a. x=0 b. x=5 c. x=10 d. x=15 e. x=20 f. x=25 g. x=30

This analysis shows that the 6 nodes element FEM presents the worst performance, since is the last method to converge.

The Figure 4.21 presents the velocity profiles with 833 nodes, which was the level of discretization with the discharge closer to the theoretical.



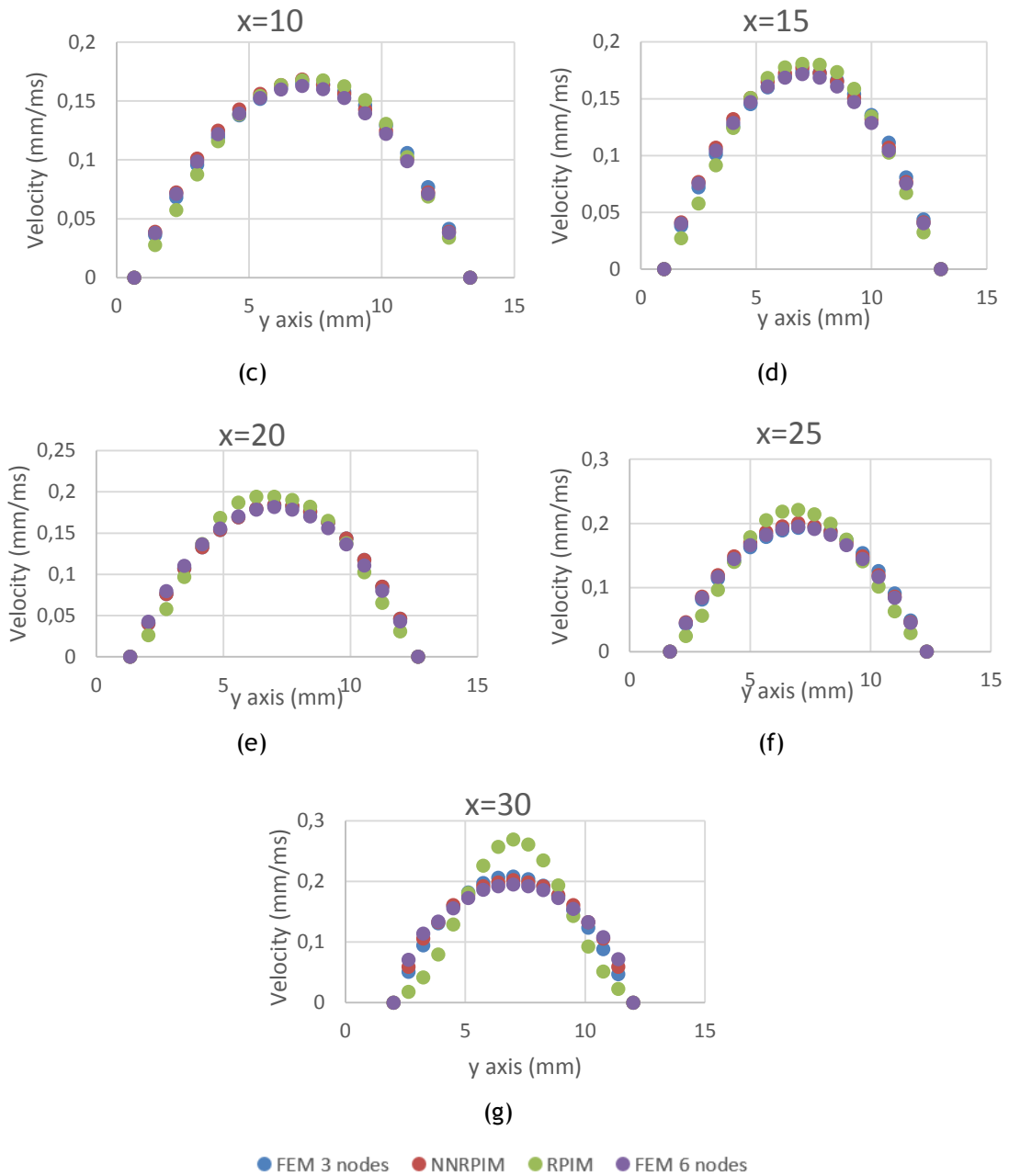


Figure 4.30 - Velocity profiles in each cross section with different methodologies

a. x=0 b. x=5 c. x=10 d. x=15 e. x=20 f. x=25 g. x=30

The velocity profiles are very similar, except the last two, in which the RPIM shows higher velocities than the other techniques. The outlet velocity expected is around 0,2 mm/ms. Therefore, the RPIM produces the worst results. As it is expected, the velocity increases with the distance from the beginning of the model.

Analysing all the factors, the FEM with a 3-element node is the best method in this case.

4.1.4- Quarter of a circular crown model

The Figure 4.31 presents the first model. The meshes (a), (b), (c) and (d) with triangular elements with 3 nodes have, respectively, 21, 65, 255 and 833 elements. The same meshes with triangular elements with 6 nodes have, respectively, 65, 225, 833 and 3201 nodes. The model has an inner radius of 20 mm and an outer radius of 30 mm. Following equation 7.3, the initial velocity profile is:

$$u(r) = 0.06r - 0.006(r)^2 \quad (4.12)$$

and therefore, the theoretical discharge should be:

$$\int_0^{10} (0.06x - 0.006x^2) dx = 1 \quad (4.13)$$

The Figure 4.31 shows the different levels of discretization studied.

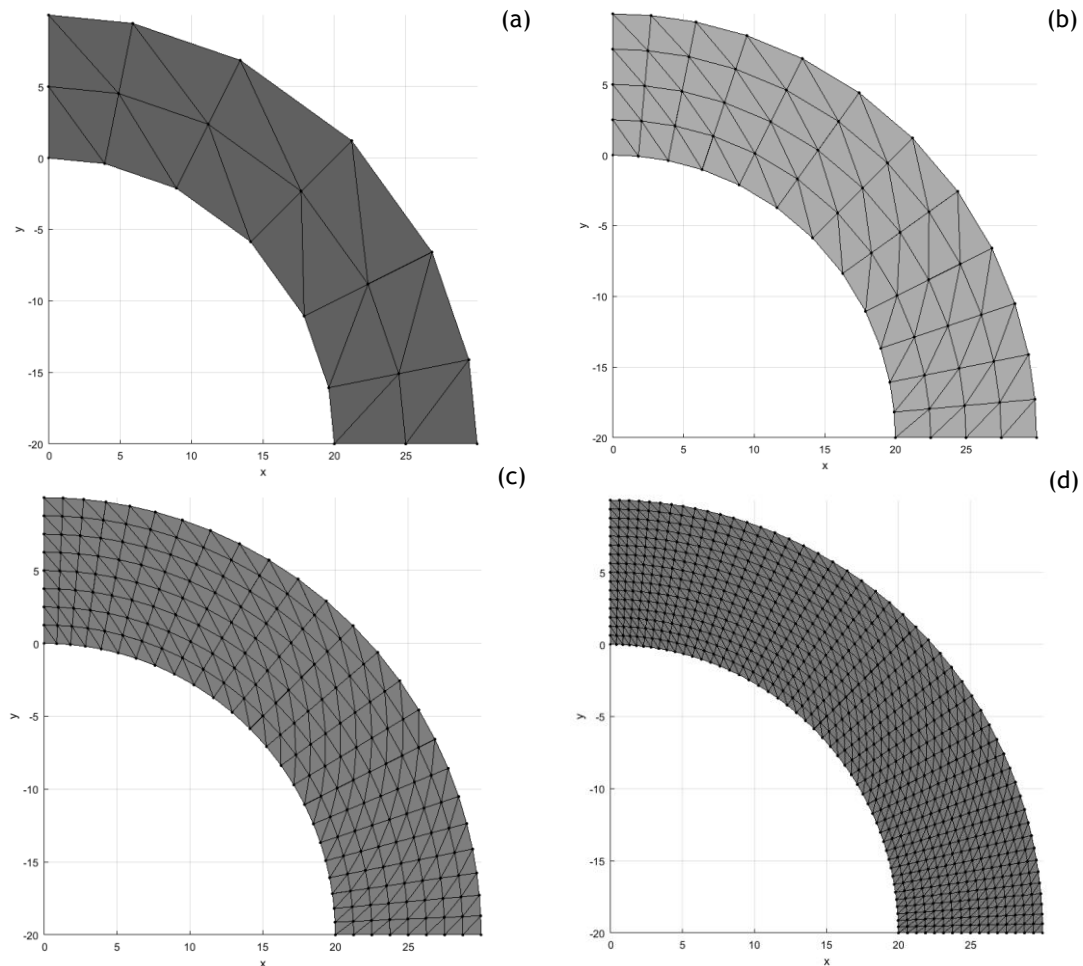


Figure 4.31 - Quarter of a circular crown model with different meshes

a. 24 elements b. 96 elements c. 384 elements d. 1536 elements

4.1.4.1- Results

The results of the analysis with the different numerical methods are represented in Figure 4.32,

Figure 4.33, Figure 4.34,

Figure 4.35 and

Figure 4.36.

In Figure 4.32 is presented the analysis with 21 nodes.

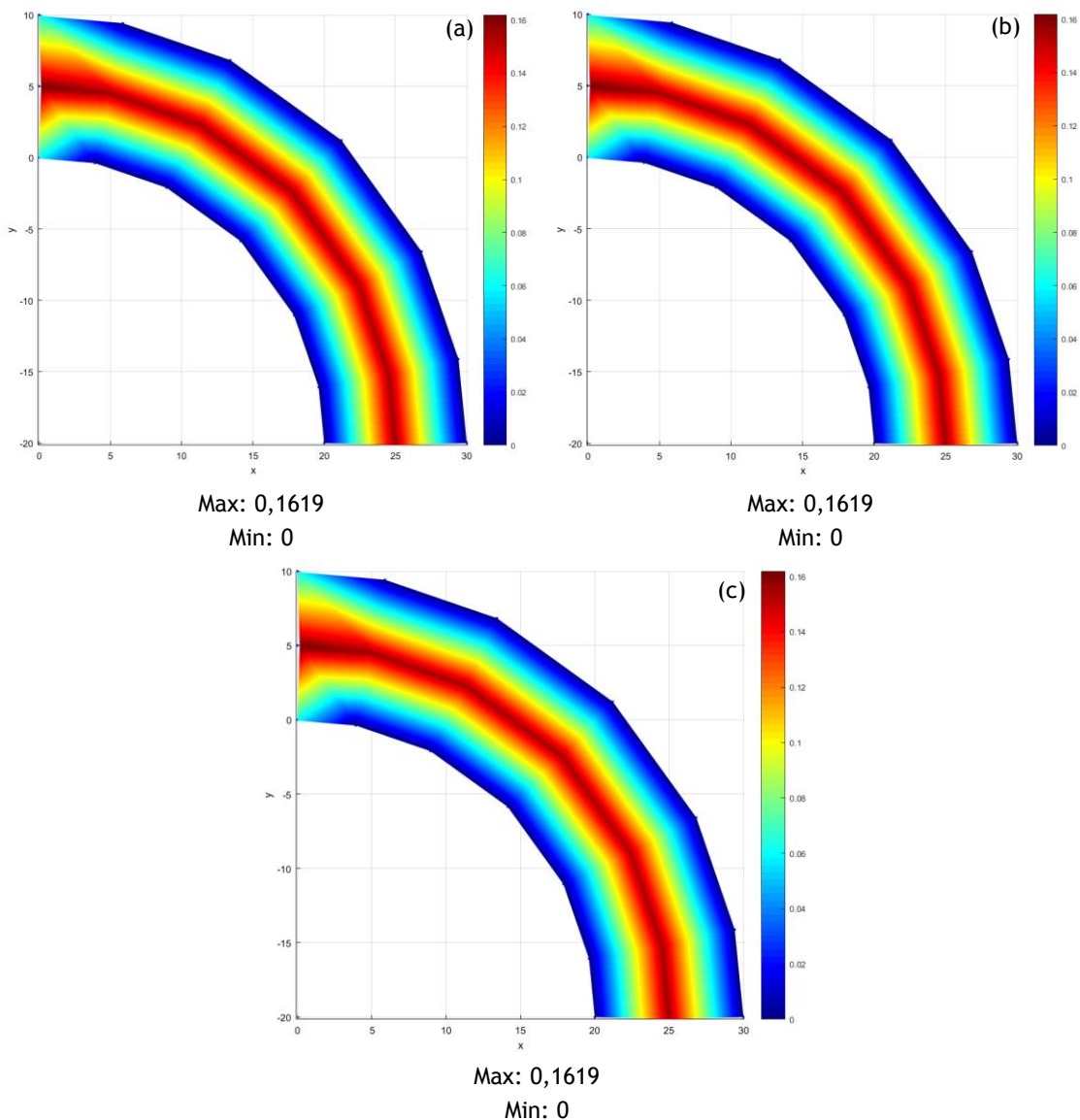


Figure 4.32 - Quarter of a circular crown model (21 nodes) analysed with different methods
a. FEM (triangular elements with 3 nodes) b. NNRPIM c. RPIM

In

Figure 4.33 is presented the analysis with 65 nodes. The NNRPIM and RRPIM were adjusted in this analysis to have consistent results. In NNRPIM, the parameter c is 1,42 and parameter p is 1,03. In RPIM the number of nodes inside the influence domain is 27, the parameter c is 0,0001 and the polynomial basis is quadratic.

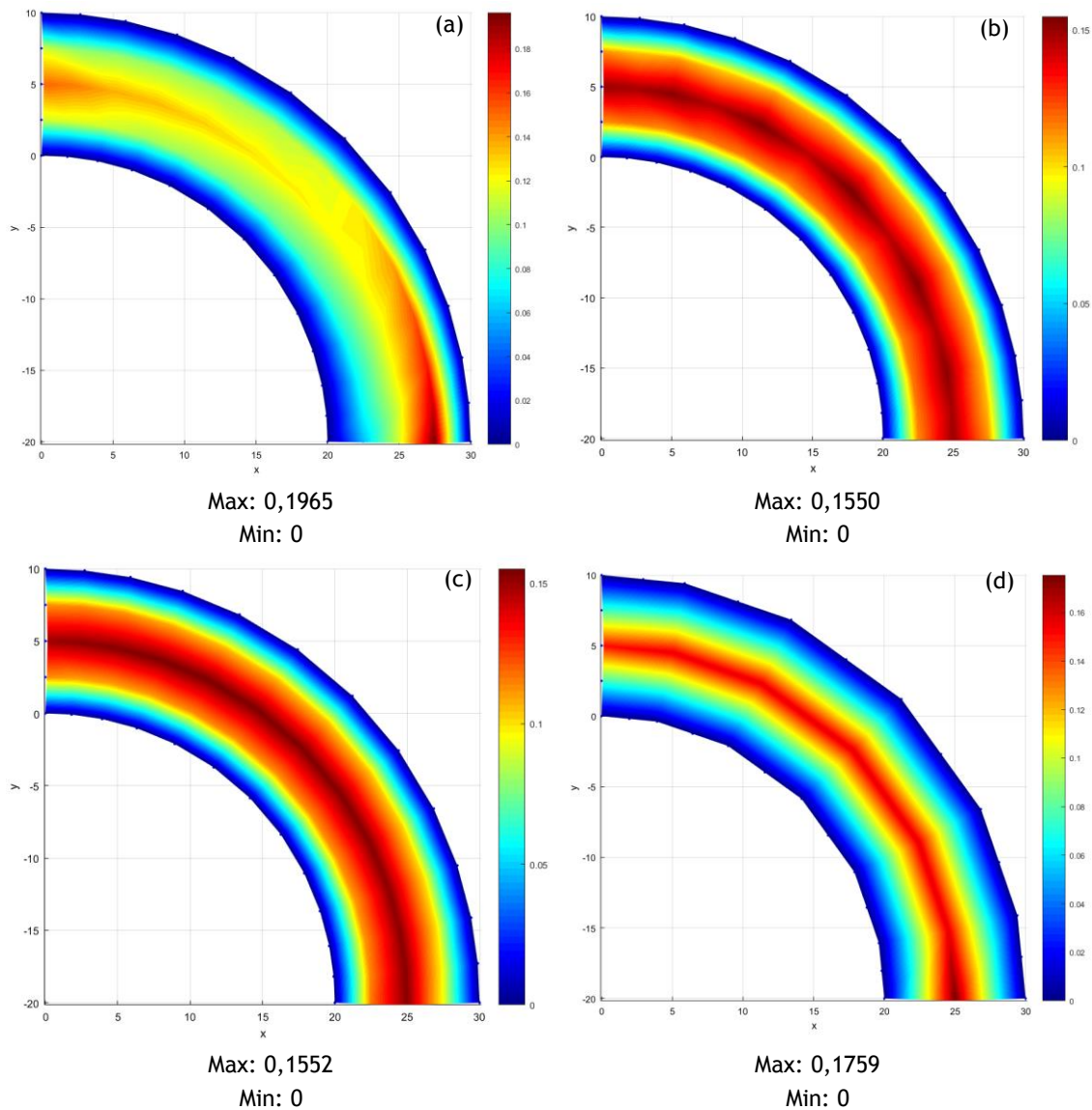


Figure 4.33 - Quarter of a circular crown model (65 nodes) analysed with different methods
a. FEM (triangular elements with 3 nodes) b. NNRPIM c. RPIM d. FEM (triangular elements with 6 nodes)

In Figure 4.34 is presented the analysis with 255 nodes. The RPIM parameters were adjusted to: number of nodes inside the influence domain is 27, the parameter c is 0,0001 and the polynomial is quadratic.

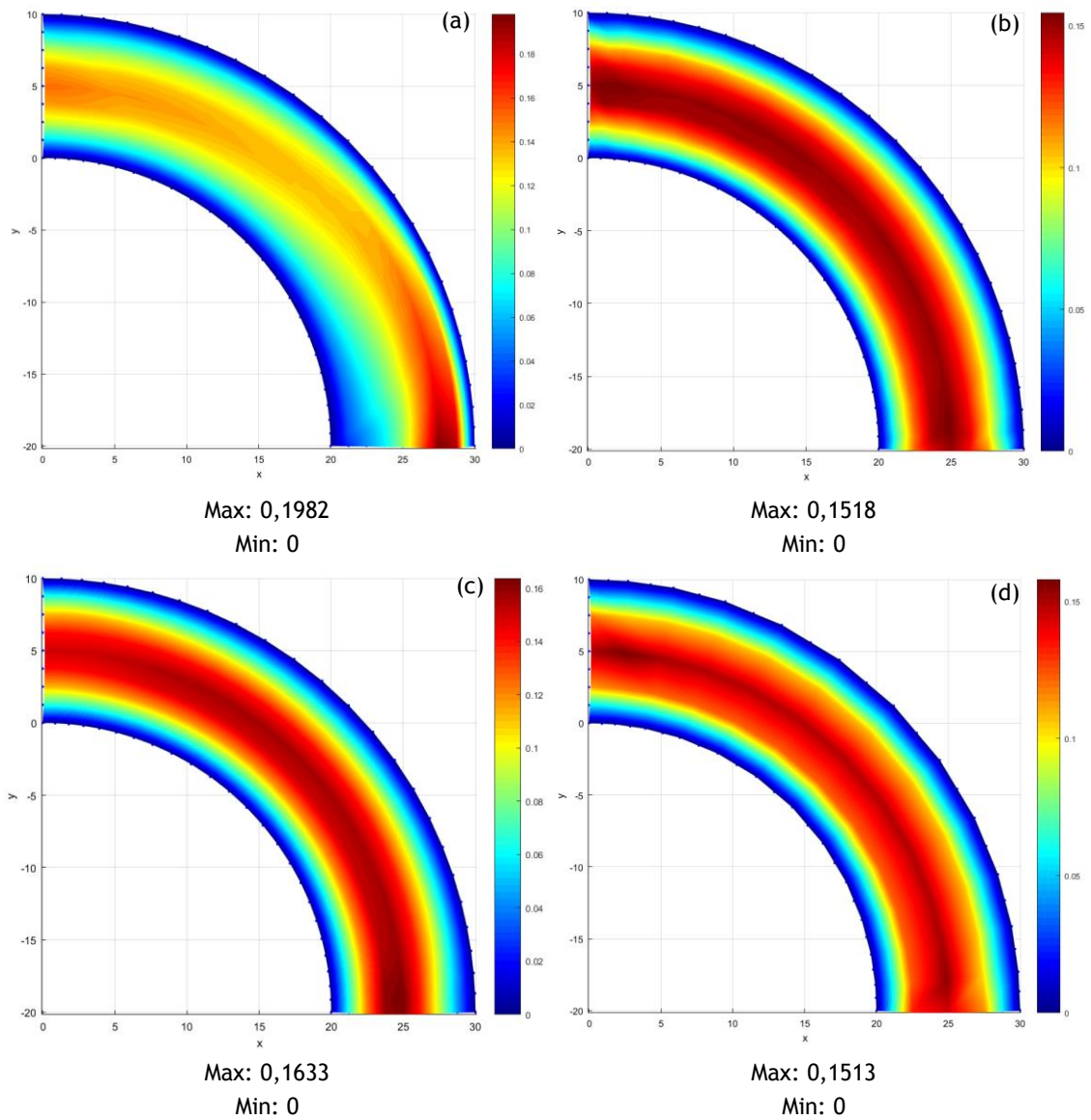


Figure 4.34 - Quarter of a circular crown model (255 nodes) analysed with different methods
a. FEM (triangular elements with 3 nodes) b. NNRPIM c. RPIM d. FEM (triangular elements with 6 nodes)

In Figure 3.5 is presented the analysis with 833 nodes. The RPIM parameters were adjusted to: number of nodes inside the influence domain is 27, the parameter c is 0,0001 and the polynomial is quadratic.

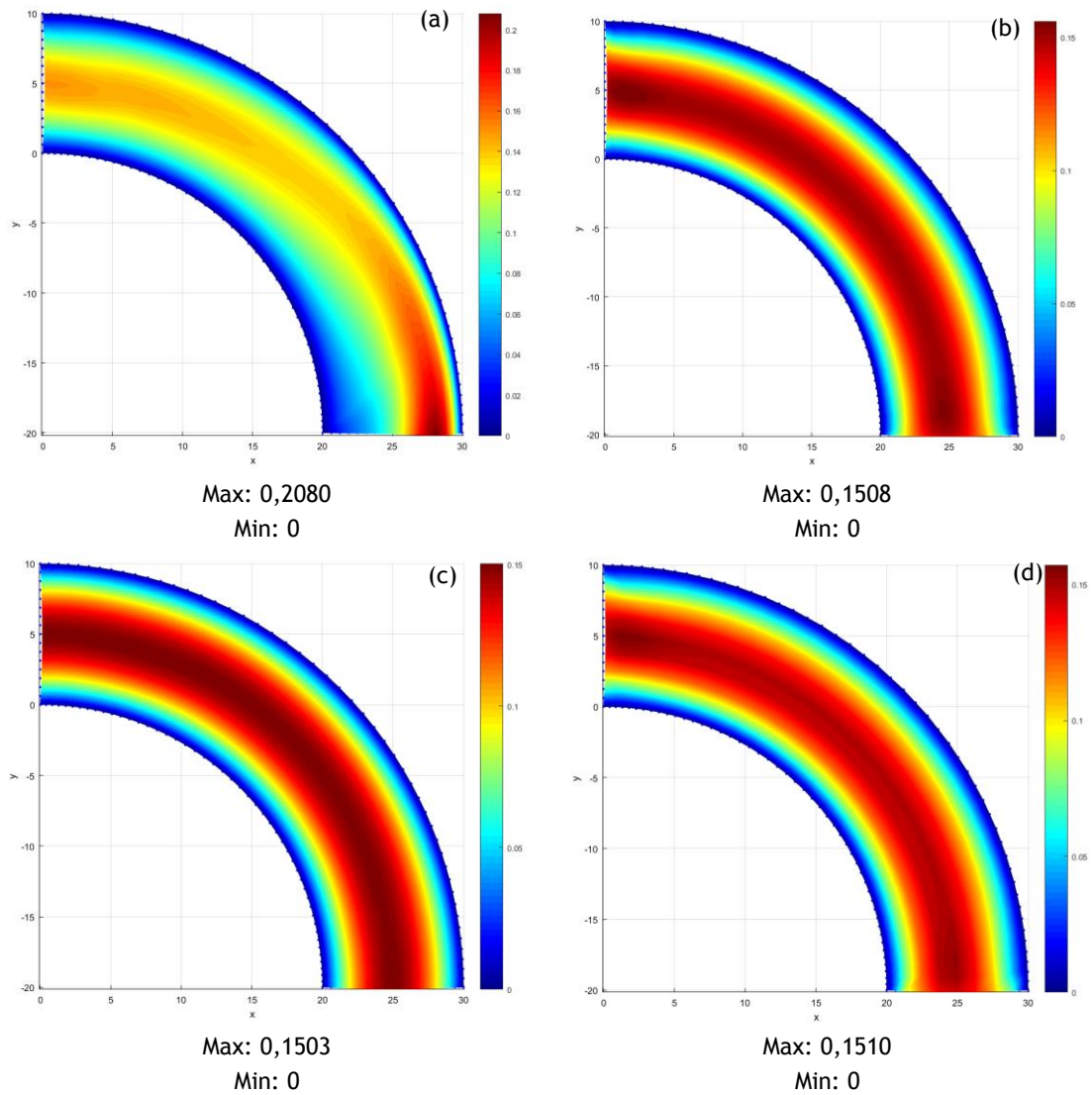


Figure 4.35 - Quarter of a circular crown model (833 nodes) analysed with different methods
 a. FEM (triangular elements with 3 nodes) b. NNRPIM c. RPIM d. FEM (triangular elements with 6 nodes)

In

Figure 4.36 is presented the FEM with a 6 nodes element analysis with 3201 nodes.

The Figure 4.37 represents the discharge along the model.

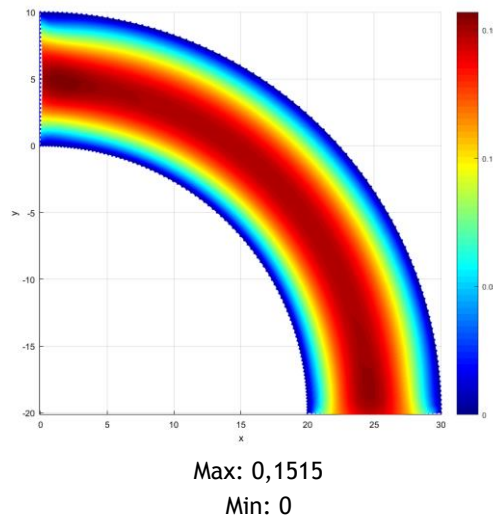


Figure 4.36 - Quarter of a circular crown model (3201 nodes) analysed with FEM (triangular elements with 6 nodes)

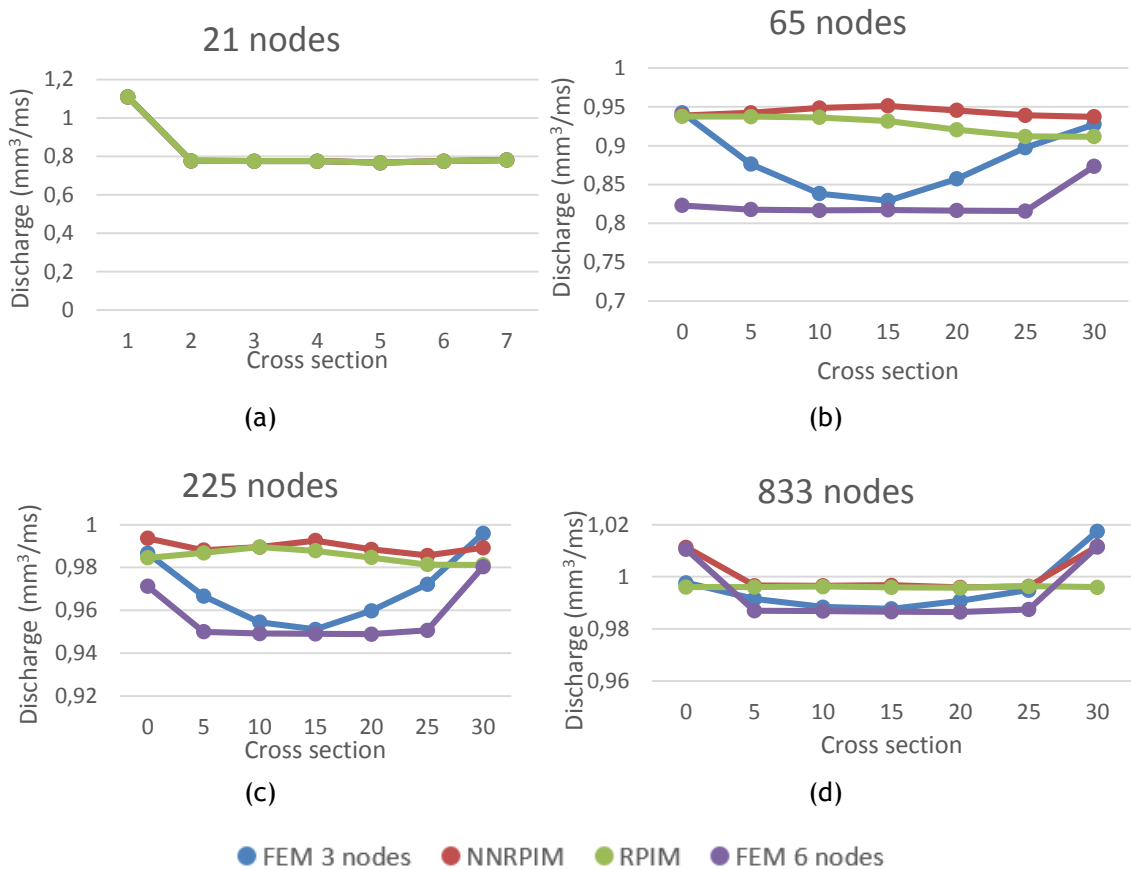


Figure 4.37 - Discharge in every cross section of the models

a. 21 nodes b. 65 nodes c. 225 nodes d. 833 nodes

Analysing the previous charts, it is possible to observe that NNRPIM and RPIM are the most stable numerical methods, with RPIM performing slightly better. They also are the ones that converge more quickly to the value expected: $Q=1 \text{ mm}^3/\text{ms}$.

In Figure 4.39 is presented the discharge for each method and each discretization level.

The cross sections are at the divisions of the first discretization level, so all models can be compared. The first cross section is at $x=0$ and the others are numerated successively.

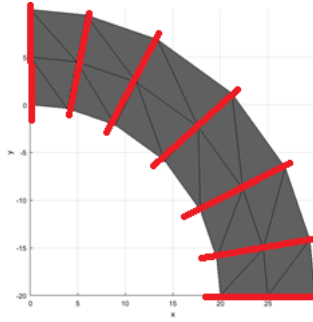
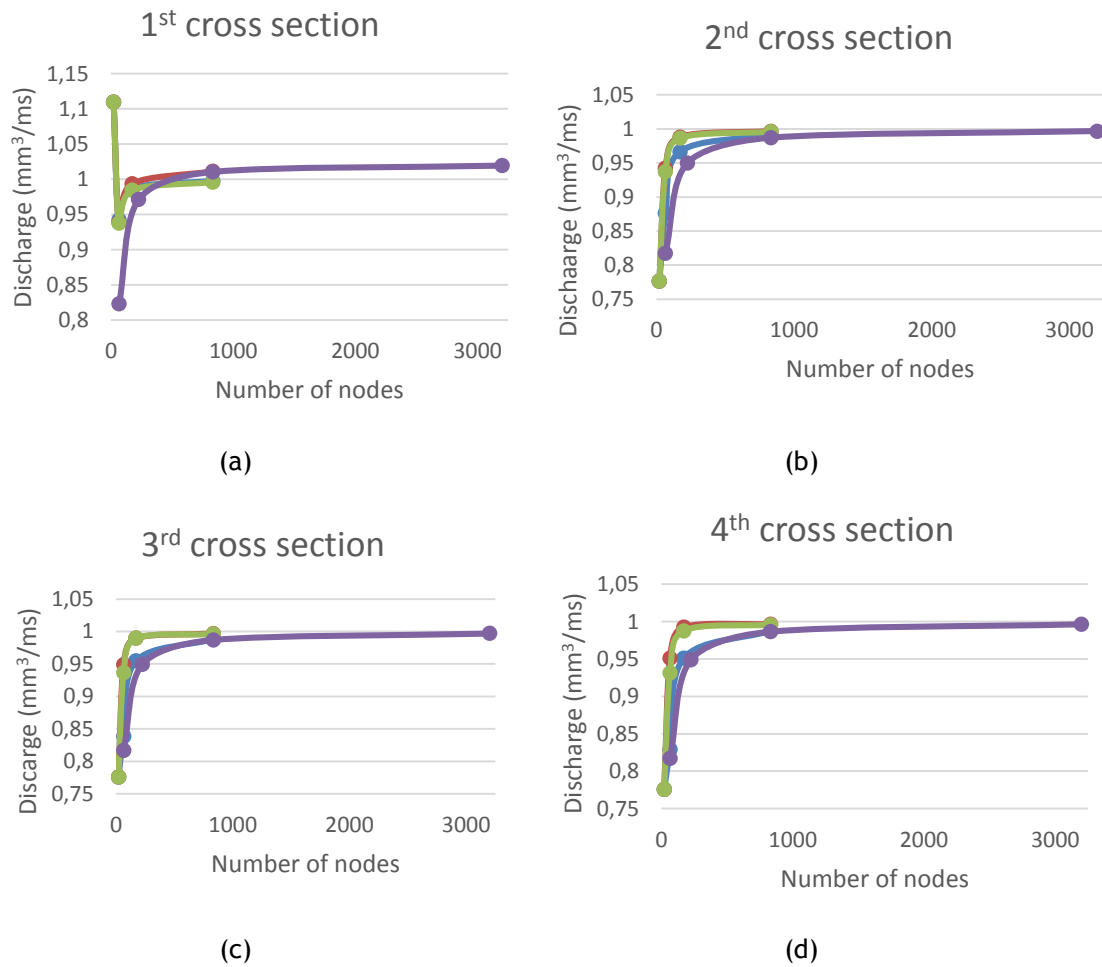


Figure 4.38 - Cross sections



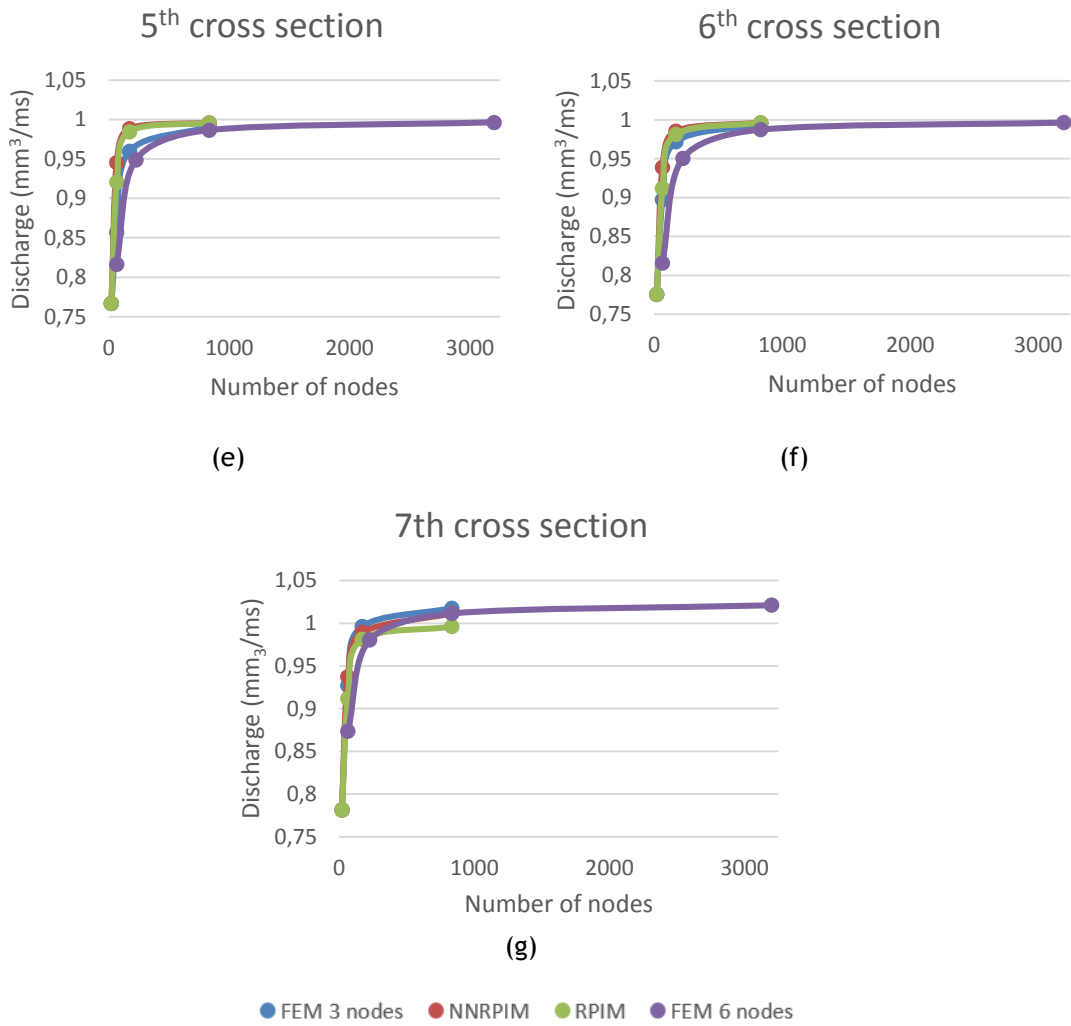


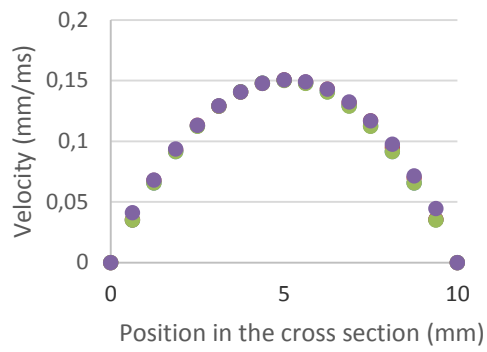
Figure 4.39 - Discharge in each cross session with different methodologies

- a. 1st cross section b. 2nd cross section c. 3rd cross section d. 4th cross section e. 5th cross section f. 6th cross section g. 7th cross section

From this chart analysis, it is possible to verify that NNRPIM and RPIM converge faster than FEM with 3 nodes element and FEM with 6 nodes elements.

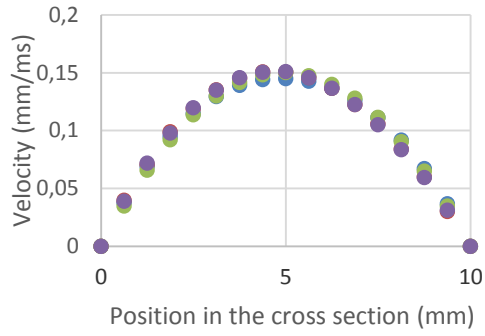
The Figure 4.40 presents the velocity profiles with 833 nodes, which was the level of discretization with the discharge closer to the theoretical.

1st cross section



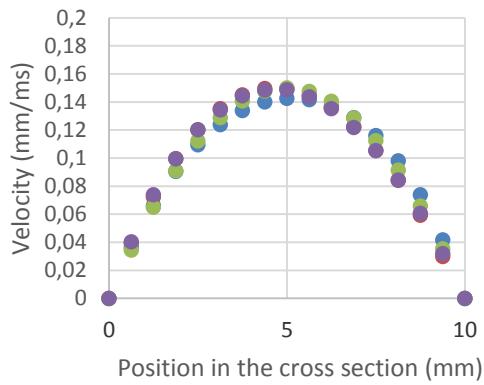
(a)

2nd cross section



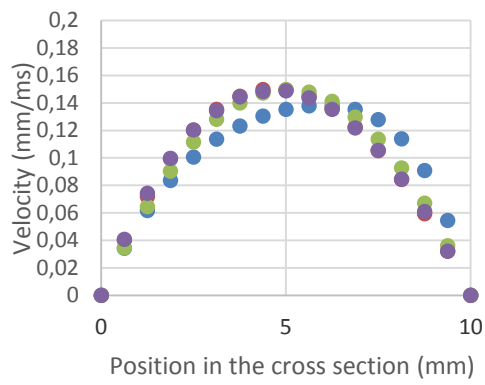
(b)

3rd cross section



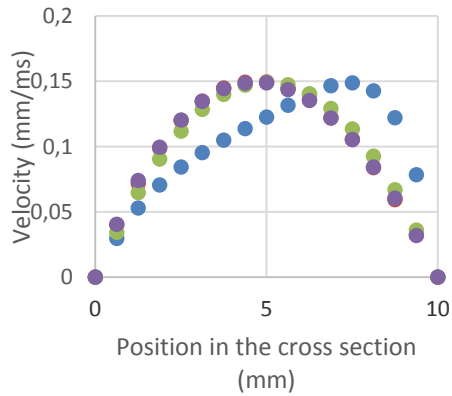
(c)

4th cross section



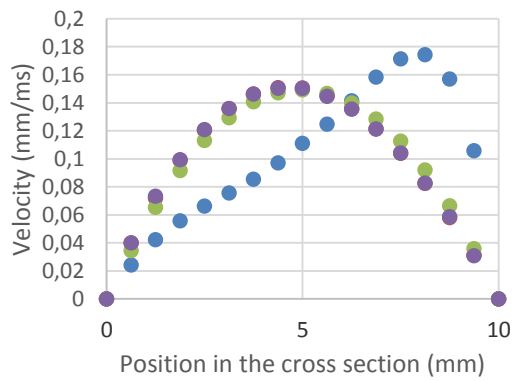
(d)

5th cross section



(e)

6th cross section



(f)

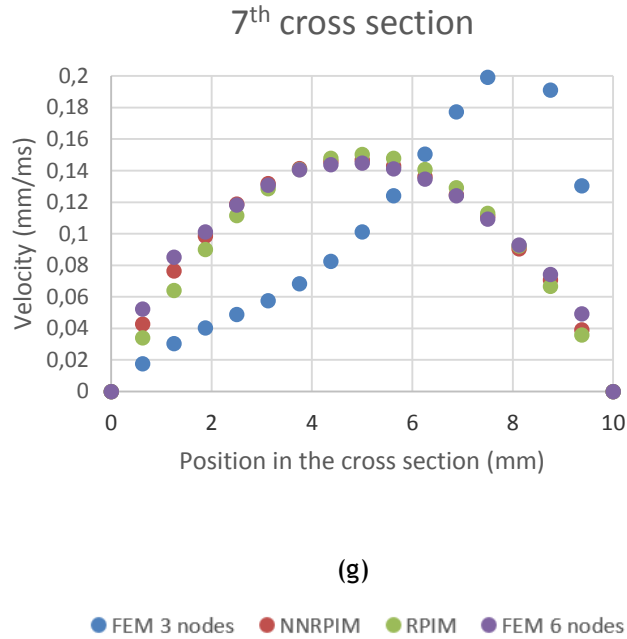


Figure 4.40 - Velocity profiles in each cross session with different methodologies

- a. 1st cross section b. 2nd cross section c. 3rd cross section d. 4th cross section e. 5th cross section
 section f. 6th cross section g. 7th cross section

As it's possible to see in Figure 4.40, the FEM with 6 nodes, the NRRPIM and RPIM have similar velocity profile, but FEM with 3 nodes is significantly different. However, theoretically, in a pipe the flow is distorted as shown in figure. This suggest that the flow pattern given by FEM with a 3-node element is more accurate.

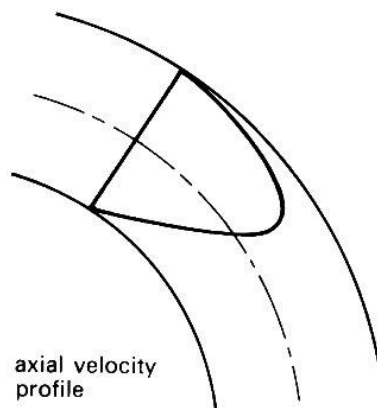


Figure 4.41 - Distortion of the axial velocity profile as a result of tube curvature [47]

4.1.5- Half of a circular crown model

The Figure 4.31 presents the first model. The meshes (a), (b), (c) and (d) with triangular elements with 3 nodes have, respectively, 75, 125, 441 and 1649 elements. The same meshes with triangular elements (except (d)) with 6 nodes have, respectively, 245, 441 and 1649 nodes.

The model has an inner radius of 20 mm and an outer radius of 30mm. Following equation 7.3, the initial velocity profile is:

$$u(r) = 0.06(r)^2 - 0.006r \quad (4.14)$$

and therefore, the theoretical discharge should be:

$$\int_0^{10} (0.06x - 0.006x^2) dx = 1 \quad (4.15)$$

The Figure 4.31 shows the different levels of discretization studied.

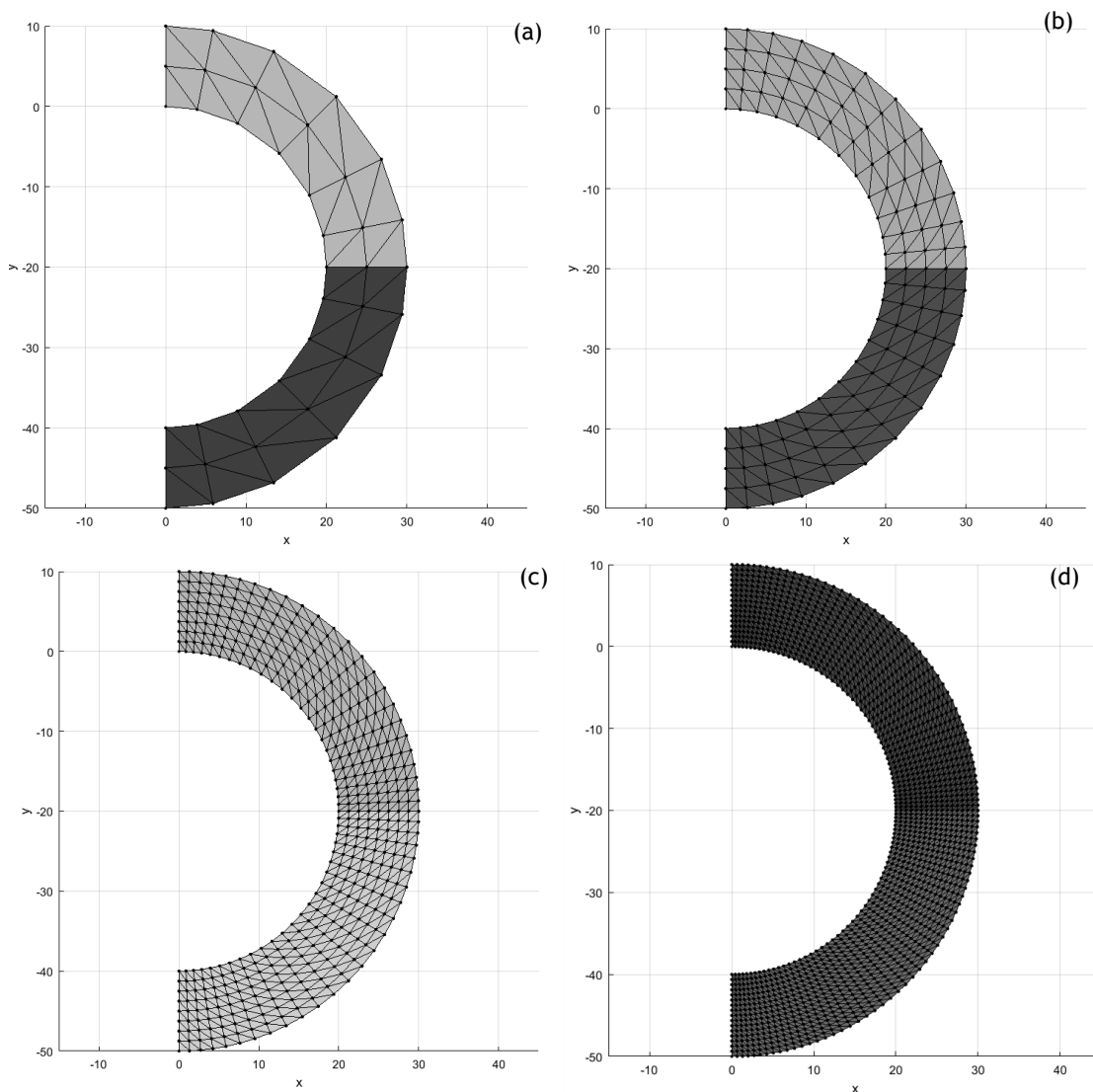


Figure 4.42- Half of a circular crown model with different meshes
a. 48 elements b. 192 elements c. 768 elements d. 3072 elements

4.1.5.1 - Results

The results of the analysis with the different numerical methods are represented in Figure 4.43, Figure 4.44, Figure 4.45 and Figure 4.46.

In

Figure 4.43 is presented the analysis with 75 nodes. In this example, NNRPIM the parameters were changed. The parameter c is 1,42 and the parameter p is 1,03.

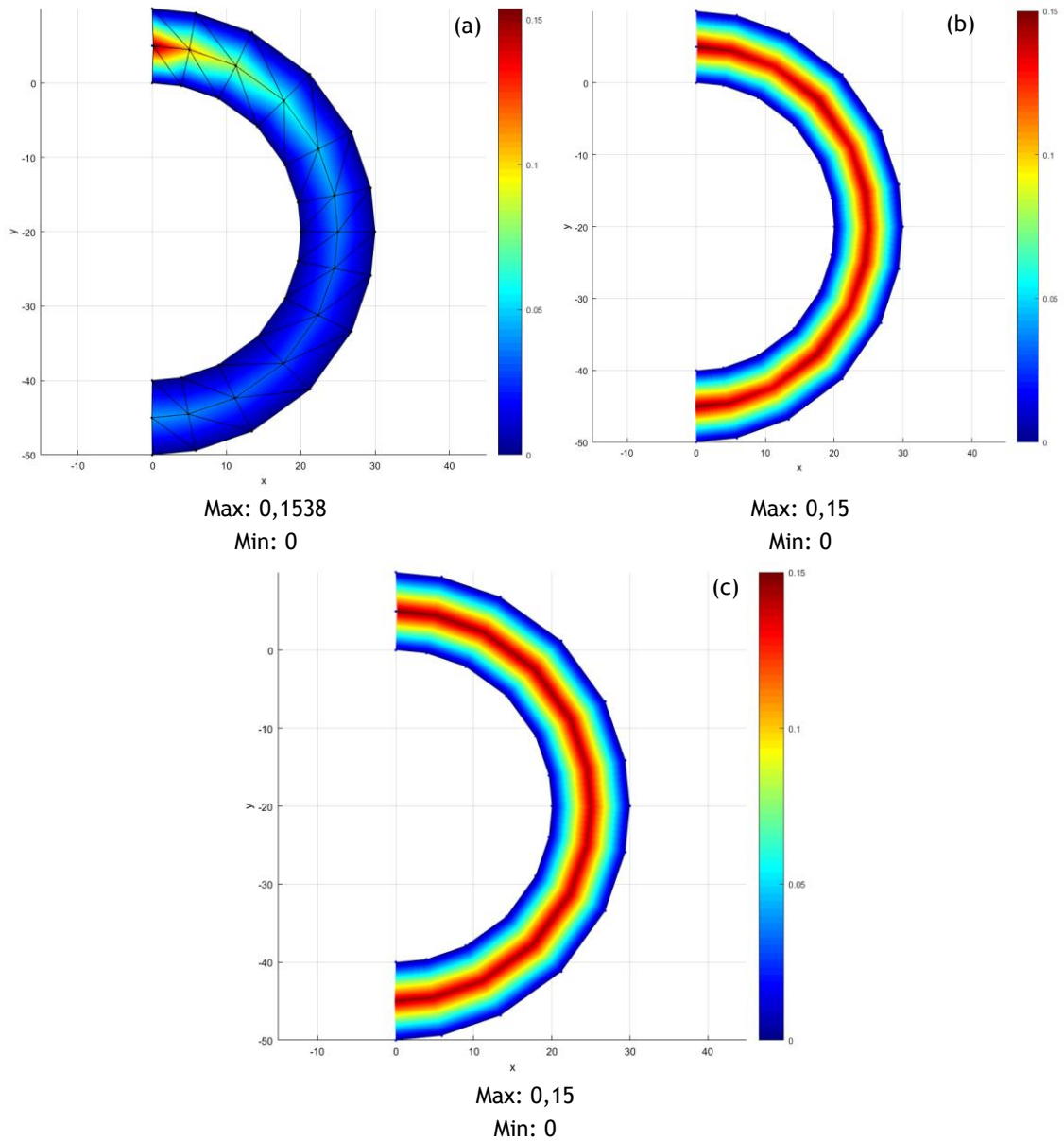


Figure 4.43 - Half of a circular crown model (75 nodes) analysed with different methods
 a. FEM (triangular elements with 3 nodes) b. NNRPIM c. RPIM

With this level of discretization, the FEM with 3 nodes is considerable different from the other two examples. This results are not consistent with the reality.

In Figure 4.44 is presented the analysis with 125 nodes. In this example, both NNRPIM and RPIM parameters were changed. In NNRPIM, the c parameter is 1,42 and the parameter p is 1,03. In RPIM, the parameter c is 0,0001 and parameter p is 0,9999, the number of nodes inside the influence domain is 27 and the number of Gauss points is 2.

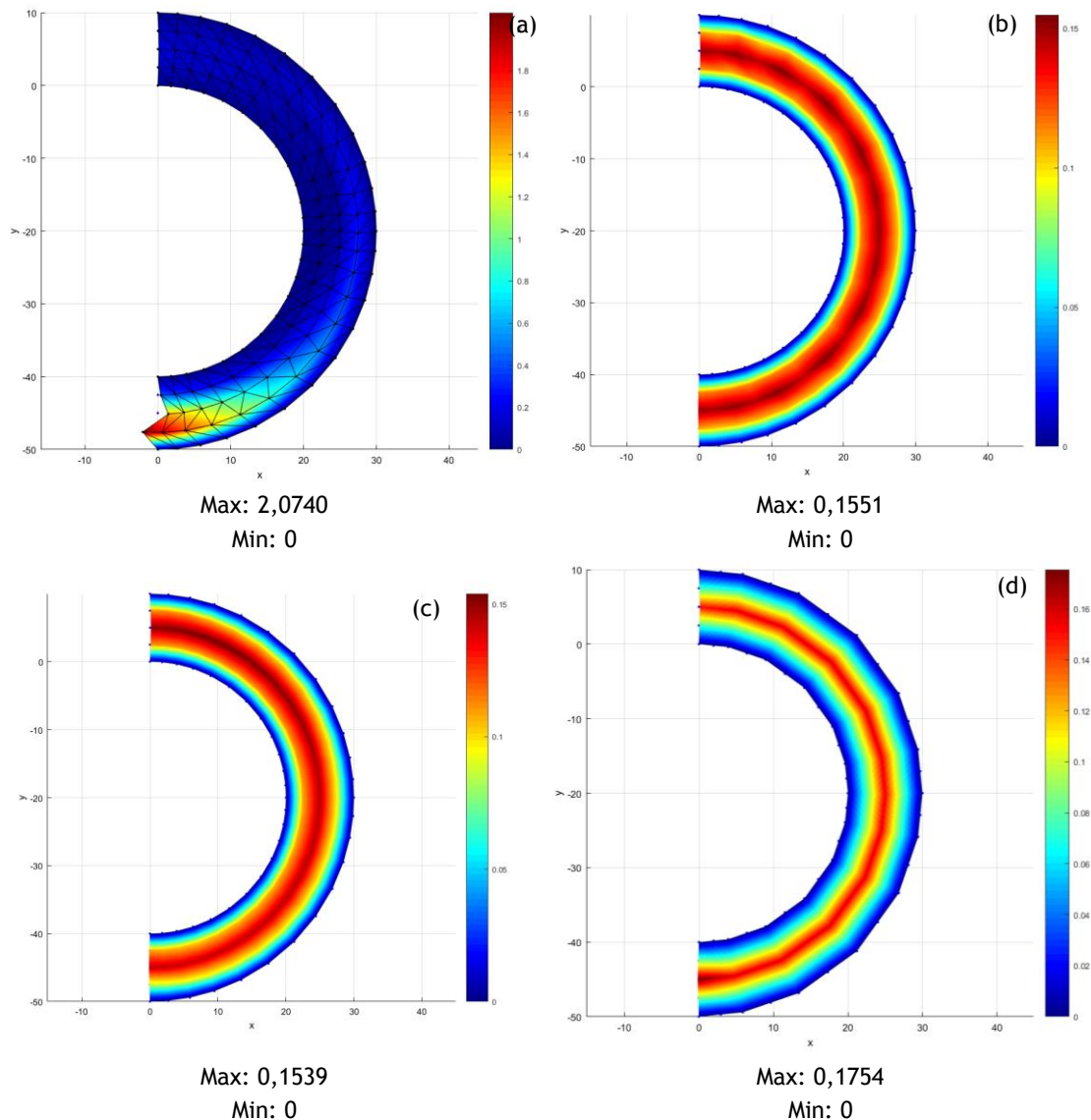


Figure 4.44 - Half of a circular crown model (125 nodes) analysed with different methods
 a. FEM (triangular elements with 3 nodes) b. NNRPIM c. RPIM d. FEM (triangular elements with 6 nodes)

In

Figure 4.45 is presented the analysis with 441 nodes.

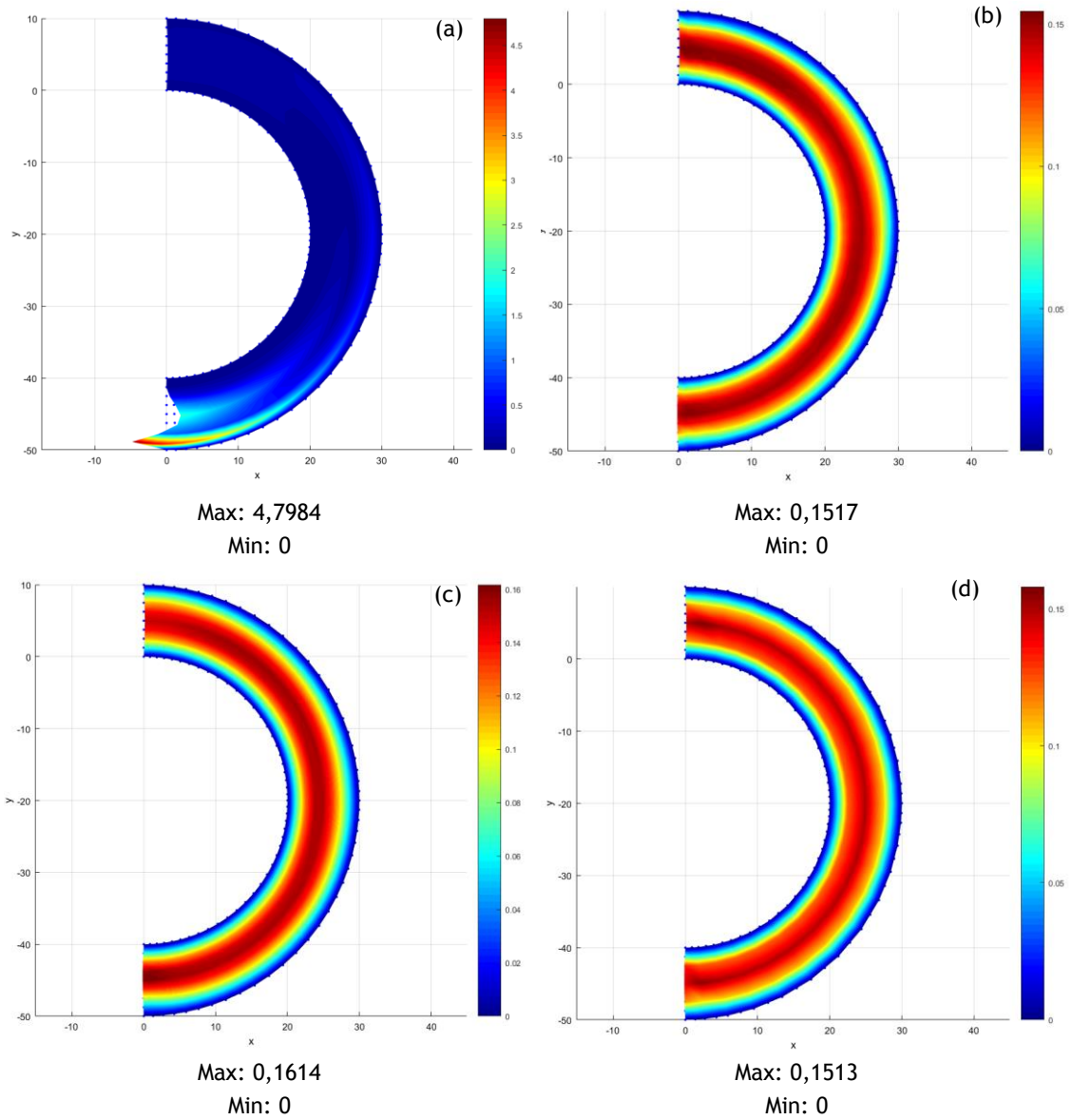


Figure 4.45 - Half of a circular crown model (441 nodes) analysed with different methods
a. FEM (triangular elements with 3 nodes) b. NNRPIM c. RPIM d. FEM (triangular elements with 6 nodes)

In

Figure 4.46 is presented the analysis with 1659 nodes. The RPIM parameters were changed. The parameter c is 0,0001, the parameter c is 0,9999, the number of nodes inside the influence domain is 27 and the number of Gauss points is 2.

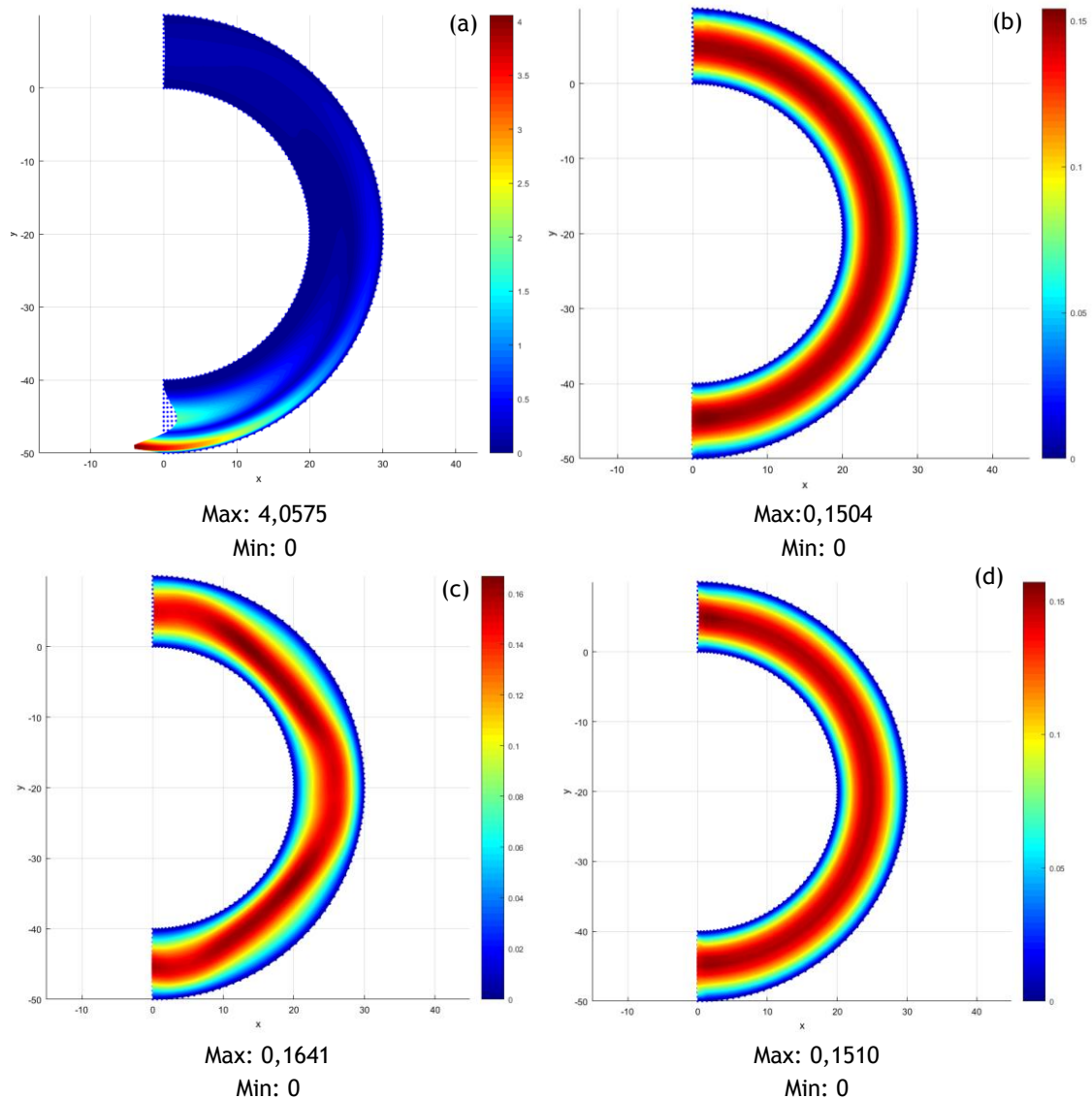


Figure 4.46 - Half of a circular crown model (1659 nodes) analysed with different methods
 a. FEM (triangular elements with 3 nodes) b. NNRPIM c. RPIM d. FEM (triangular elements with 6 nodes)

As a general comment for all the tests, the FEM with triangular elements with 3 nodes does not represent a viable solution to simulate this example.

The FEM with 3 nodes element is not represented in the graphs because the results were very displaced from the other analysis, which doesn't allow the their correct comparison.

The Figure 4.47 represents the discharge along the model.

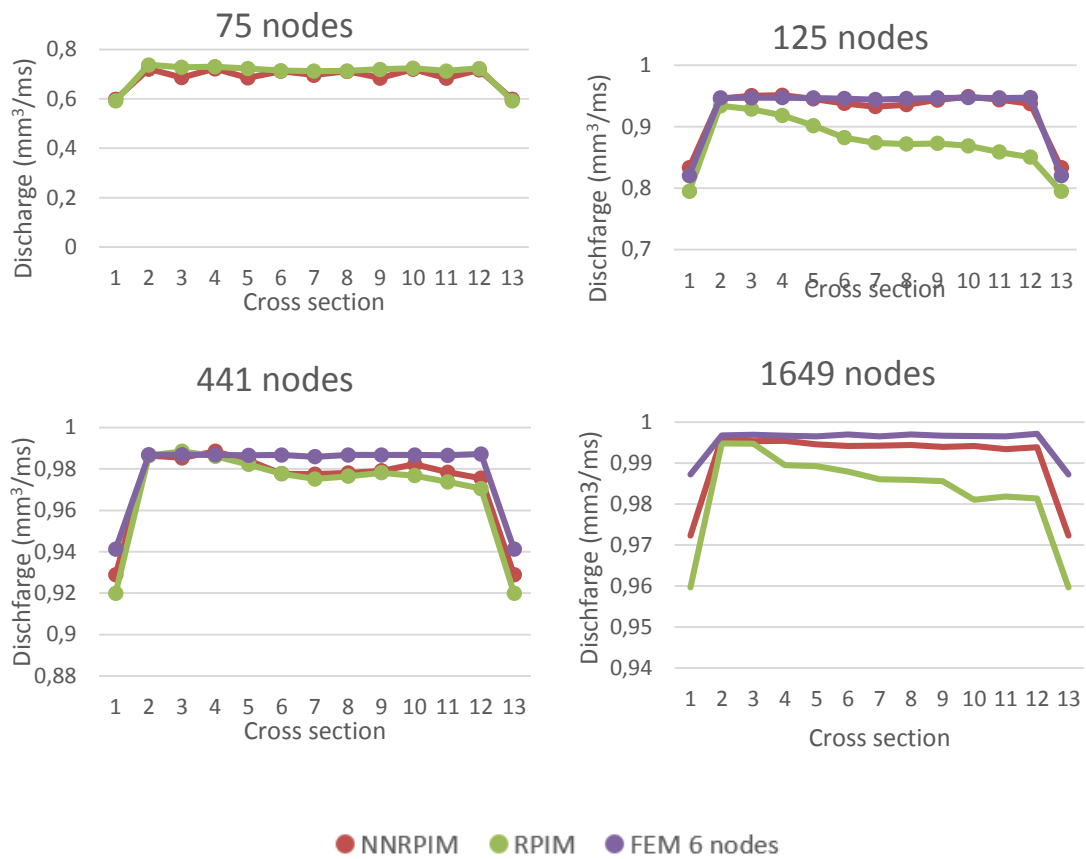


Figure 4.47 - Discharge in every cross section of the models

a. 75 nodes b. 125 nodes c. 441 nodes d. 1649 nodes

The Figure 4.47 shows that FEM with a 6-nodes element and NNRPIM are the most constant analysis, with FEM being slightly better.

To evaluate the discharge along this model, 13 cross sections were analysed. This cross section are represented in the Figure 4.48.

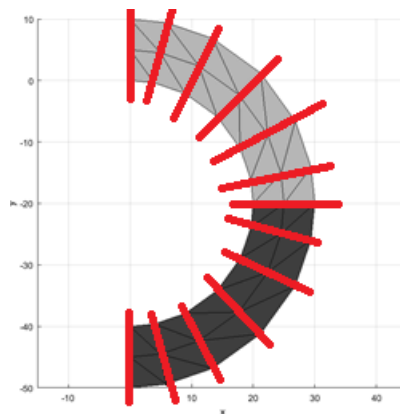
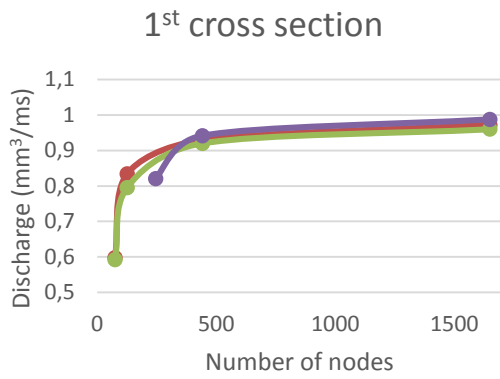
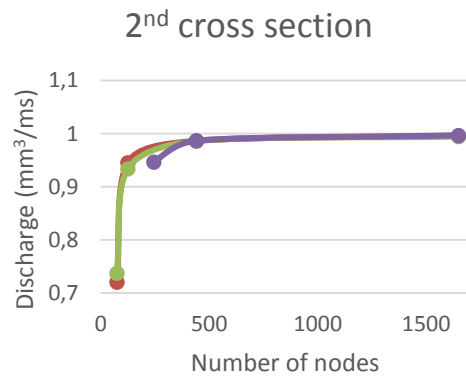


Figure 4.48 - Cross sections in half of a crown model

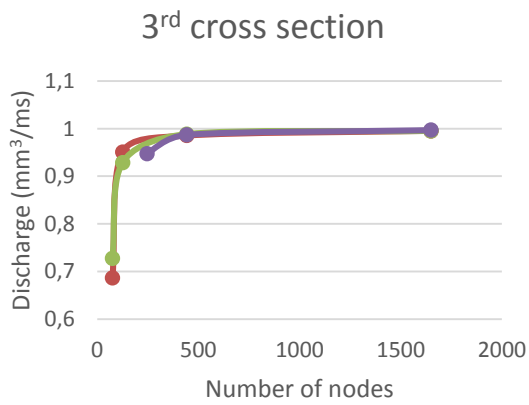
The first cross section is $x=0$ and $0 < y < 10$ and the rest of the cross sections are numerated following the model direction.



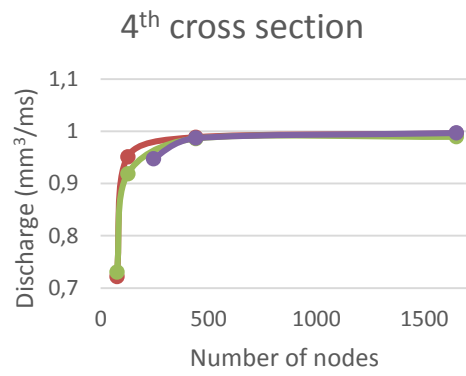
(a)



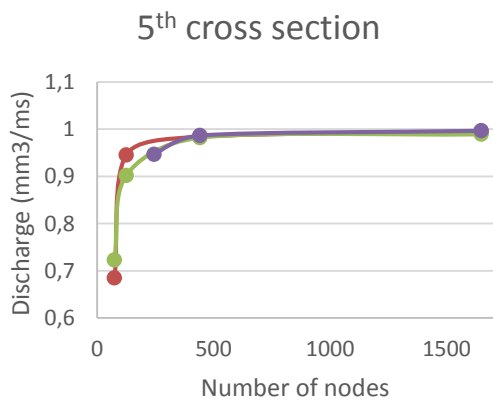
(b)



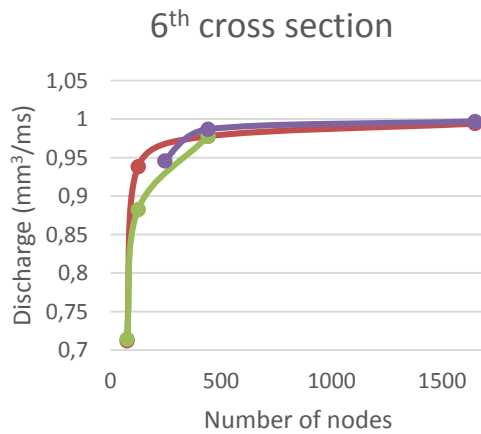
(c)



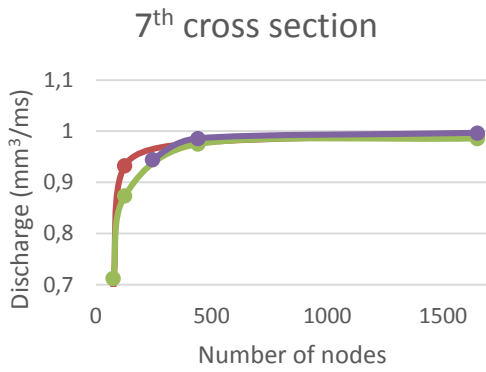
(d)



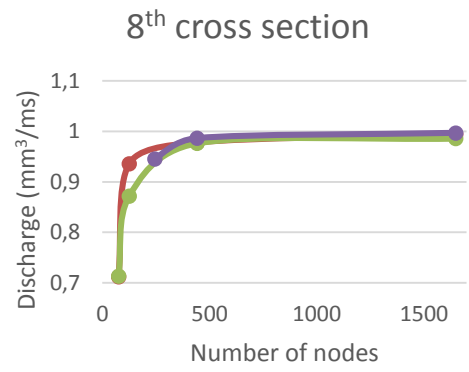
(e)



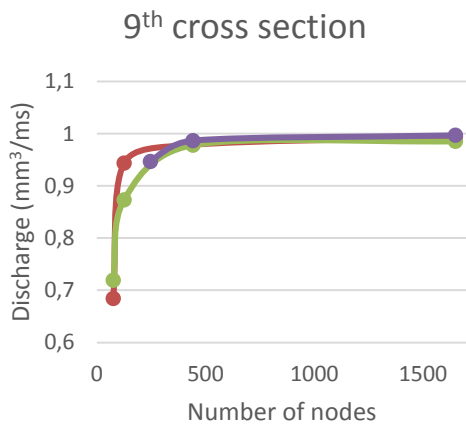
(f)



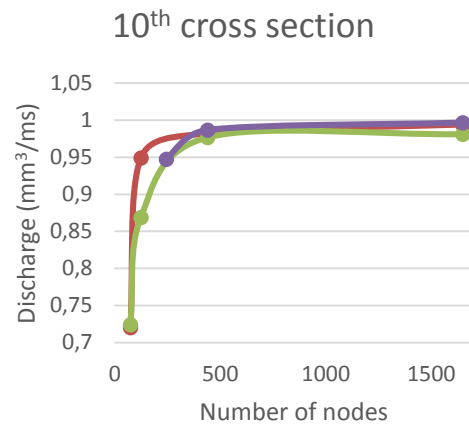
(g)



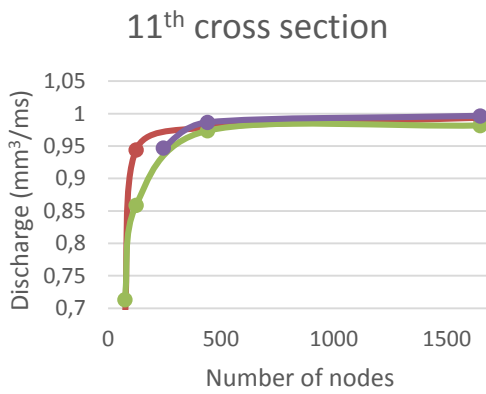
(h)



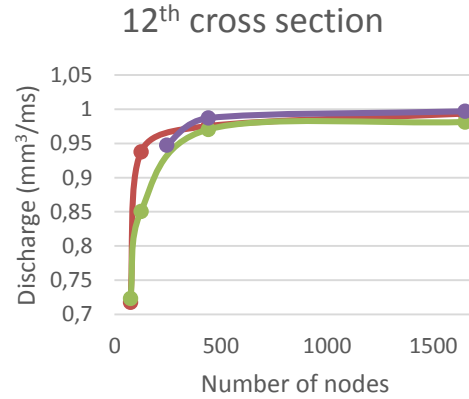
(i)



(j)



(l)



(m)

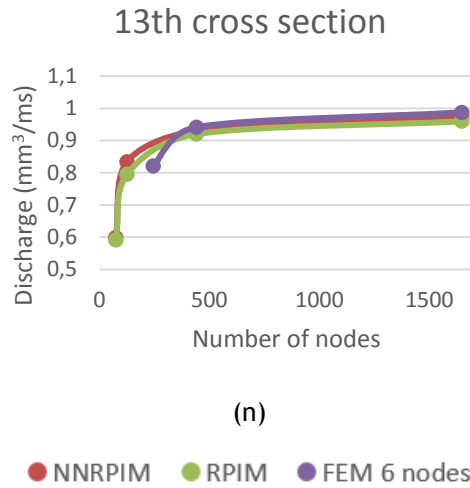
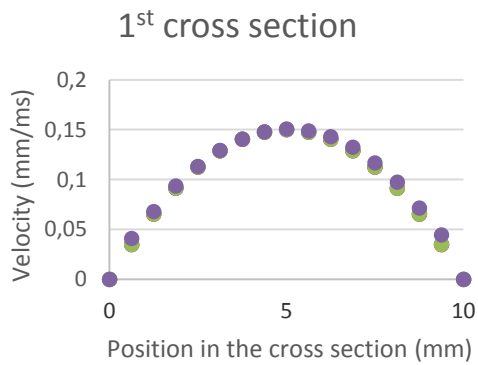


Figure 4.49 - Velocity profiles in each cross session with different methodologies

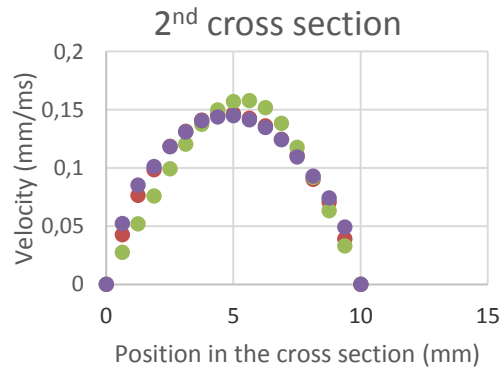
- a. 1st cross section b. 2nd cross section c. 3rd cross section d. 4th cross section e. 5th cross section
 f. 6th cross section g. 7th cross section h. 8th cross section i. 9th cross section j.
 10th cross section l. 11th cross section m. 12th cross section n. 13th cross section

From Figure 4.49, it's possible to verify that RPIM is the method that converges earlier.

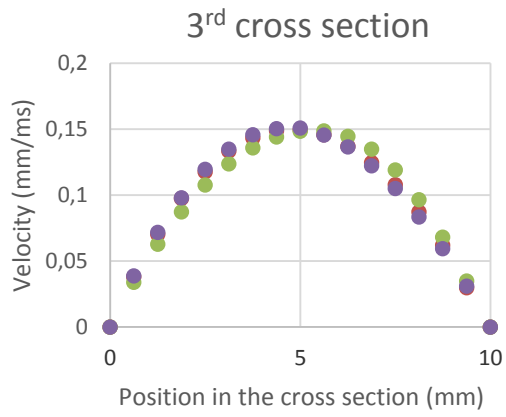
The Figure 4.50 presents the velocity profiles with 833 nodes, which was the level of discretization with the discharge closer to the theoretical.



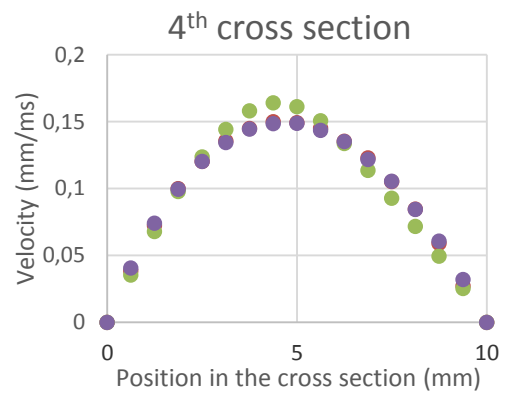
(a)



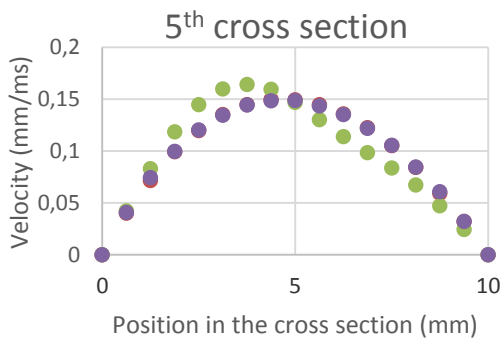
(b)



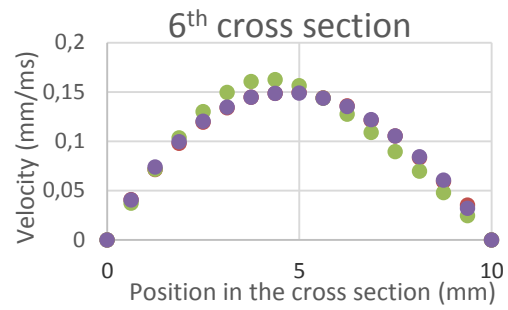
(c)



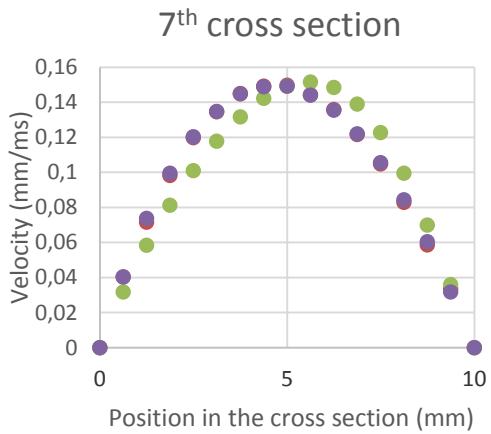
(d)



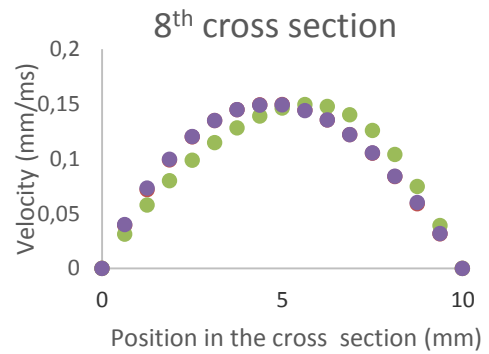
(e)



(f)



(g)



(h)

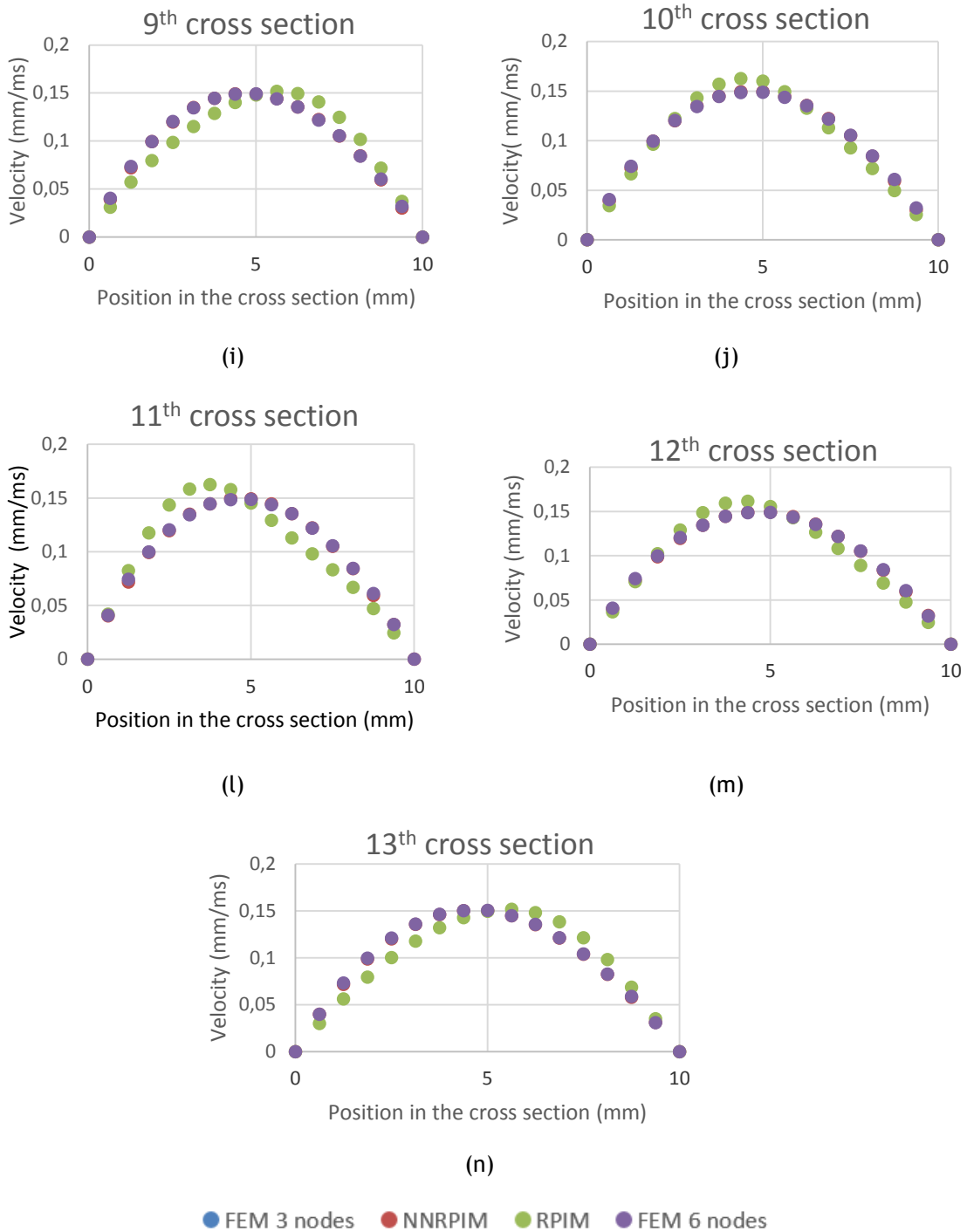


Figure 4.50 - Discharge in each cross session with different methodologies

- a. 1st cross section b. 2nd cross section c. 3rd cross section d. 4th cross section e. 5th cross section f. 6th cross section g. 7th cross section h. 8th cross section i. 9th cross section j. 10th cross section l. 11th cross section m. 12th cross section n. 13th cross section

As mentioned in the last model, the flow of a pipe is different from a linear model. The maximum velocity should be close to the outer wall. None of the analysis show this particularity, and RPIM contradicts this pattern.

4.1.6- Double curve model

The Figure 4.51 presents the first model. The meshes (a), (b), (c) and (d) with triangular elements with 3 nodes have, respectively, 75, 245, 873 and 3281 elements. The same meshes with triangular elements (except (d)) with 6 nodes have, respectively, 245, 873 and 3281 nodes. Following equation 7.3, the initial velocity profile is:

$$u(r) = 0.06(r)^2 - 0.006r \quad (4.16)$$

and therefore, the theoretical discharge should be:

$$\int_0^{10} (0.06x - 0.006x^2) dx = 1 \quad (4.17)$$

The Figure 4.31 shows the different levels of discretization studied.

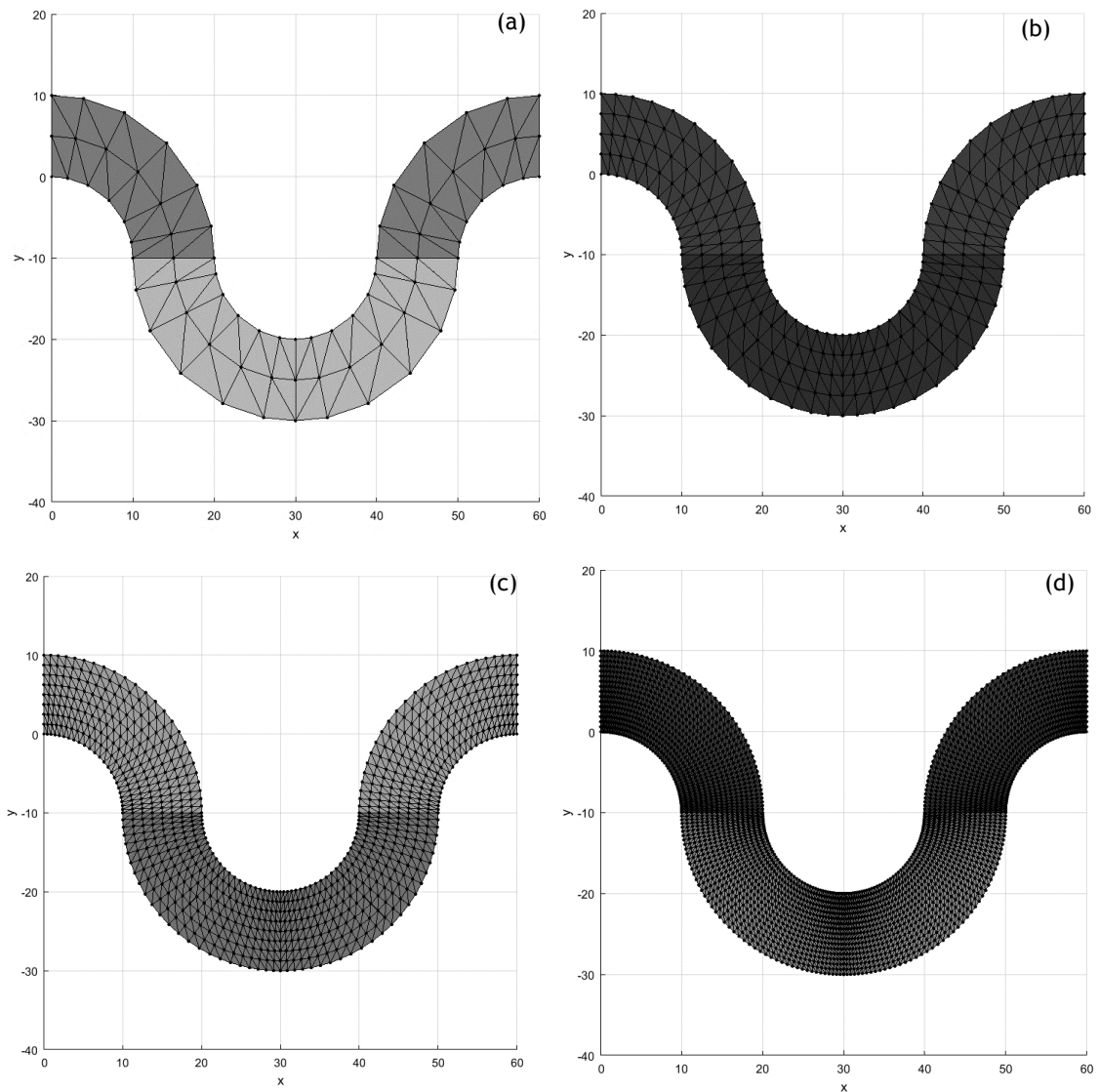


Figure 4.51 Double curve model with different meshes
a. 96 elements b. 4384 elements c. 1536 elements d. 6144 elements

4.1.6.1 - Results

The results of the analysis with the different numerical methods are represented in Figure 4.52,

Figure 4.53, Figure 4.54 and

Figure 4.55. The Figure 4.52 represents the analysis with 75 nodes.

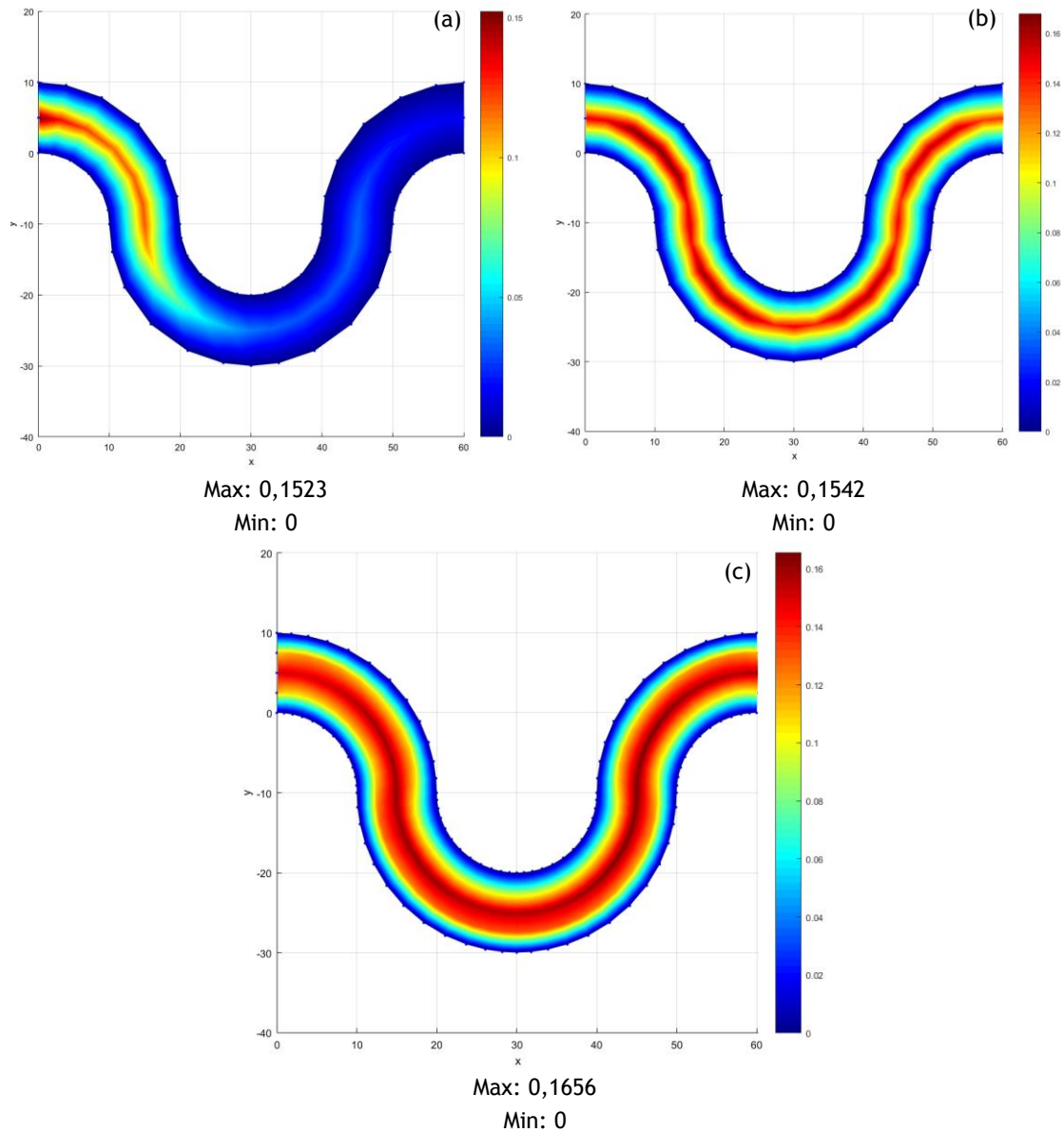


Figure 4.52 - Double curve model (75 nodes) analysed with different methods
a. FEM (triangular elements with 3 nodes) b. NNRPIM c. RPIM

In this analysis, the FEM with a 3 nodes element have a clear atypical result.
The

Figure 4.53 represents the analysis with 225 nodes.

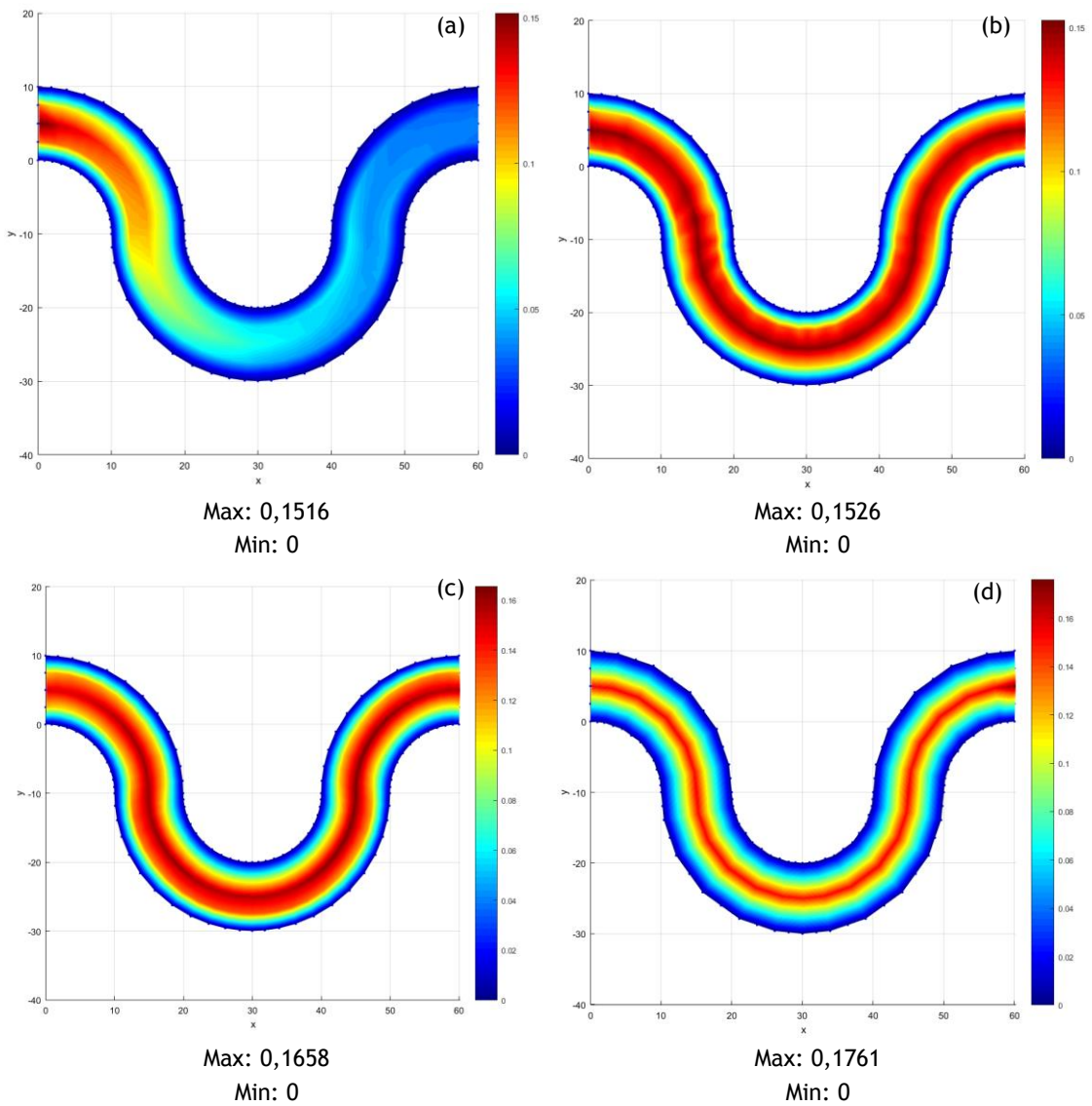


Figure 4.53 - Double curve model (245 nodes) analysed with different methods
 a. FEM (triangular elements with 3 nodes) b. NNRPIM c. RPIM d. FEM (triangular elements with 6 nodes)

The Figure 4.54 represents the analysis with 873 nodes. The NNRPIM parameters had to be changed. The parameter c is 1,42 and the parameter p is 1,03.

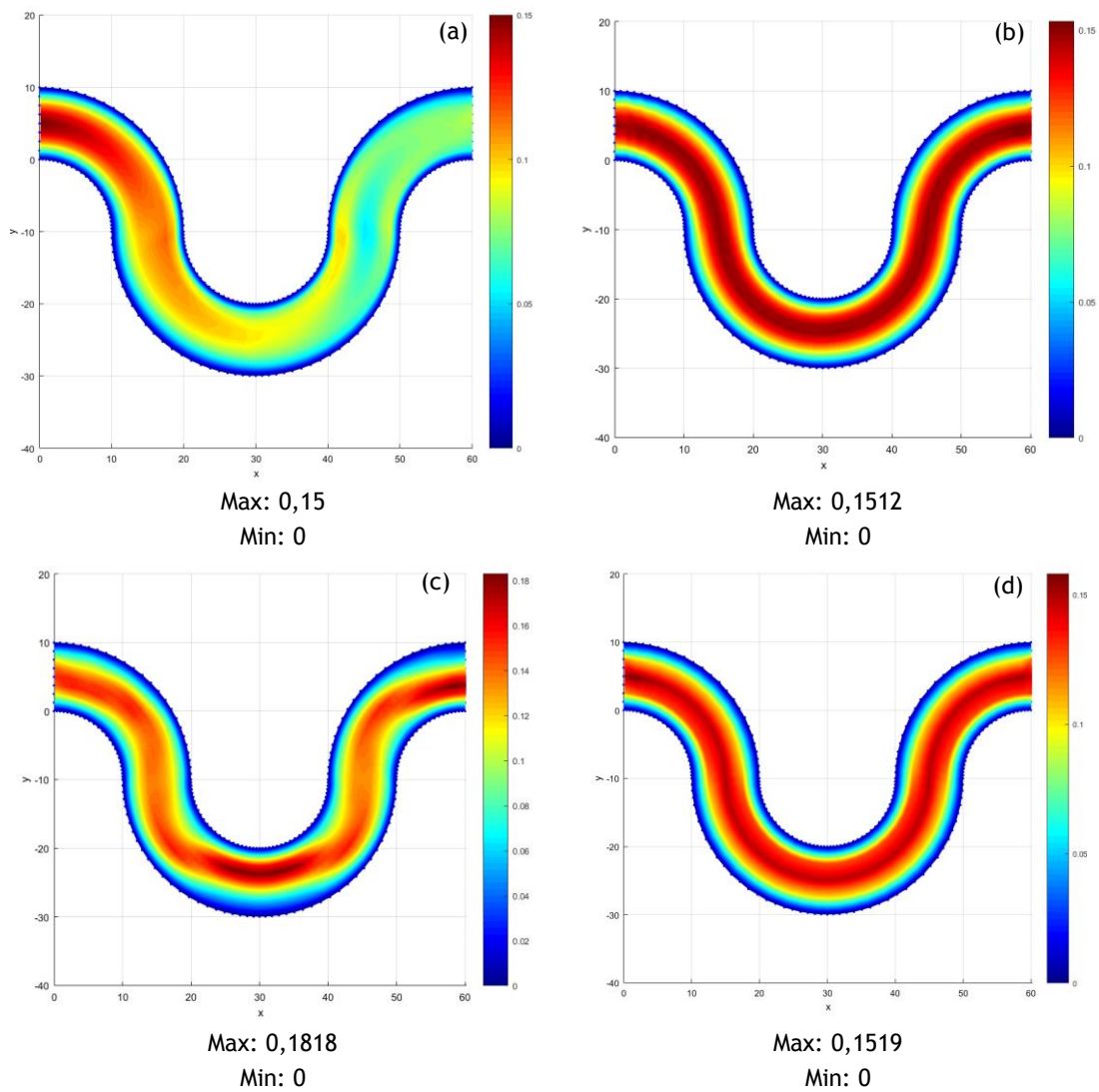


Figure 4.54 - Double curve model (873 nodes) analysed with different methods
 a. FEM (triangular elements with 3 nodes) b. NNRPIM c. RPIM d. FEM (triangular elements with 6 nodes)

The Figure 4.55 represents the analysis with 3281 nodes.

The FEM with a 3 nodes element has poor performance, regardless the levels of the discretization. RPIM also presents a low performance on the last two levels of discretization.

The Figure 4.57 represents the discharge along the model. The cross sections are represented in the Figure 4.56.

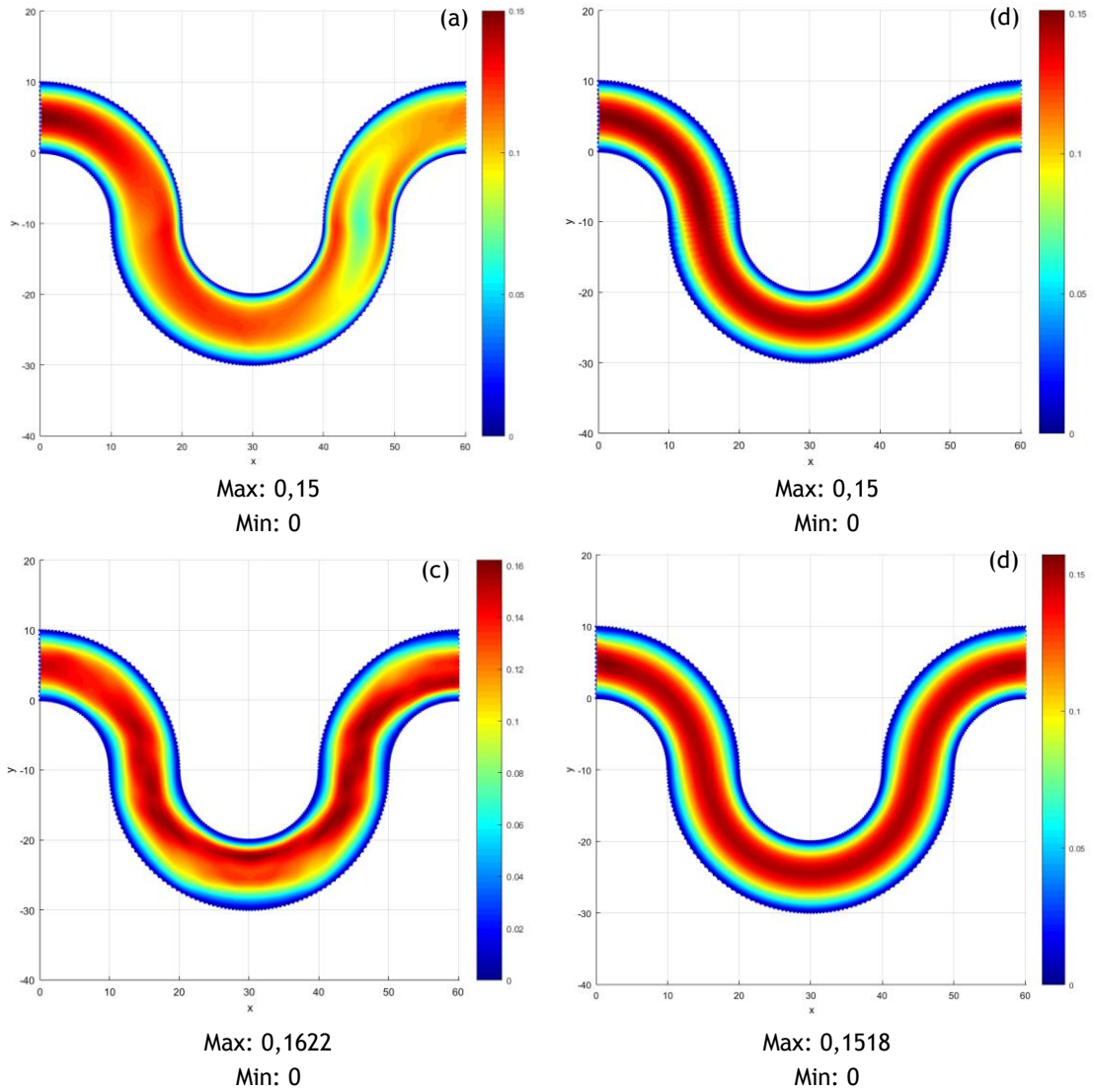


Figure 4.55 - Double curve model (3281 nodes) analysed with different methods
 a. FEM (triangular elements with 3 nodes) b. NNRPIM c. RPIM d. FEM (triangular elements with 6 nodes)

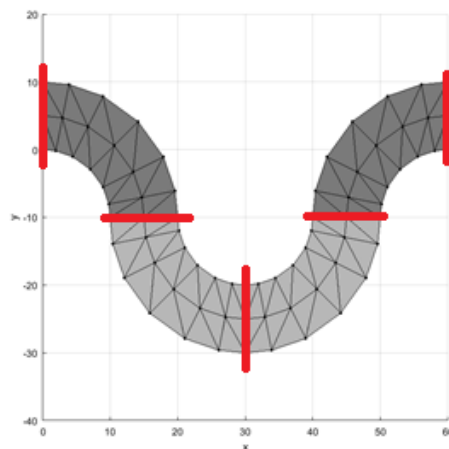


Figure 4.56 - Cross sections in the double curve model

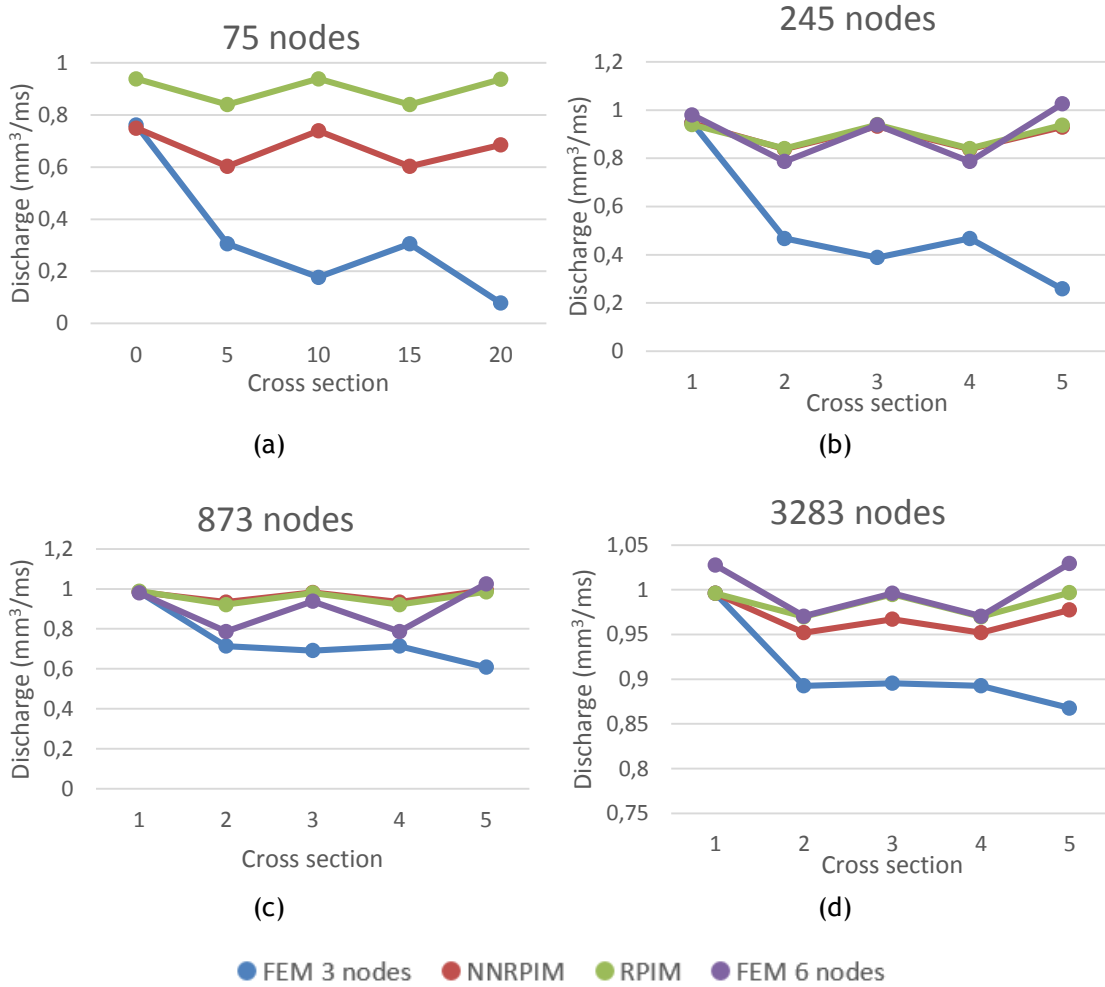
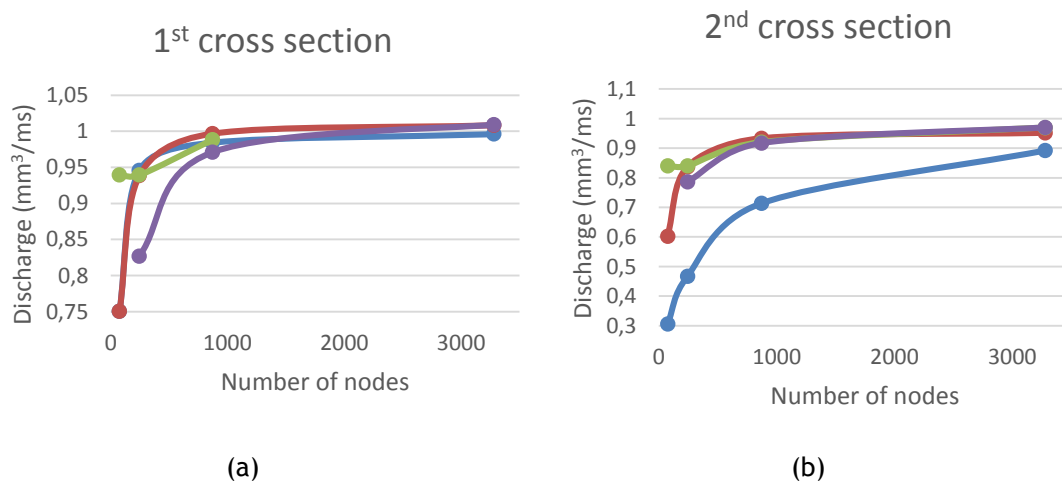


Figure 4.57 - Discharge in every cross section of the models
a. 75 nodes b. 245 nodes c. 873 nodes d. 3283 nodes

The best performing numerical methods, maintaining the discharge along the model, are the FEM with 6 elements and the RPIM. Although it is possible to observe that NRRPIM and RPIM converge faster.

The Figure 4.58 represents the discharge in each level of discretization of each method.



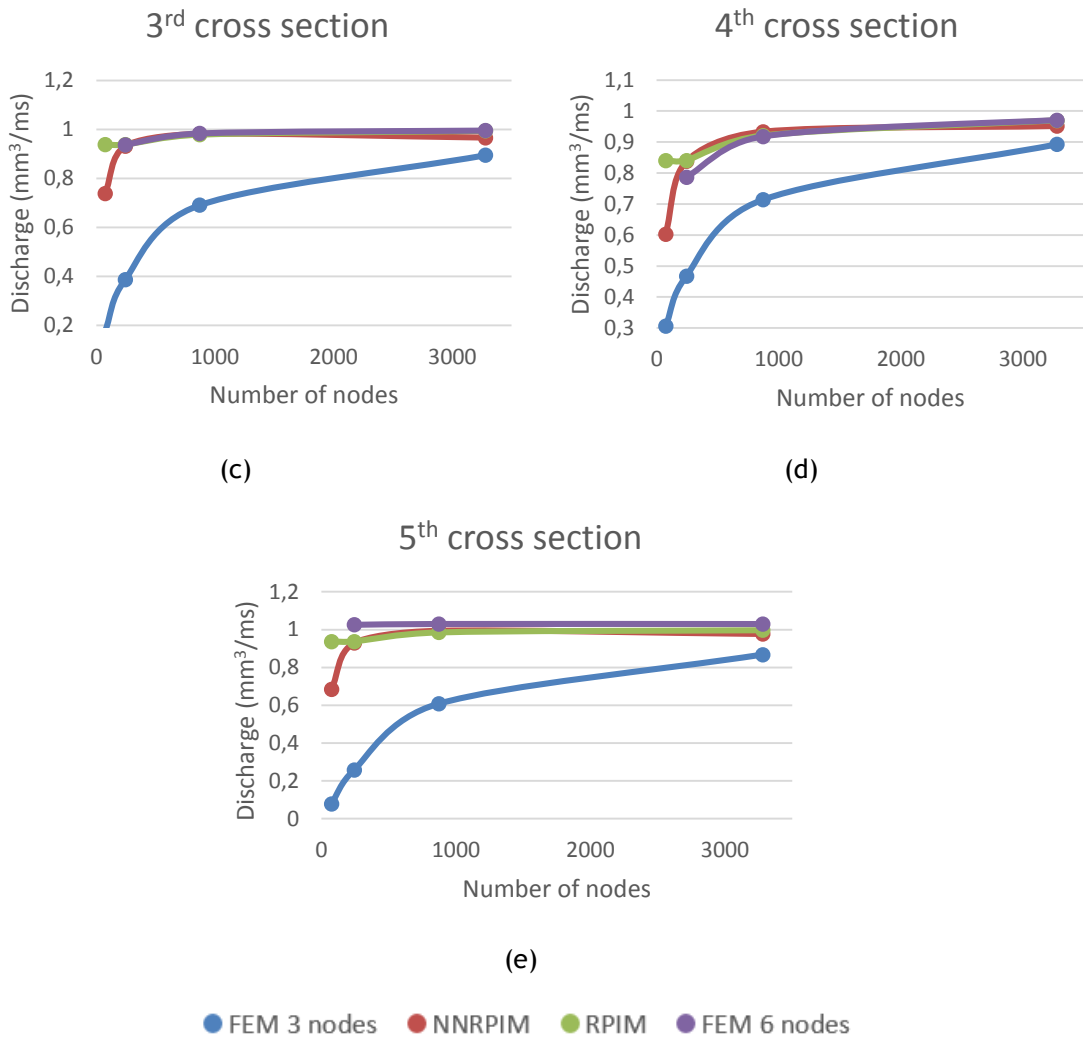
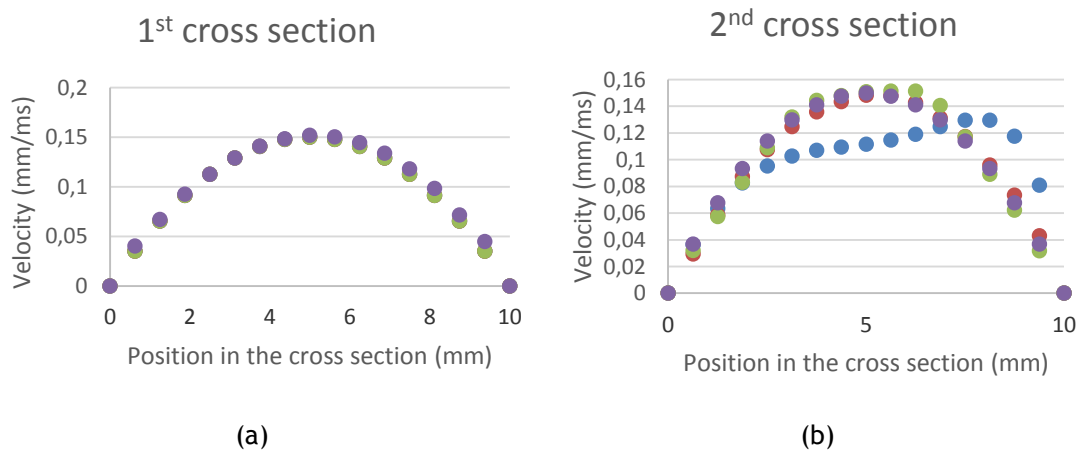


Figure 4.58 - Velocity profiles in each cross session with different methodologies

a. 1st cross section b. 2nd cross section c. 3rd cross section d. 4th cross section e. 5th cross section

In this case, RPIM seems to converge faster than the other methods and FEM with a 3 nodes element clearly the worst performance.



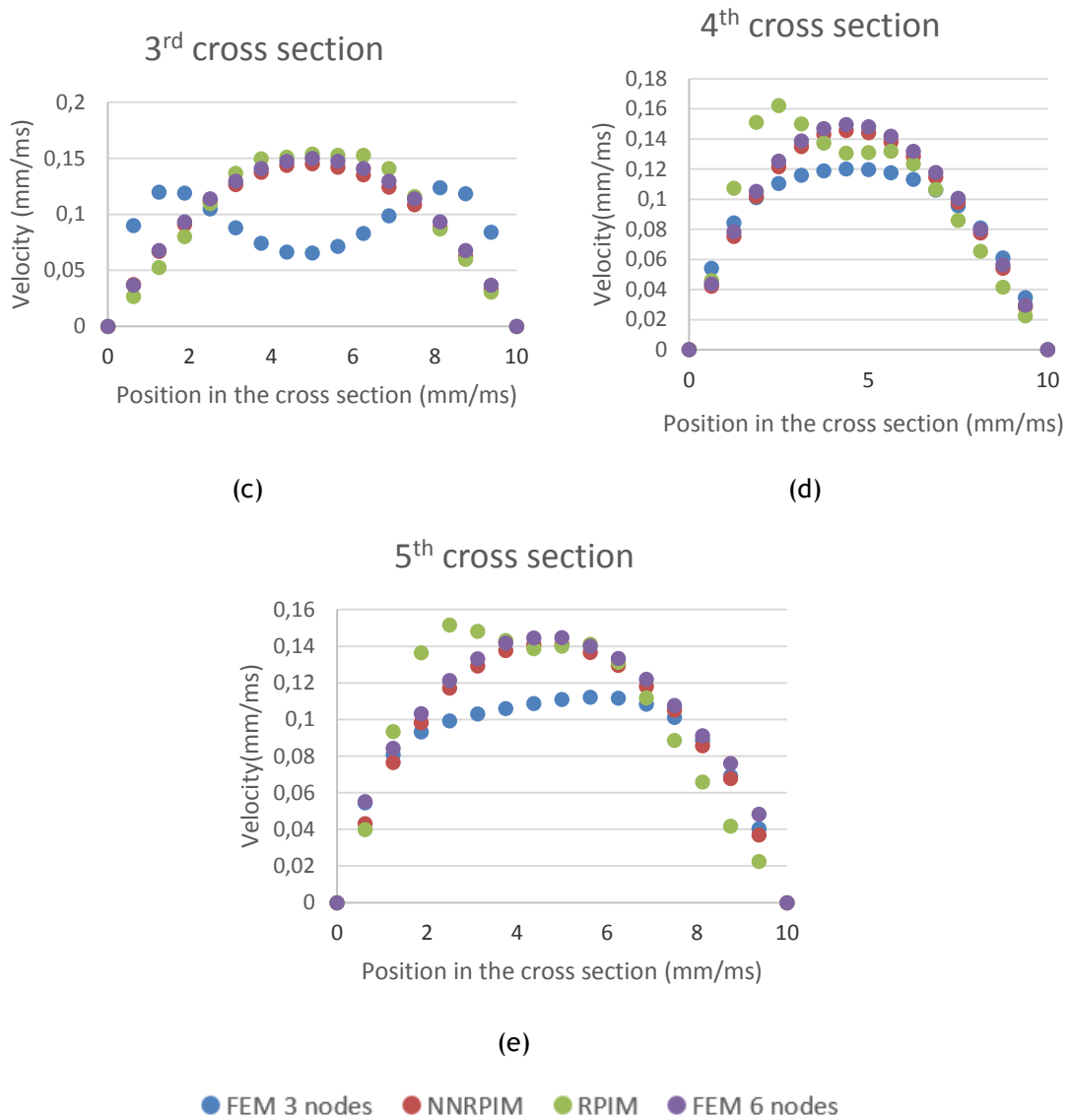


Figure 4.59 - Discharge in each cross session with different methodologies

- a. 1st cross section b. 2nd cross section c. 3rd cross section d. 4th cross section e. 5th cross section

4.2- 3D studies

To evaluate the performance of the three numerical methods studied, there were designed three 3D models.

In these simulations, blood was simulated as a Newtonian isotropic fluid. The viscosity is $3,5 \times 10^{-06}$ N.ms/mm² and the density is 1,05 kg/mm³.

4.2.1- Linear model

This model has a height of 30 mm and a radius of 5 mm and have 1825 nodes. To design this model, the semi-circle in Figure 4.60 was designed, and then it was extruded. The maximum velocity of this model 0,15 mm/ms. The velocity profile is an hyperbole:

$$v = (0,06x - 0,006x^2)\left(1 - \frac{1}{25}y^2\right) \quad (4.18)$$

The boundary conditions imposed are the degrees of freedom u, v and w restrained in the round lateral part, and with the v restrained in the plane y=0. To impose the velocity profile in z=0, each node in a line was considered being in a y plane, so the velocity only depends on the x position. The velocity of the outliers was calculated individually.

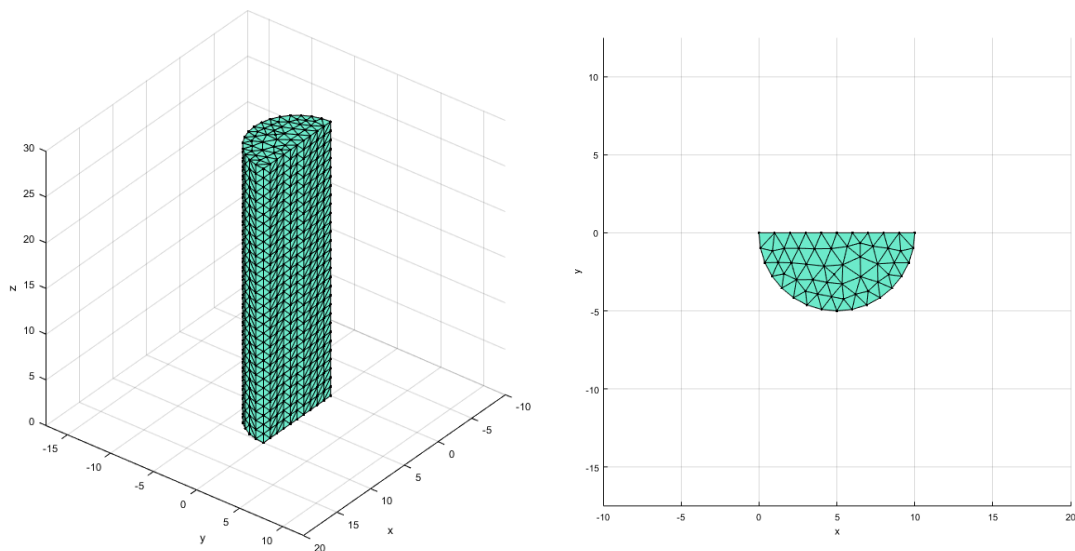


Figure 4.60 - Linear 3D model

The parameters used are shown in the Table 4.2.

Table 4.2 - RPIM and NNRPIM parameters in the linear 3D model

RPIM			NNRPIM		
Influence domain	Number of nodes inside the influence domain	27	Influence cells	Order	Second
RPI shape functions	Parameter c	0.0001	RPI shape functions	Parameter c	0.0001
	Parameter p	0.9999		Parameter p	0.9999
	Polynomial	Constant		Polynomial	Constant
Integration scheme	Gauss points	0	Integration scheme	Integration	1 (full integration)

4.2.1.1 - FEM analysis

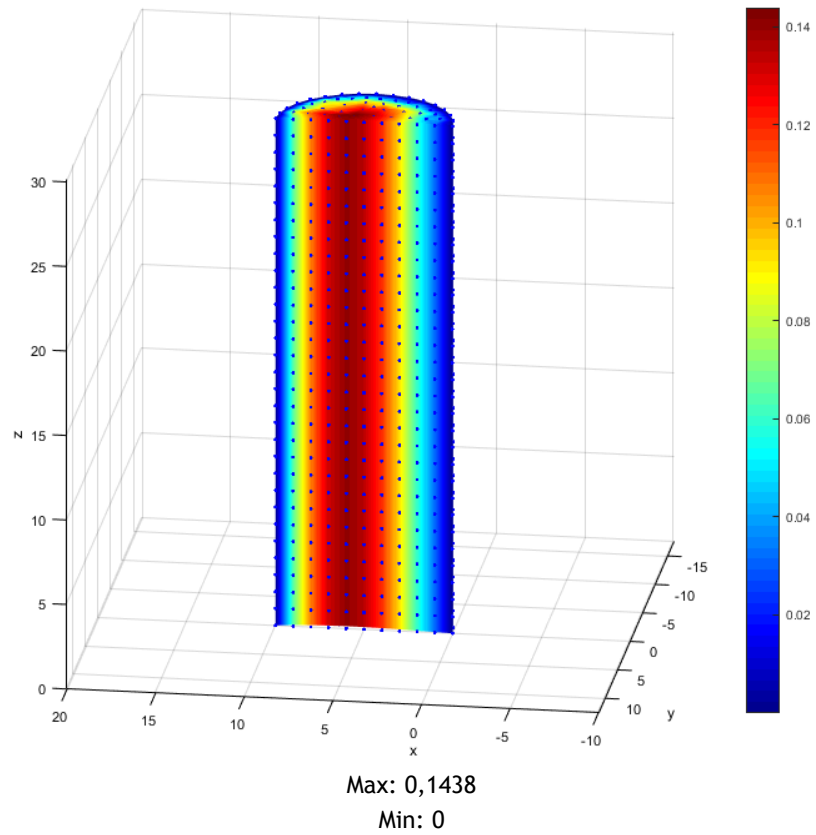


Figure 4.61 - Linear 3D model FEM analysis

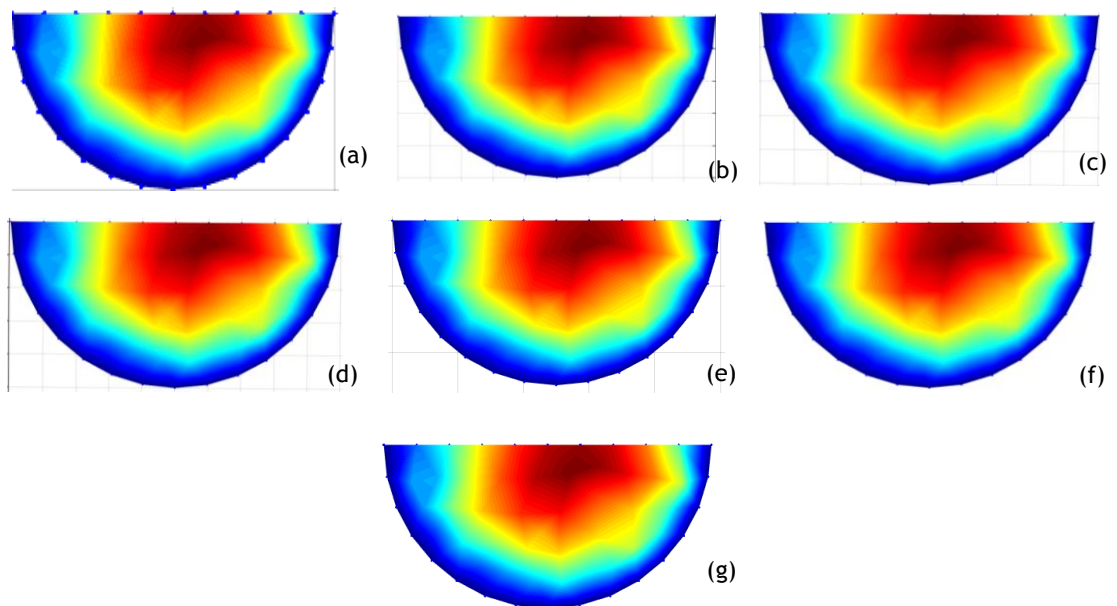


Figure 4.62 - Linear 3D model FEM analysis - cross section views
a. $x=0$ b. $x=5$ c. $x=10$ d. $x=15$ e. $x=20$ f. $x=25$ g. $x=30$

4.2.1.2- NNRPIM analysis

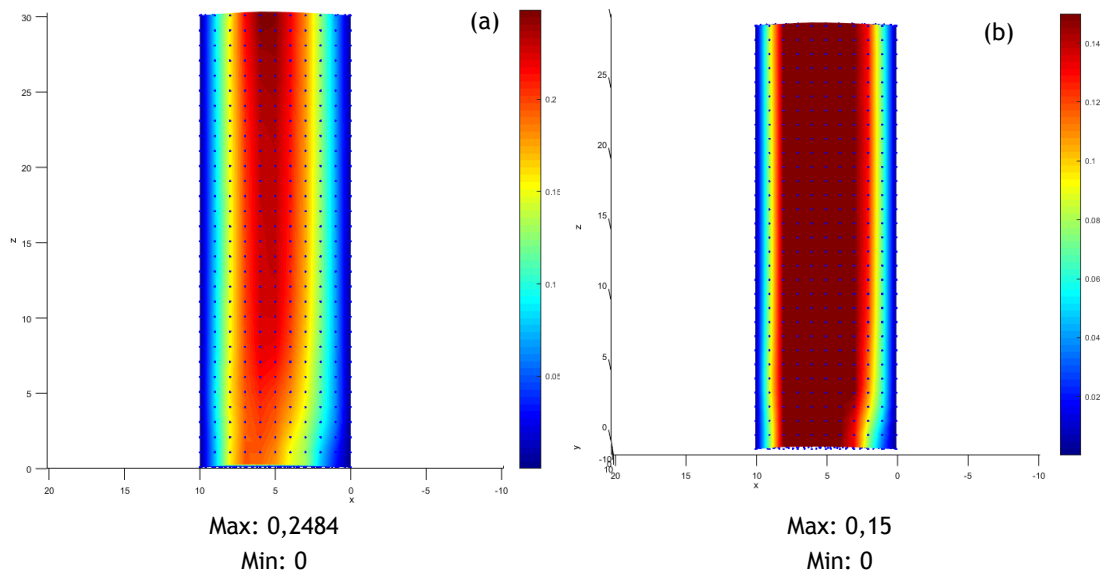


Figure 4.63 - Linear 3D model NNRPIM analysis
 a. non-scaled b. scale with maximum velocity 0.15 mm/ms

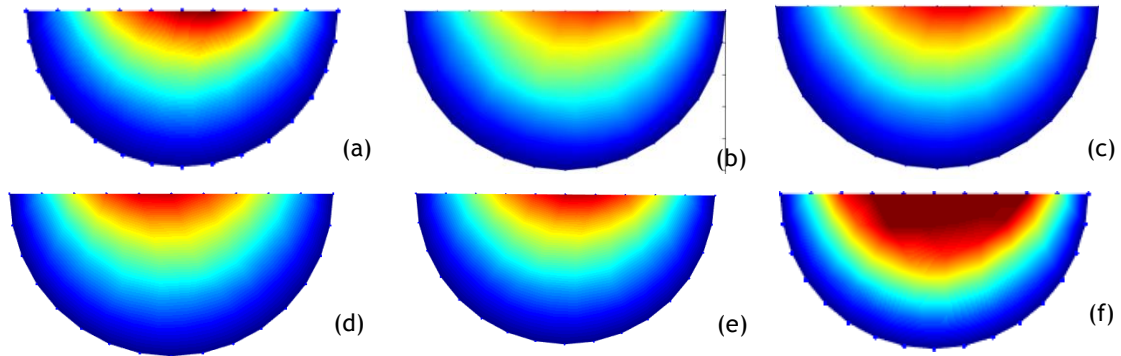
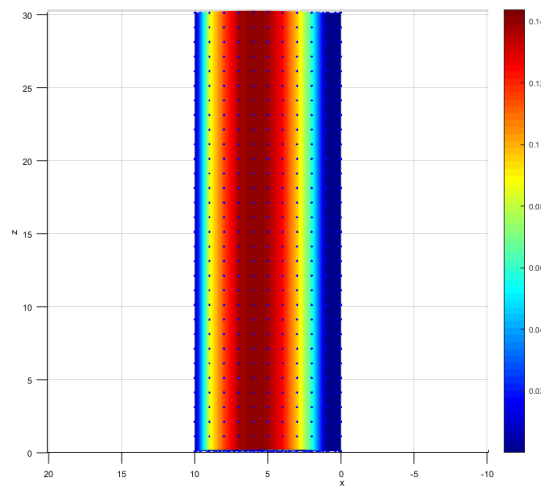


Figure 4.64 - Linear 3D model NNRPIM analysis
 a. x=0 b. x=5 c. x=10 d. x=15 e. x=30 (non-scaled)
 f. x=30 (scale with maximum velocity 0.15 mm/ms)

4.2.1.3- RPIM analysis



Max: 0,1438

Min: 0

Figure 4.65 - Linear 3D model RPIM analysis

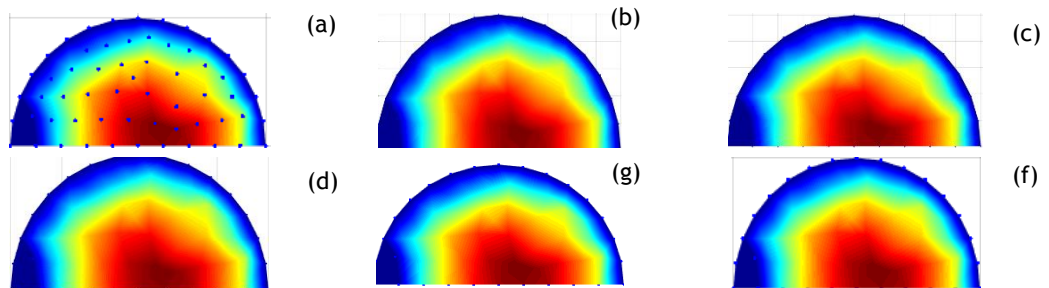


Figure 4.66 - Linear 3D model NNRPIM analysis

a. x=0 b. x=5 c. x=10 d. x=15 e. x=25 f. x=30 (non-scaled)

4.2.1.4- Discussion

The maximum velocity of the model should be 0,15 mm/ms, however, just the FEM and RPIM analysis have a maximum velocity close to the expected value. Observing the lateral profile, NNRPIM show a lower performance when compared with the FEM and RPIM.

Since the meshless methods have adjustable parameters, it is possible that the ones used in the analyses were not the optimal parameters. However, these meshless methods present a high computational cost and require a very high computational power. Therefore, optimization studies would impossible to be performed in the available time of the present project.

4.2.2- Quarter of a crown model

This model has, in the plane $y=0$, an inner radius of 20mm and an outer radius of 30mm. In the entry of the low, the model has a radius of 5mm and have 1829 nodes. The maximum velocity of this model 0,15 mm/ms. The velocity profile is an hyperbole:

$$v = (0,06x - 0,006x^2)\left(1 - \frac{1}{25}y^2\right) \quad (4.19)$$

The boundary conditions imposed are the degrees of freedom u , v and w restrained in the round lateral part, and with the v restrained in the plane $y=0$. To impose the velocity profile in $z=0$, each node in a line was considered being in a y plane, so the velocity only depends on the x position. The velocity of the outliers was calculated individually.

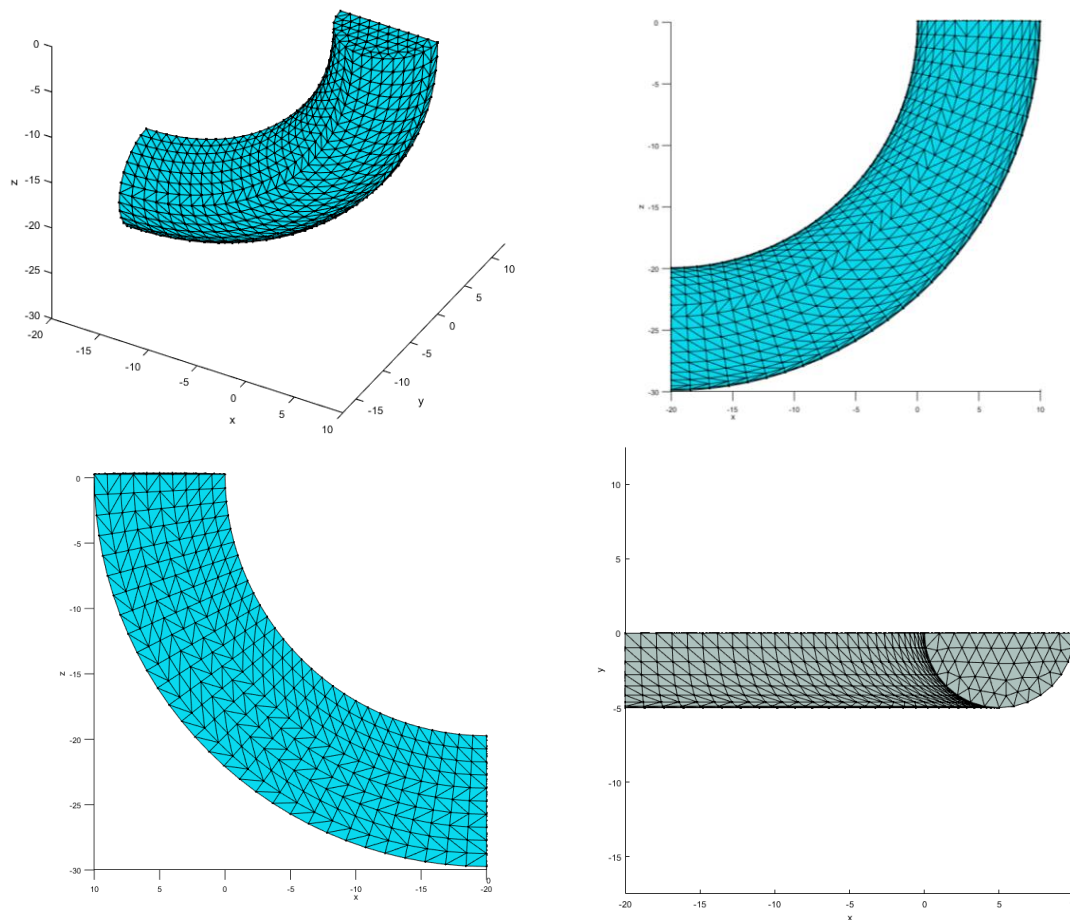


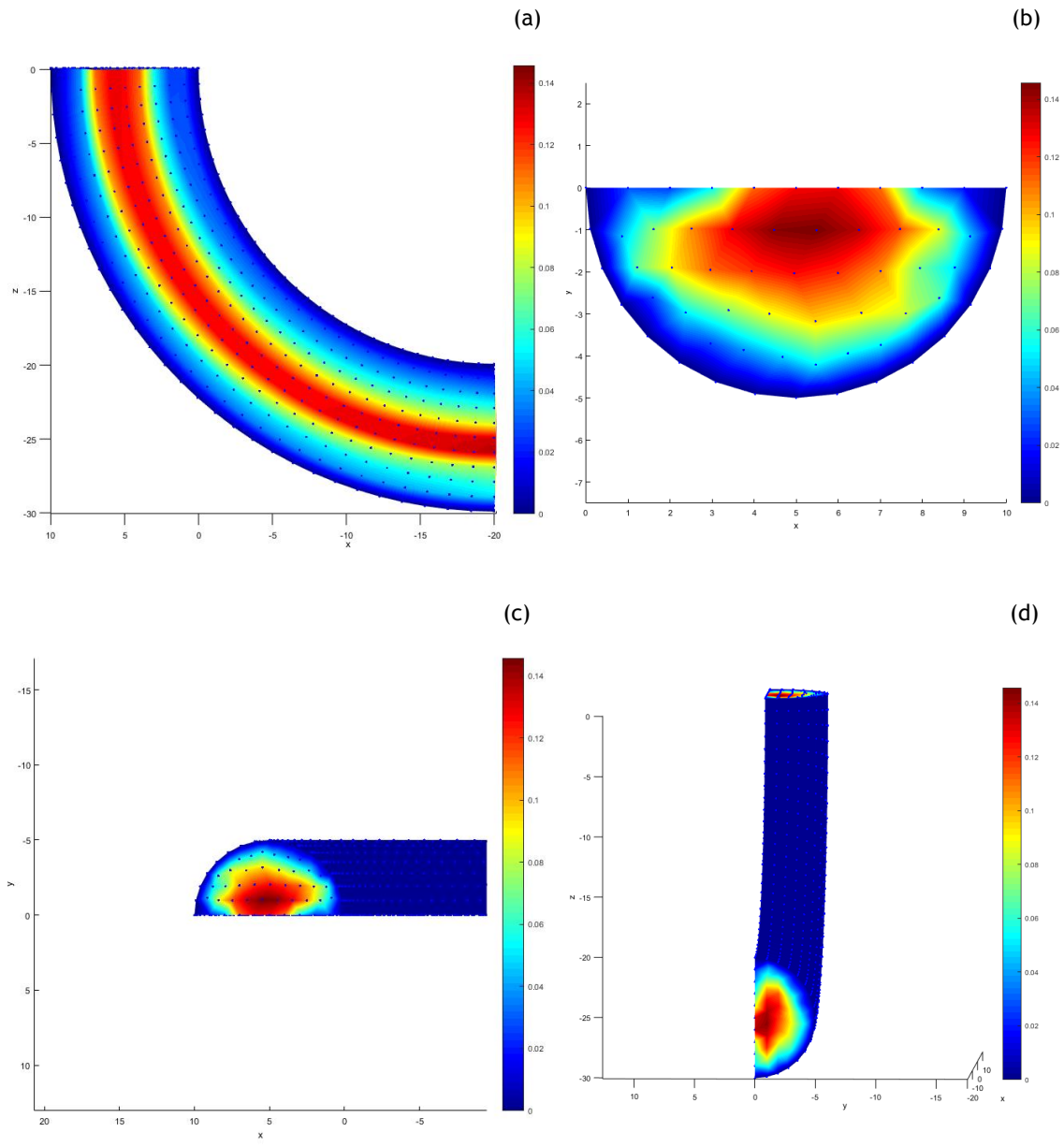
Figure 4.67 - Quarter circular crown model

The parameters used in this analysis are in the Table 4.3.

Table 4.3 - RPIM and NNRPIM parameters in the quarter circular crown 3D model

RPIM			NNRPIM		
Influence domain	Number of nodes inside the influence domain	27	Influence cells	Order	Second
RPI shape functions	Parameter c	1,42	RPI shape functions	Parameter c	0.0001
	Parameter p	1,03		Parameter p	0.9999
	Polynomial	Constant		Polynomial	Constant
Integration scheme	Gauss points	0	Integration scheme	Integration	1 (full integration)

4.2.2.1- FEM analysis



Max: 0,1457
Min: 0

Figure 4.68 - Quarter circular crown model analysed with FEM
a. lateral view b. plane z=0 c. plane z=0 d. plane x=-20

4.2.2.2- NNRPIM analysis

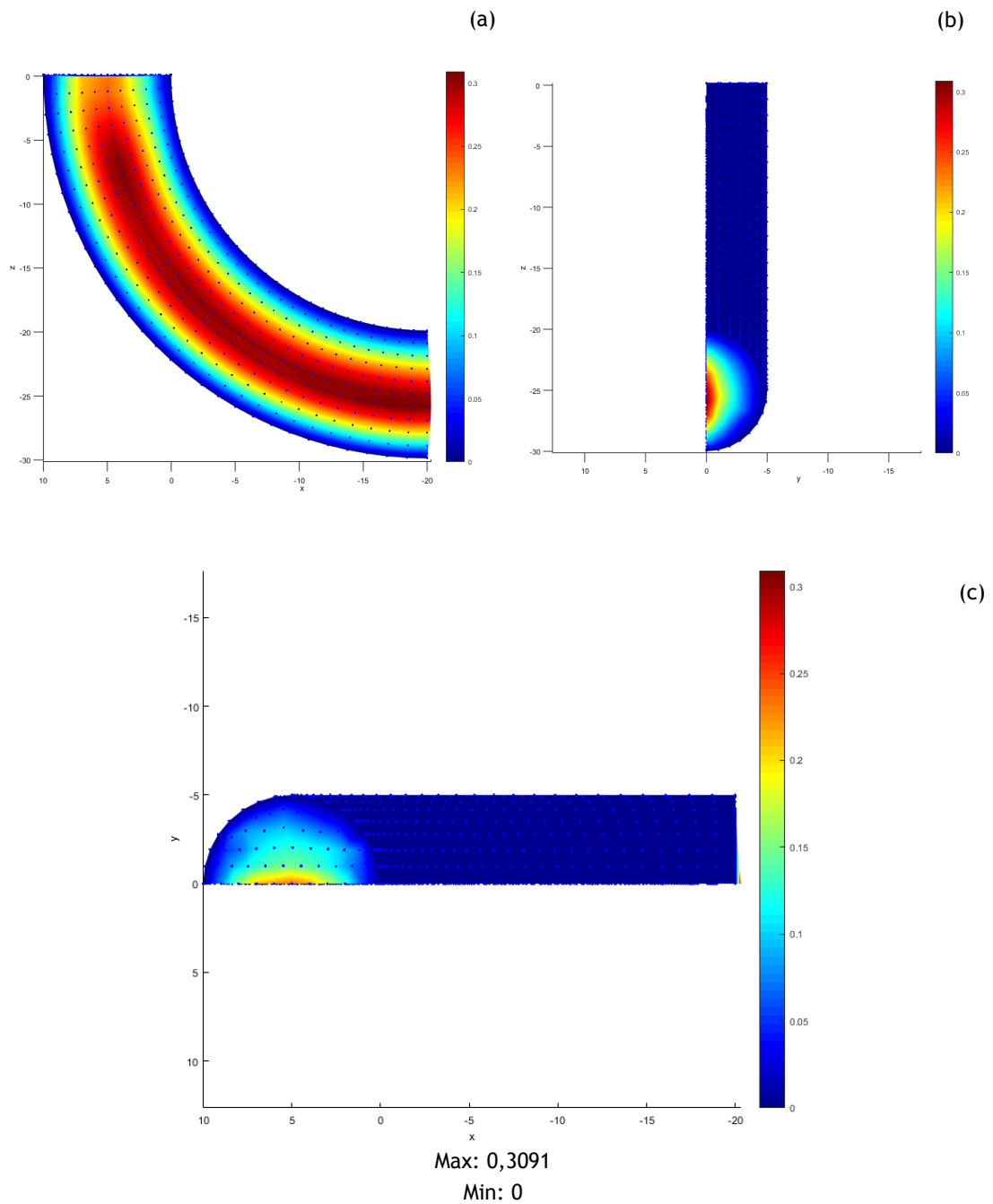


Figure 4.69 - Quarter circular crown model analysed with NNRPIM
a. lateral view b. plane $x=-20$ c. plane $z=0$

4.2.2.3- RPIM analysis

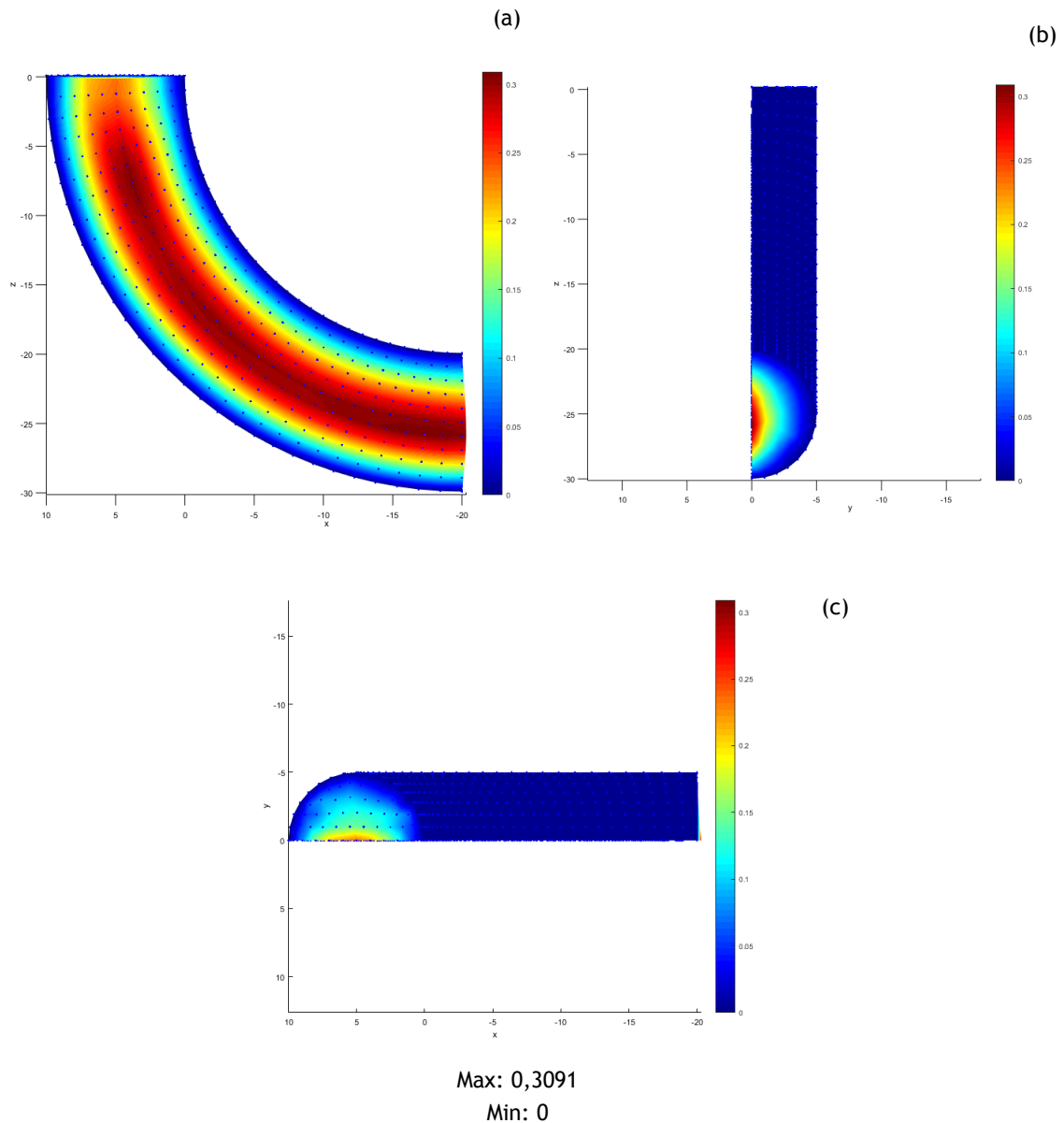


Figure 4.70 - Quarter circular crown model analysed with RPIM
a. lateral view b. plane $x=-20$ c. plane $z=0$

4.2.2.4- Discussion

In this case, the conclusions are the same that in the linear model. The FEM analysis shows a better performance.

The remarks about these analysis are the same that the linear model: RPIM and NNRPIM have adjustable parameters, which can lead to improvements to the results. However, these meshless methods present a high computational cost and require a very high computational power. Therefore, optimization studies would impossible to be performed in the available time of the present project.

4.2.3- Double curve model

This model has a radius of 5 mm and have 4235 nodes. More details can be found in the Figure 4.71. The velocity profile is an hyperbole:

$$v = (0,06x - 0,006x^2)\left(1 - \frac{1}{25}y^2\right) \quad (4.20)$$

The boundary conditions imposed are the dofs u , v and w restrained in the round lateral part, and with the v restrained in the plane $y=0$. To impose the velocity profile in $z=0$, each node in a line was considered being in a y plane, so the velocity only depends on the x position. The velocity of the outliers was calculated individually.

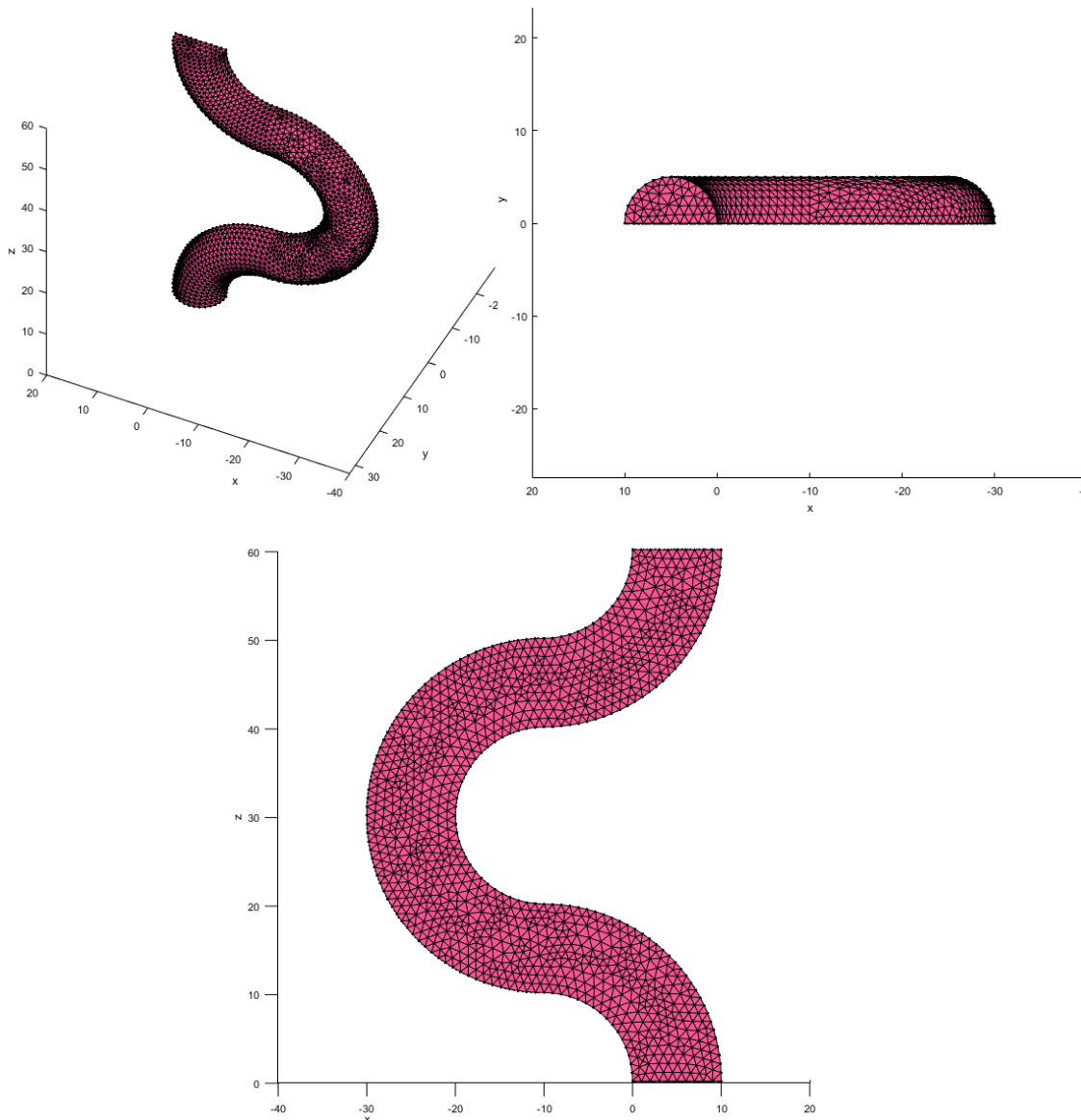


Figure 4.71 - Double curve model

The parameters used in this analysis are in the Table 4.3

Table 4.4 - RPIM and NNRPIM parameters in the half circular crown 3D model

RPIM			NNRPIM		
Influence domain	Number of nodes inside the influence domain	27	Influence cells	Order	Second
	RPI shape functions	Parameter c 0.0001 Parameter p 0.9999 Polynomial Constant		RPI shape functions	Parameter c 0.0001 Parameter p 0.9999 Polynomial Constant
Integration scheme	Gauss points	1	Integration scheme	Integration	1 (full integration)

4.2.3.1- FEM analysis

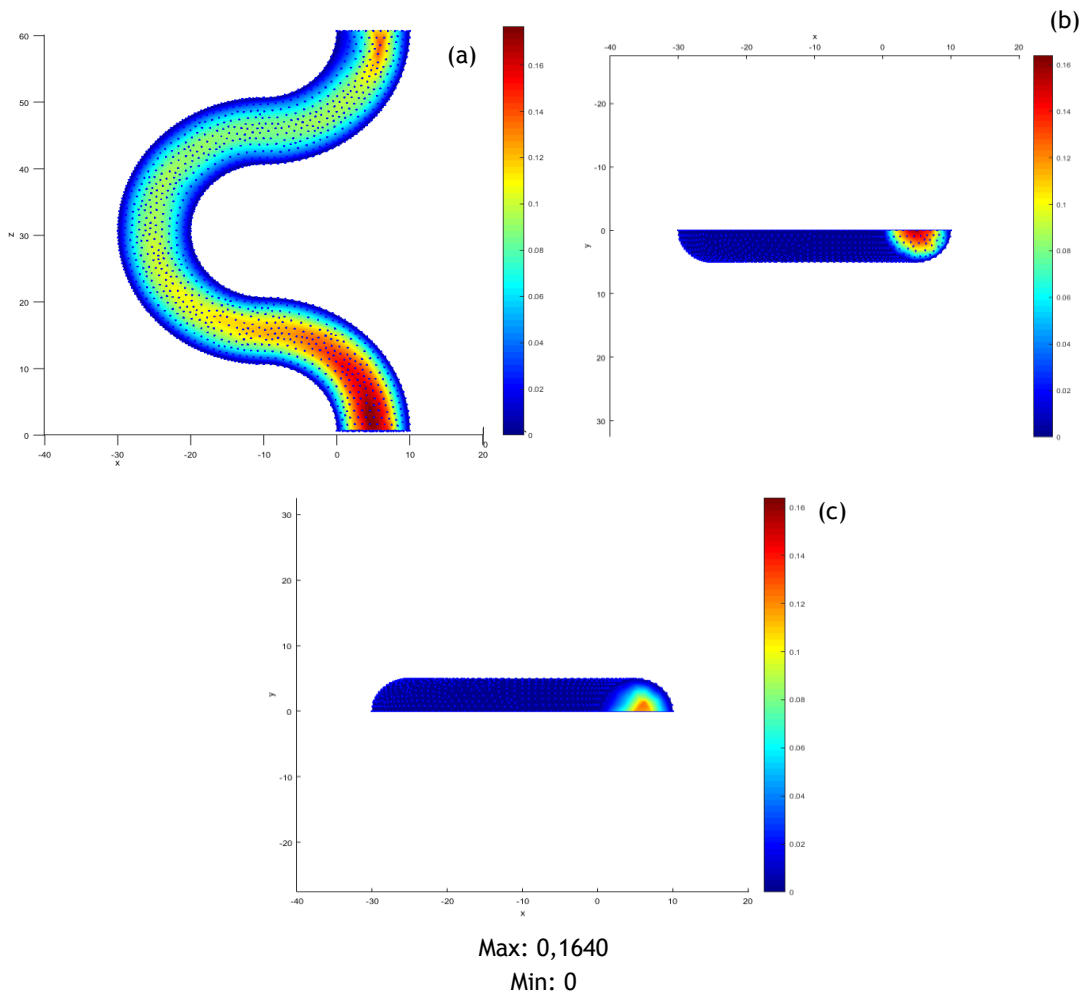
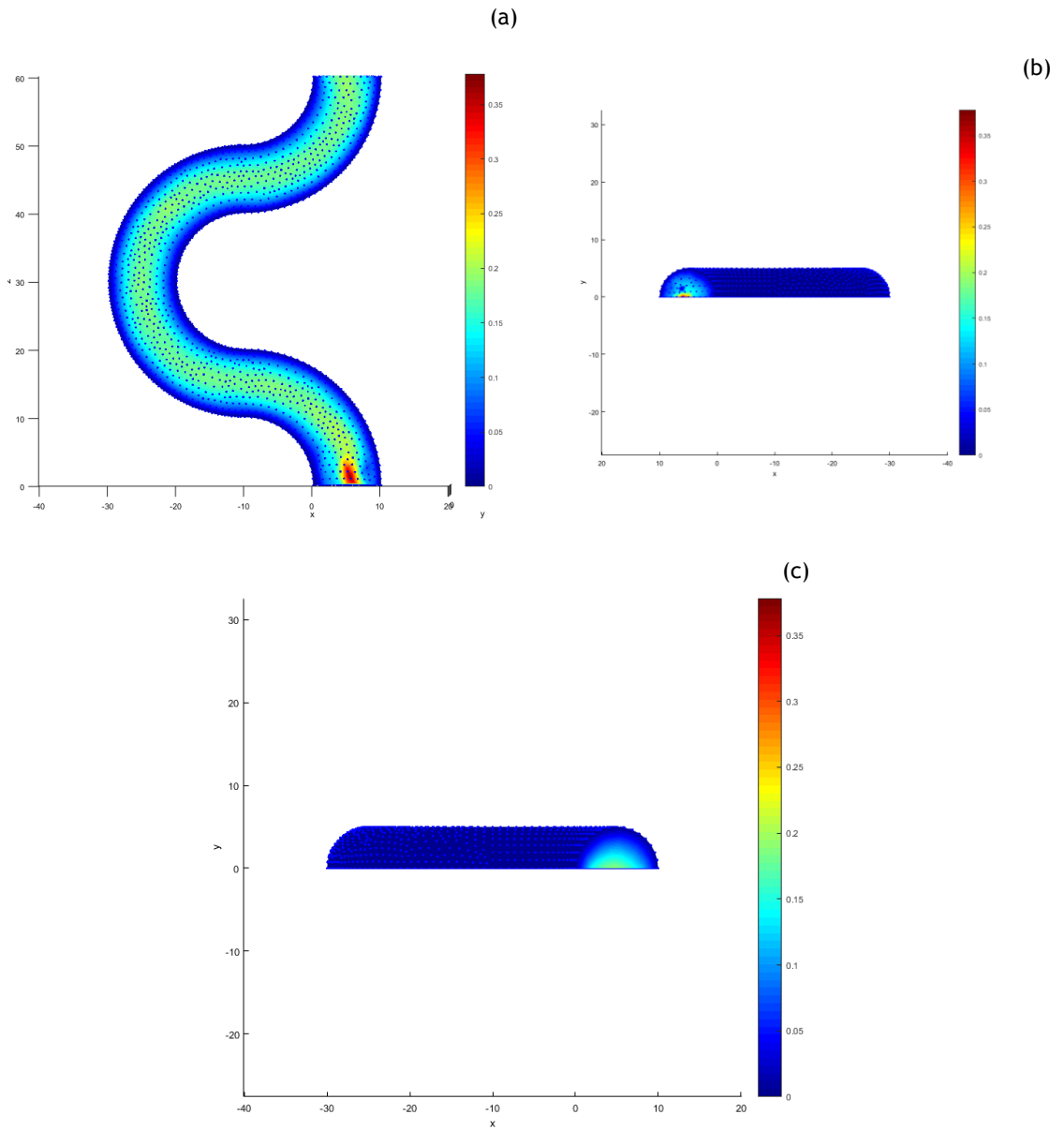


Figure 4.72 - Double curve model analysed with FEM
a. lateral view b. plane z=0 c. plane z=60

4.2.3.2- NNRPIM analysis



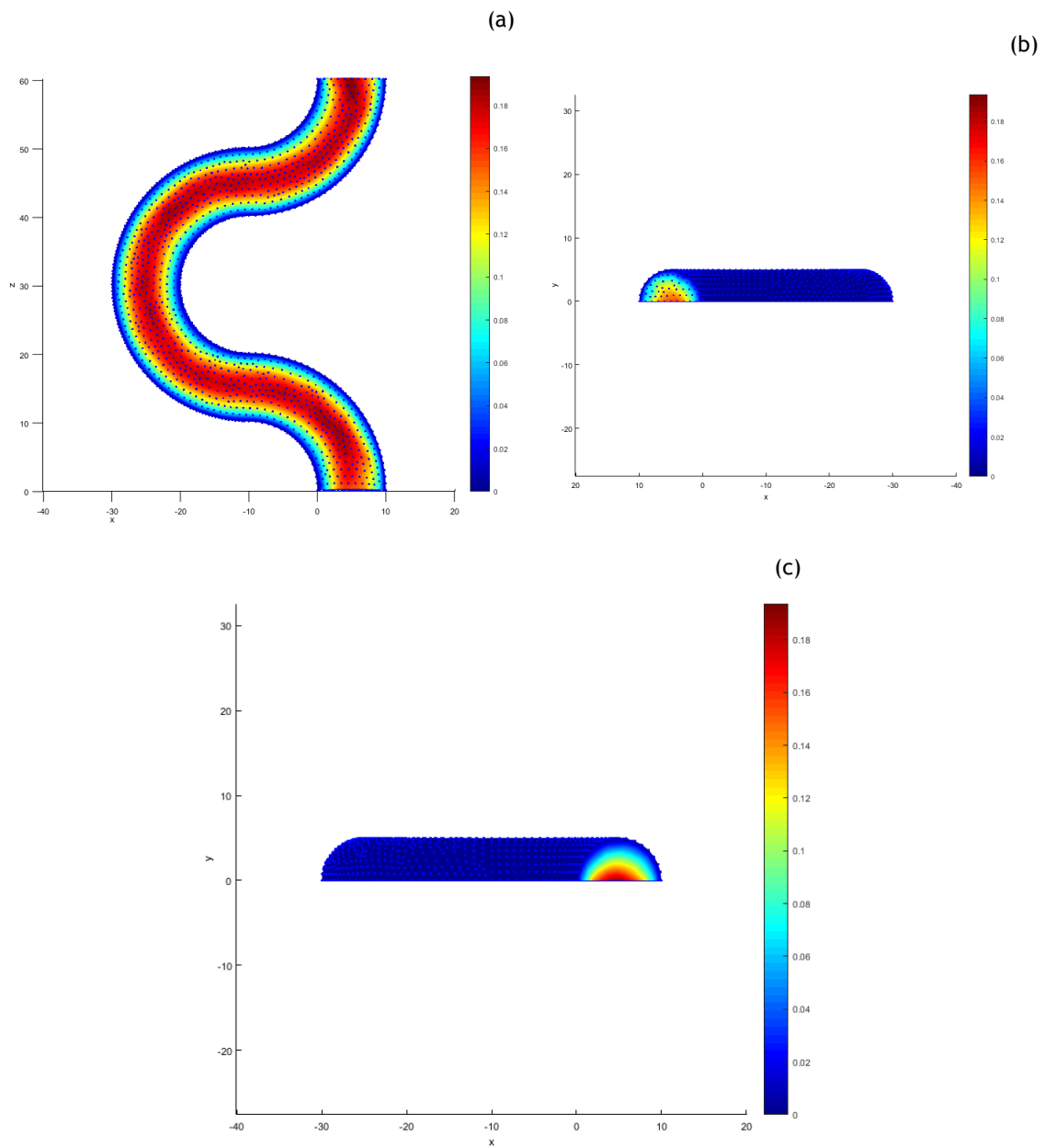
Max: 0,3784

Min: 0

Figure 4.73 - Double curve model analysed with RPIM

a. lateral view b. plane $z=0$ c. plane $z=60$

4.2.3.3- RPIM analysis



Max: 0,1937
 Min: 0

Figure 4.74 - Double curve model analysed with RPIM
 a. lateral view b. plane z=0 c. plane z=60

4.2.3.4- Discussion

In this case FEM had a lower performance than the other methods. The velocity across the model is not constant and the maximum velocity in a cross section drop as low as 0,1 mm/ms.

The velocity in NNRPIM is higher than expected. The maximum velocity in a cross section in the model is between 0,15 mm/ms and 0,2 mm/ms. However, except in the initial part of the model, the velocity is constant.

In the RPIM analysis, there are not significant increases in velocity along the model, although, the maximum velocity is higher than expected.

4.2.4- General remarks

As already mentioned, the RPIM and NNRPIM have adjustable parameters. Thus, possibly, the parameters used are not the optimal ones. More research is required in this field. Nevertheless, more powerful computational resources must be used, since the present ones are not capable to efficiently determine the optimal parameters (influence domain size, integration points scheme, polynomial basis, shape parameters).

Chapter 5

Case studies

To validate these methods, it is necessary to compare with benchmark examples. The examples in this chapter are simple examples found in literature.

5.1 - Comparison with another constitutive model for blood

In the paper [48], an example of a tube with a step with another rheological model for blood was studied. The example is represented in the Figure 5.1.

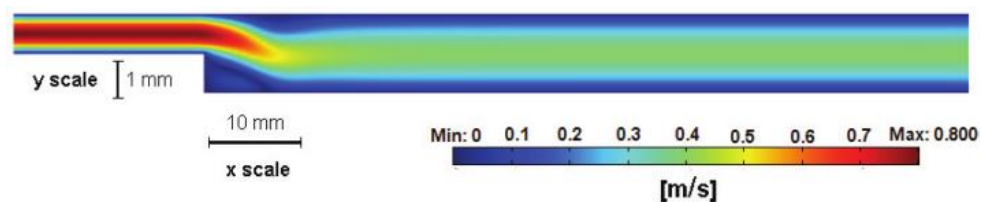


Figure 5.1 - Velocity field for the Carreau model for inlet centre line velocities of 0.8 m/s [48]

In this model, the inlet velocity is 0,8 m/s, which is equivalent to 0,8 mm/ms. The model have 1 mm in the entry of the flow, 1 mm of step, 20 mm of length in the narrow part of the tube and 100 mm in the total length, which is represented in Figure 5.2.

The boundary conditions are similar to the ones used in the convergence tests, except for the inlet velocity. In the paper, the model has 7000 elements.

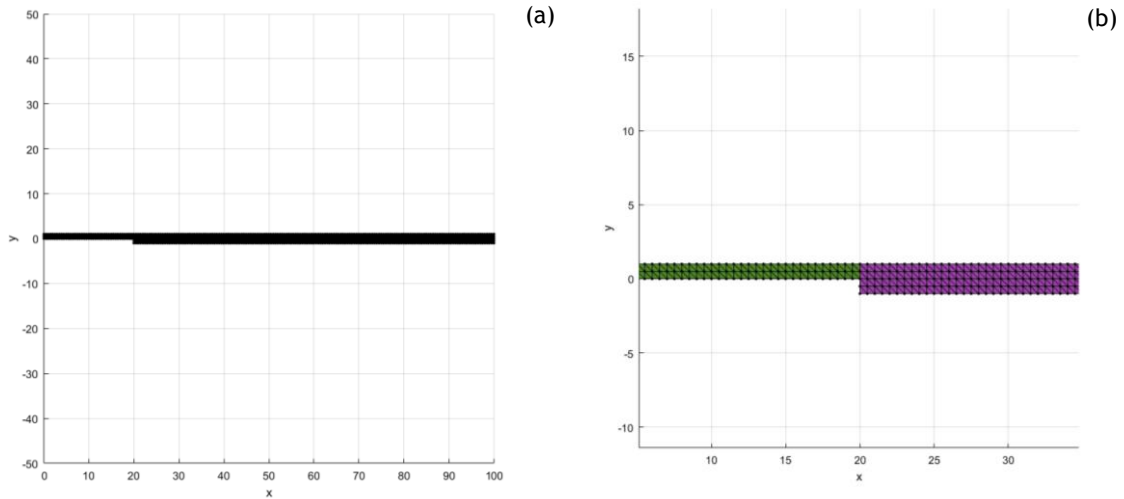


Figure 5.2 - Reproduced model

The model has 925 nodes and the material properties are the same used in the 2D and 3D models. The Figure 5.3 illustrate the comparison between the comparison between the Carreau model (used in [48]) and the Newtonian model.

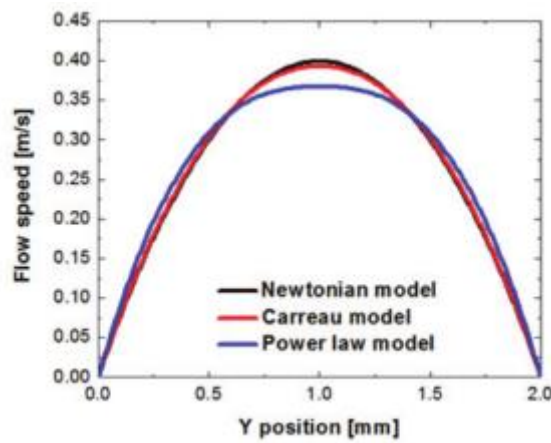



Figure 5.3 - Comparison in [48] between the velocity profiles expected

In the  Figure 5.4 is shown the results of the reproduced model.

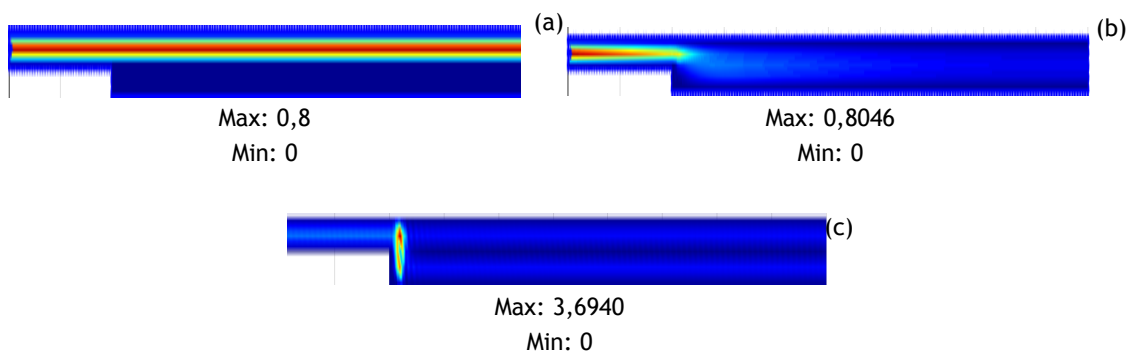


Figure 5.4 - Numerical analysis of model
a. FEM b. RPIM c. NRPIM

The RPIM is capable to reproduce the results documented in the literature. Notice that the RPIM's and NNRPIM's parameters used are the standard recommended by the software, shown in Table 4.1. The results show that the FEM technique does not recognize the section variation, and the NNRPIM produces an atypical result. In order to improve the results, the parameters were modified, nevertheless the results did not change. It is possible that the level of discretization is not enough, as in chapter 4, indicating that the discretization level can influence significantly the results. As it can be seen in Figure 5.3, at this velocity, the velocity profile of the Carreau model is close to the Newtonian model, confirming that blood can be simulated as a Newtonian model in certain conditions.

5.2 - Bifurcation

Bifurcations are also a benchmark in blood flow studies. The example used in this work is from [49].

In the paper, the blood was assumed isotropic, incompressible, with constant density and viscosity Newtonian fluid and the model was studied with FEM. The viscosity is $3,5 \times 10^{-06}$ N.ms/mm² and the density is 1,05 kg/mm³. The mesh used in the paper is in Figure 5.5 (b). The model used in this study tried to reproduce as close as possible the model in the paper.

The dimensions of the model were not showed in the paper. The paper only indicates that it is an intracranial bifurcation vessel and the entry velocity of 0,18 m/s. Based on these information, the diameter used was based on the diameter of the basilar artery [50][51], 2,7 mm. The rest of the measurements were defined using a proportion rule.

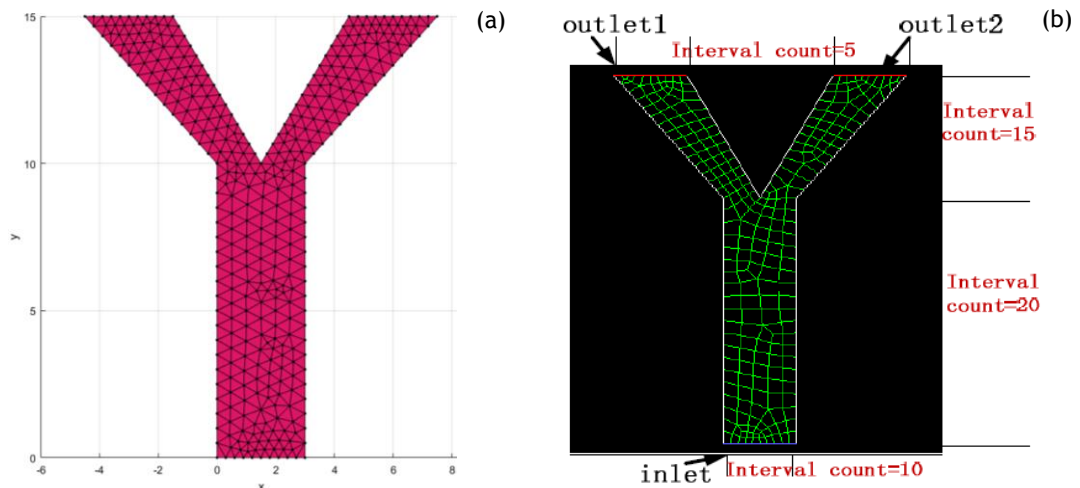


Figure 5.5 - Bifurcation models
a. designed in FEMAS b. present in the paper

The paper mentions an initial pressure that was not applied. The velocity was not parabolic, but constant along the entry. The walls of the vessel had the degrees of freedom constrained in u, v and w. The parameters for RPIM and NNRPIM are shown in Table 5.1.

Table 5.1 - RPIM and NNRPIM parameters in the bifurcation model with constant velocity profile

RPIM			NNRPIM		
Influence domain	Number of nodes inside the influence domain	27	Influence cells	Order	Second
RPI shape functions	Parameter c	0.0001	RPI shape functions	Parameter c	1.42
	Parameter p	0.9999		Parameter p	1.03
	Polynomial	Constant		Polynomial	Constant
Integration scheme	Gauss points	3	Integration scheme	Integration	1 (full integration)

The comparison between the results in literature and the results obtained in FEMAS are shown in the Figure 5.6.

As an alternative, a model with an initial parabolic profile with maximum velocity of 0,18 mm/ms was simulated. The parameters used are in Table 5.2 and the results are in Figure 5.7.

Table 5.2 - RPIM and NNRPIM parameters in the bifurcation model with parabolic velocity profile

RPIM			NNRPIM		
Influence domain	Number of nodes inside the influence domain	27	Influence cells	Order	Second
RPI shape functions	Parameter c	0.0001	RPI shape functions	Parameter c	1.42
	Parameter p	0.9999		Parameter p	1.03
	Polynomial	Constant		Polynomial	Constant
Integration scheme	Gauss points	1	Integration scheme	Integration	1 (full integration)

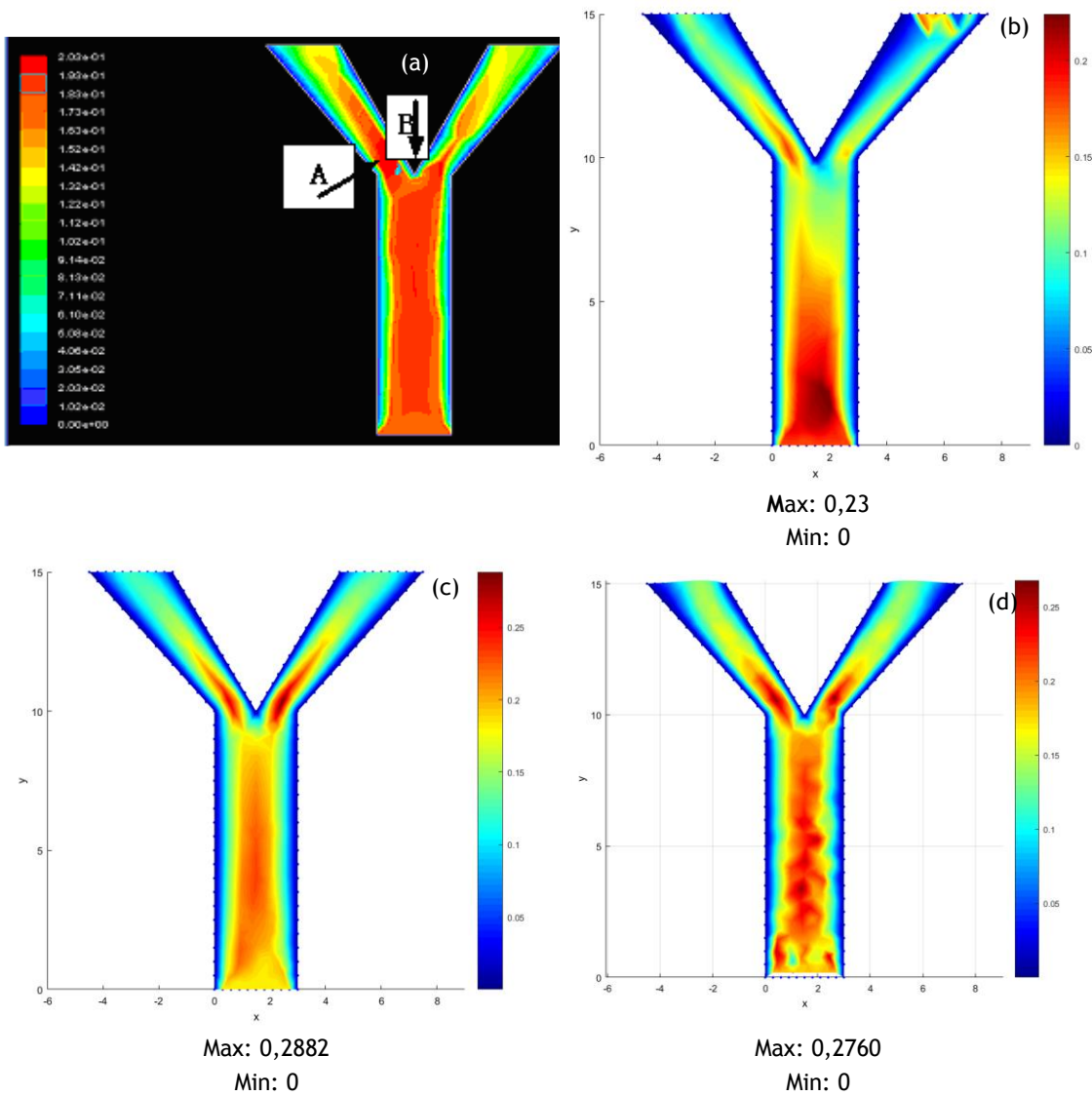


Figure 5.6 - Numerical analysis of model with the initial constant velocity
 a. result in literature b. FEM c. RPIM d. NNRPIM

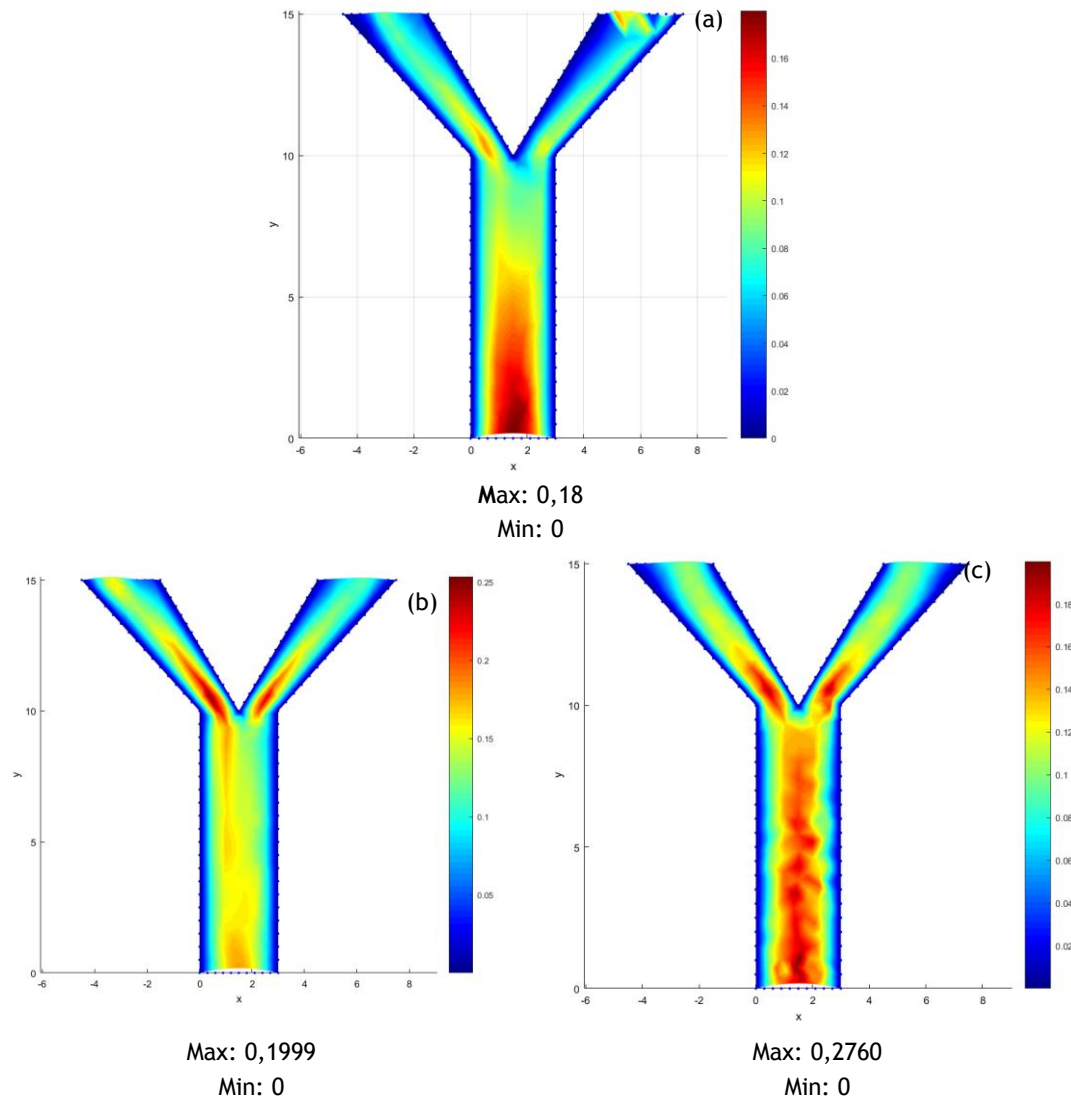


Figure 5.7 - Numerical analysis of model with the parabolic initial velocity
 a. result in literature b. FEM c. RPIM d. NNRPIM

As the figures show, the FEM has a good performance but have some artifacts in the exit of the fluid. The results which the initial velocity is constant show that NNRPIM is not capable to produce acceptable results. Nevertheless, in the study which a parabolic entry velocity profile was enforced, the NNRPIM has improved its performance, producing better results. Overall, RPIM results seem closer to the reality that the other techniques.

As showed in 2D convergence studies, the parameters in RPIM and NNRPIM are an essential factor, hence is important to study several to reach the better outcome.

5.3 - Spastic middle cerebral arteries

This case studies an example where the calibre of the vessel is abruptly reduced in a certain zone. The boundary conditions in the wall of the vessel are similar to the ones in the convergence studies. The inlet velocity is a parabolic with maximum velocity of 0,23 m/s and normal to the boundary and the degrees of freedom are restrained in u and v .

In these simulations, blood was simulated as a Newtonian isotropic fluid, where the viscosity is $3,5 \times 10^{-6}$ N.ms/mm² and the density is 1,05 kg/mm³. In the paper, the fluid was simulated in these conditions.

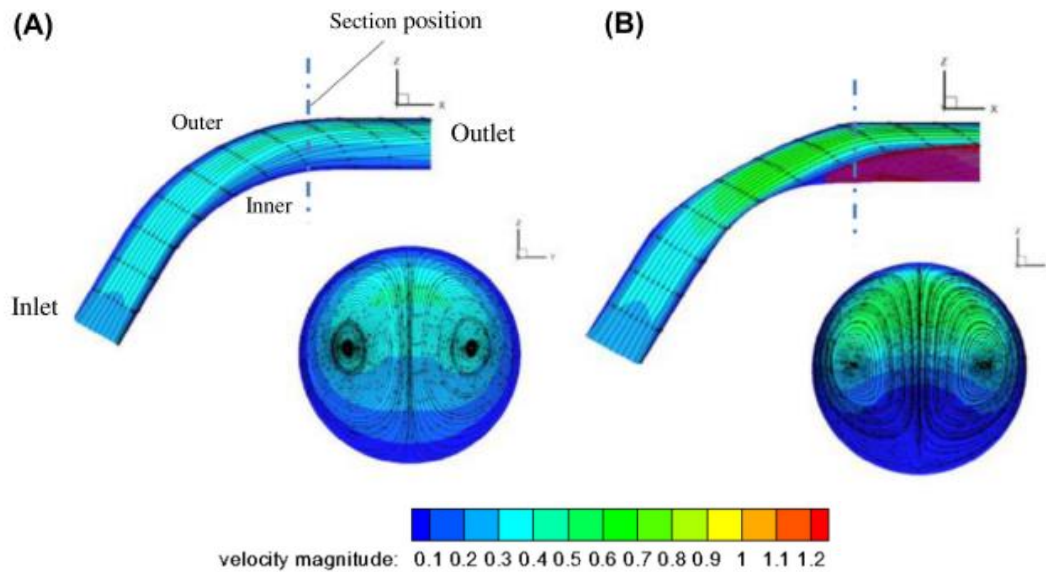


Figure 5.8 - Results presented in literature

The parameters for RPIM and NNRPIM are shown in Table 5.3 and

Table 5.4. These parameters are different from the standard ones, because, by trial and errors, these parameters showed better results.

Table 5.3 - RPIM and NNRPIM parameters in the spastic middle cerebral artery model (a)

RPIM			NNRPIM		
Influence domain	Number of nodes inside the influence domain	27	Influence cells	Order	Second
	Parameter c	0.0001		Parameter c	0.0001
RPI shape functions	Parameter p	0.9999	RPI shape functions	Parameter p	0.9999
	Polynomial	Constant		Polynomial	Constant
Integration scheme	Gauss points	3	Integration scheme	Integration	1 (full integration)

Table 5.4 - RPIM and NNRPIM parameters in the spastic middle cerebral artery model (b)

RPIM			NNRPIM		
Influence domain	Number of nodes inside the influence domain	27	Influence cells	Order	Second
RPI shape functions	Parameter c	0.0001	RPI shape functions	Parameter c	0.0001
	Parameter p	0.9999		Parameter p	0.9999
	Polynomial	Constant		Polynomial	Constant
Integration scheme	Gauss points	2	Integration scheme	Integration	1 (full integration)

The results are in the Figure 5.9 and Figure 5.10. The first model has 308 nodes and the second one have 270 nodes.

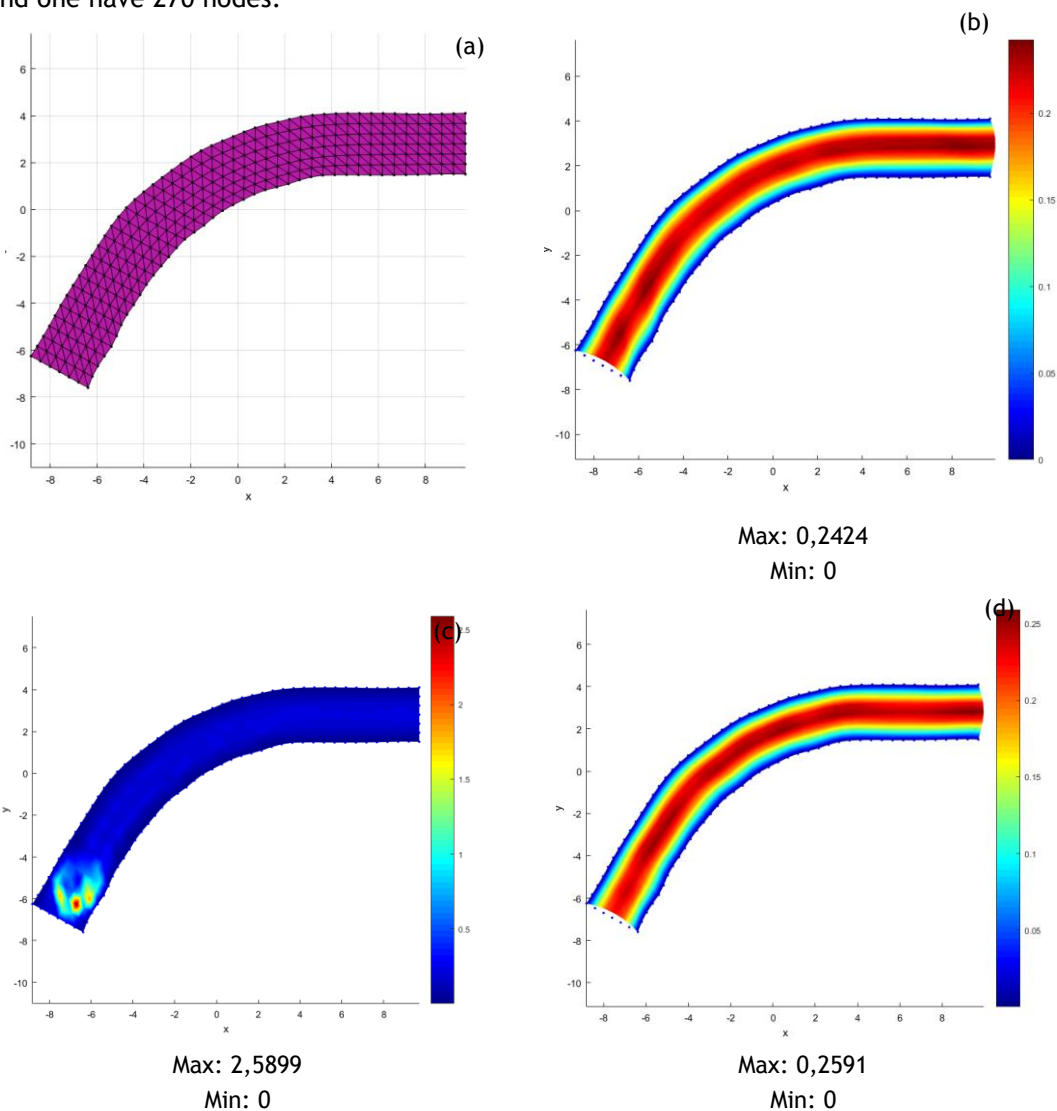


Figure 5.9 - Numerical analysis of model

a. model b. FEM c. RPIM d. NNRPIM

In this case, the maximum velocity is between 0,2 mm/ms and 0,3 mm/ms, which is the maximum velocity in Figure 5.8 (a). The RPIM has a spike in velocity, which is not expected. Both RPIM and FEM have good results. Is to notice that the discretization level is not very high, so that can influence the results of the numerical methods. In this case does not seems to be an issue, but in other cases can be.

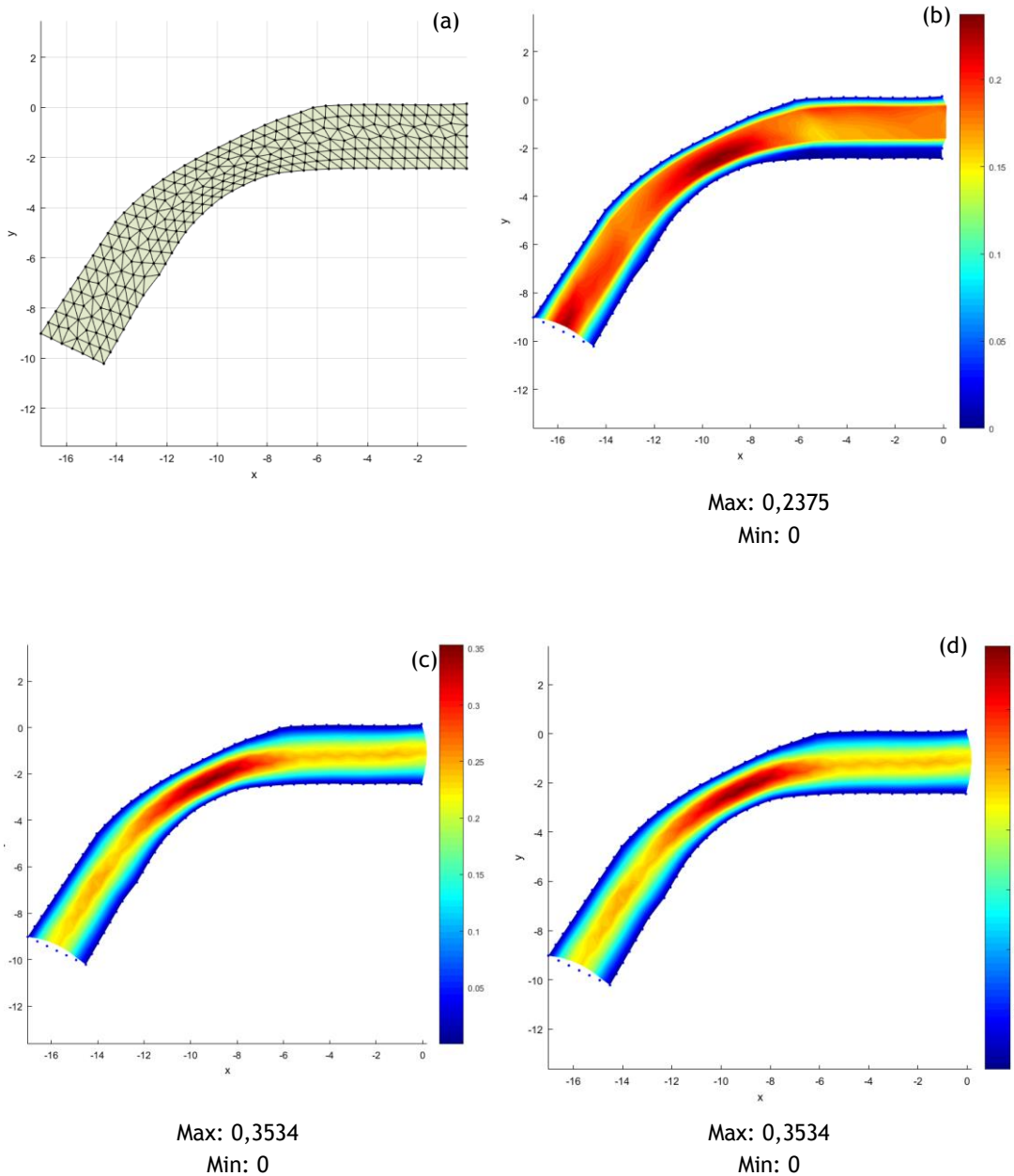


Figure 5.10 - Numerical analysis of model

a. model b. FEM c. RPIM d. NNRPIM

The results with FEM seem to be more accurate, because the zone with low velocities after the stenosis is larger. However, if the velocity range is analyzed, it is possible to see that

velocities in FEM are too low, compared with literature, so NNRPIM and RPIM are more accurate in this field. Overall, all analysis point to the normal flow when there is a narrowing of a tube.

These results could be improved increasing the level of discretization and experimenting other parameters.

5.4 - Cerebral aneurysm

This example was taken from [52]. The initial velocity is 20 mm/s. The boundary condition imposed in the entry was a parabolic with the degrees of freedom in u and v constrained. Other boundary conditions were experimented but did not have good results. The model has 522 nodes. In these simulations, blood was simulated as a Newtonian isotropic fluid, where the viscosity is $3,5 \times 10^{-06}$ N.ms/mm² and the density is 1,05 kg/mm³.

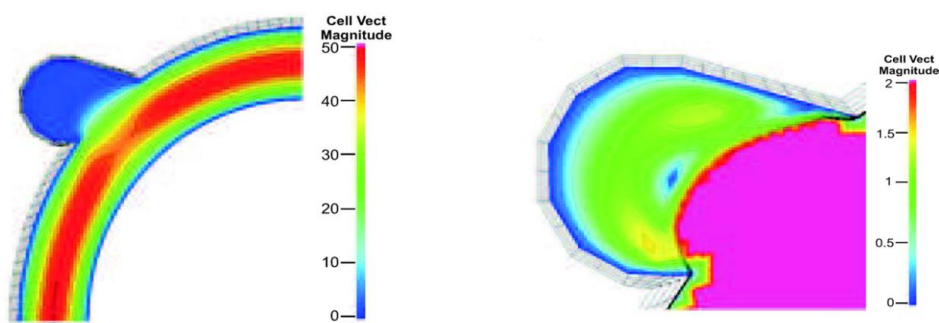


Figure 5.11 - Results presented in paper

The parameters used are in Table 5.5 and the results are in the Figure 5.2.

Table 5.5 - RPIM and NNRPIM parameters in cerebral aneurism

RPIM			NNRPIM		
Influence domain	Number of nodes inside the influence domain	27	Influence cells	Order	Second
	Parameter c	0.0001		Parameter c	0.0001
RPI shape functions	Parameter p	0.9999	RPI shape functions	Parameter p	0.9999
	Polynomial	Constant		Polynomial	Constant
Integration scheme	Gauss points	3	Integration scheme	Integration	1 (full integration)

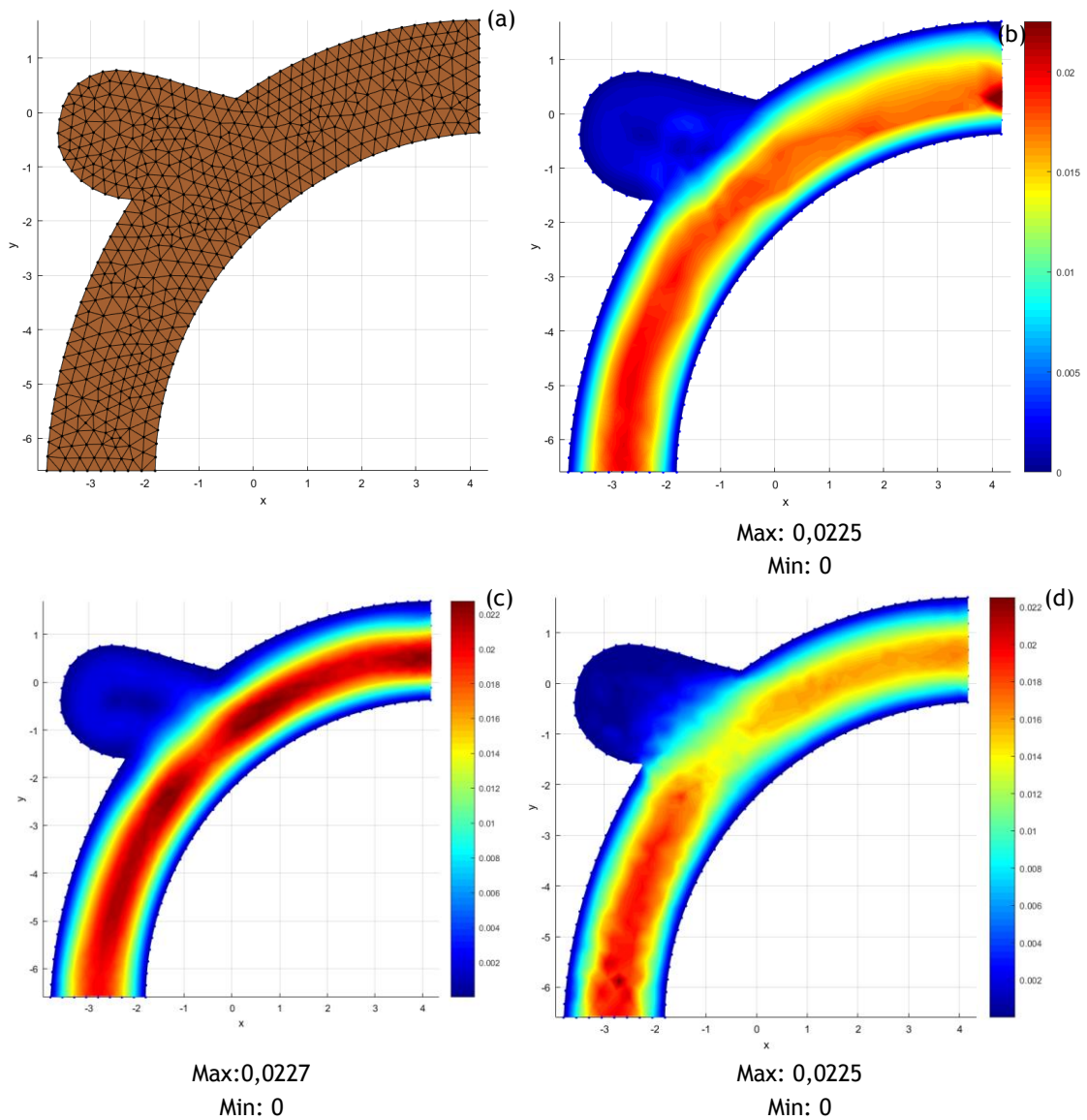


Figure 5.12 - Numerical analysis of model
a. model b. FEM c. RPIM d. NNRPIM

Comparing with the figure from literature, the RPIM analysis seems to be the closer. FEM analysis does not represent the situation where there is a decrease in velocity, in the vessel close to the aneurysm. The results already seem accurate, but further discretization could improve the results. It is to notice that NNRPIM is the analysis that shows better the characteristic aneurysm-vessel transition.

5.5 - Aortic aneurysm

This model was taken from [53]. The model has 1240 nodes and the initial velocity profile is a parabola with 0,6 mm/ms maximum velocity. In these simulations, blood was simulated

as a Newtonian isotropic fluid, where the viscosity is $3,5 \times 10^{-6}$ N.ms/mm² and the density is 1,05 kg/mm³.

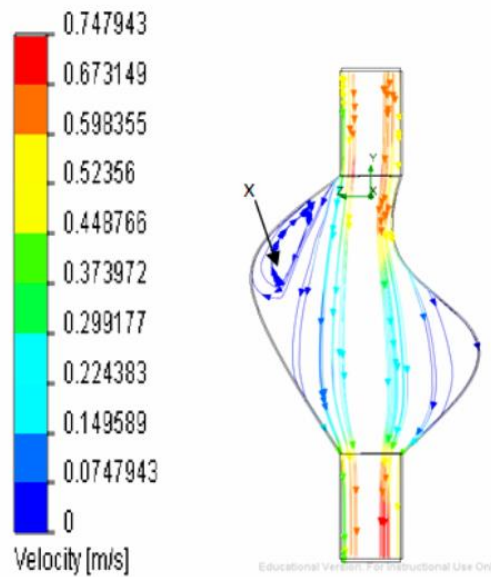


Figure 5.13 - Results presented in paper

The parameters used are in this analysis is in Table 5.6 and the results are in Figure 5.14.

Table 5.6 - RPIM and NNRPIM parameters in aortic aneurism

RPIM			NNRPIM		
Influence domain	Number of nodes inside the influence domain	27	Influence cells	Order	Second
	Parameter c	0.0001		Parameter c	0.0001
RPI shape functions	Parameter p	0.9999	RPI shape functions	Parameter p	0.9999
	Polynomial	Constant		Polynomial	Constant
	Integration scheme	Gauss points		2	Integration scheme

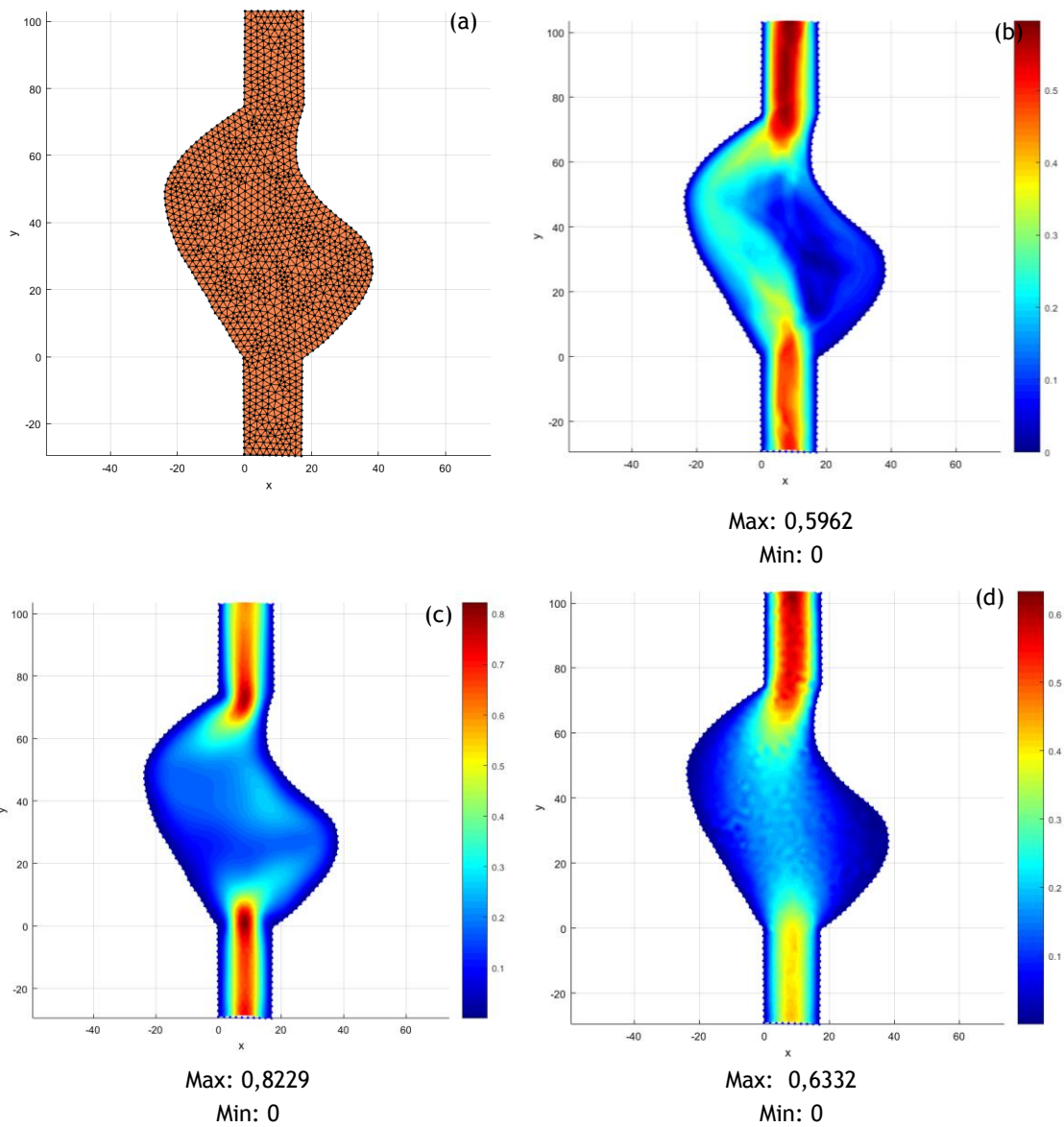


Figure 5.14 - Numerical analysis of model
a. model b. FEM c. RPIM d. NNRPIM

The NNRPIM results are the most similar with literature. Analyzing the maximum velocity, it is possible to see that it is close to the one in the literature and, second, the low velocities areas are respected in NNRPIM, which is not true in FEM, since is an area with medium velocity.

This model has a reasonable discretization level, although it could be higher, and help have better results. Other factor is the NNRPIM and RPIM factors that could influence as well.

5.6 - Real bifurcation

This model (not extracted from literature) replicates a bifurcation and have 2653 nodes where the initial velocity is a parabolic with 0,15 mm/ms. In these simulations, blood was simulated as a Newtonian isotropic fluid, where the viscosity is $3,5 \times 10^{-06}$ N.ms/mm² and the density is 1,05 kg/mm³. The parameters used were the default.

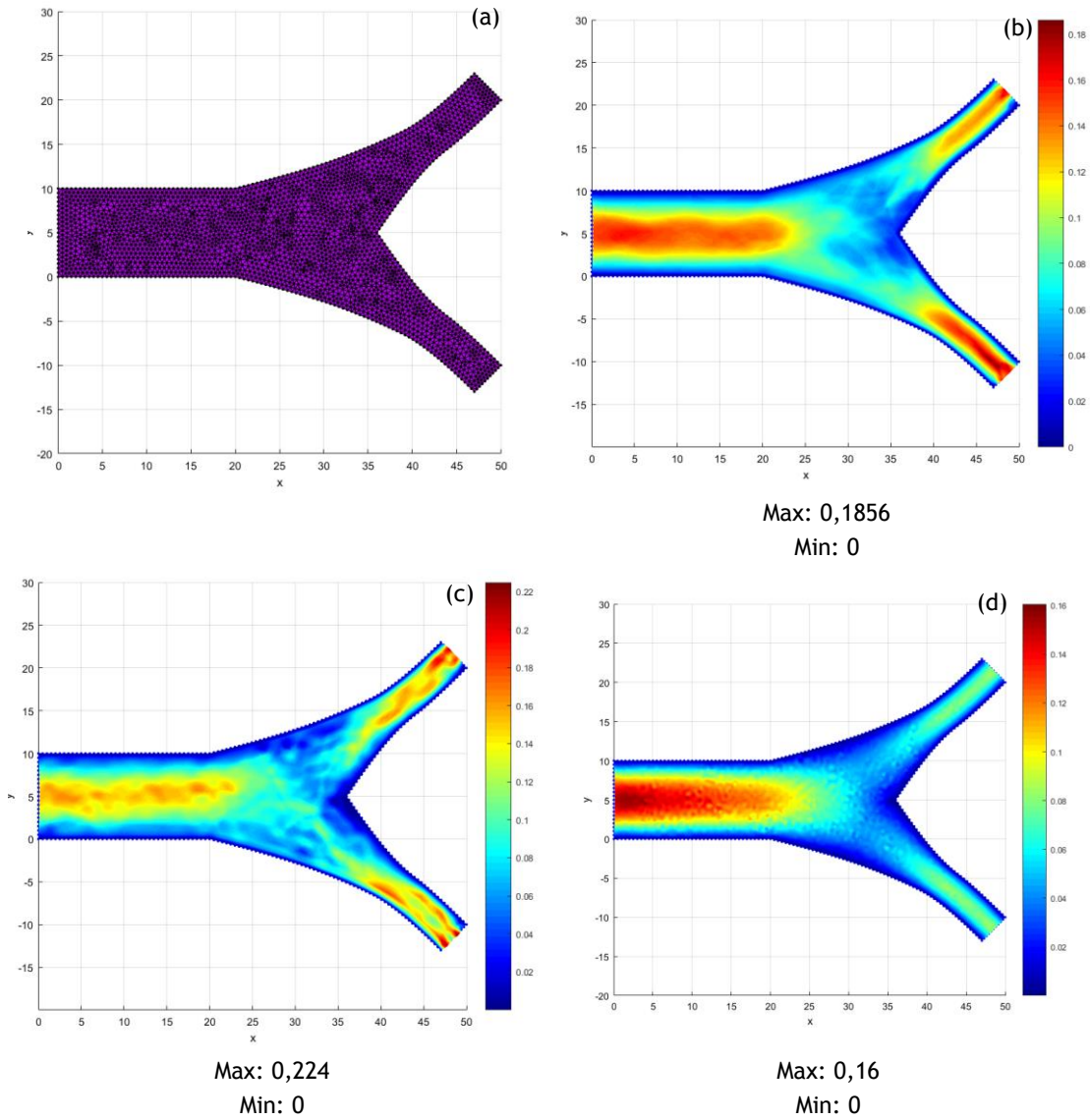


Figure 5.15 - Numerical analysis of model
 a. model b. FEM c. RPIM d. NNRPIM

As it is not possible to compare the results obtained with the literature. It is not possible to affirm which result is more correct but the results from RPIM seem to be inaccurate. The most accurate seems to be from NNRPIM which have a symmetrical velocity map but it appears “pixelized”. FEM, by other hand does not have a symmetrical velocity map.

Chapter 6

Conclusions and future work

Cardiovascular diseases and blood flow related problems are a huge burden in our society and national health system. In this work, the Radial Point Interpolation Method (RPIM) and the Natural Neighbour Radial Point Interpolation Method (NNRPIM) were used to analyse the blood flow with two-dimensional and three-dimensional models. These methods have never been used in literature before to simulate blood flow.

The main objectives of this thesis were to perform a static fluid flow analysis of blood using meshless methods, to study the blood flow behaviour in several benchmark situations and to compare the meshless' solution with the solution obtained with the Finite Element Method.

In order to achieve the proposed goals, several vessel geometries with different discretization levels were analysed. In this research work was proved that the meshless methods are a viable solution to simulate blood flow. However, it was found that the optimal NNRPIM and RPIM parameters for solid mechanics are not always suited for analysing fluids. Therefore, in the future, a deeper investigation concerning the determination of the optimal parameters for fluid flow analysis should be conducted. NNRPIM is particularly sensitive to the parameters used, because some parameters give atypical results.

In 3D studies, the FEM had better results in some cases. However, since the RPIM and NNRPIM require more computational power (which was not available), it is difficult to properly test new parameters and achieve better solutions.

In the comparison with benchmark cases, it was not possible to compare quantitatively the models, so it is difficult to validate the studied examples. It is also difficult to make fair comparisons because some parameters, such as dimensions of the models, are not shown in the papers.

This work had some limitations. Other rheological models for blood should have been tested. However, the parameters found in literature were not in the desired scale or could not be directly applied to the standard rheological laws included in FEMAS. The use of well-behaved geometries for the vessels is one of the limitations of the present study. Other geometries (such as real geometries coming from medical images) should have been studied. However, the imposition of the boundary conditions in such models is a very demanding task.

As mentioned before, the available computational power as limited the progression of this work. The hardware available only could process until around 4000 nodes, which influenced the analysis of models such as aneurysms and do convergence studies with 3D models.

In future works it could be studied the influence of the RPIM and NNRPIM parameters, attempting to achieve optimal parameters for fluid flow analyses. Additionally, it could be study models were the blood flow is more complex, such as low velocity zones leading to thrombus formation. In this work, the walls of the vessel were considered rigid. In the human body, the walls have mechanical properties that influence the blood flow, which wold be interesting to study. The influence of pulsate flow is another very important property of the cardiovascular system that was not studied in this thesis, but it wold be interesting to study.

References

- [1] A. Qiao and Y. Liu, "Medical application oriented blood flow simulation," *Clin. Biomech.*, vol. 23, no. SUPPL.1, pp. 130-136, 2008.
- [2] C. H. Hennekens, "Increasing burden of cardiovascular disease: current knowledge and future directions for research on risk factors.," *Circ.*, vol. 97, no. 11, pp. 1095-1102, 1998.
- [3] G. A. Mensah and D. W. Brown, "An overview of cardiovascular disease burden in the United States," *Health Aff.*, vol. 26, no. 1, pp. 38-48, 2007.
- [4] S. Mendis, P. Pekka, and B. Norrving, "Global Atlas on cardiovascular disease prevention and control," p. 155, 2011.
- [5] K. T. Delis, D. Bountouroglou, and A. O. Mansfield, "Venous Claudication in Iliofemoral Thrombosis: Long-term Effects on Venous Hemodynamics, Clinical Status, and Quality of Life," *Ann. Surg.*, vol. 239, no. 1, 2004.
- [6] R. MJ, C. BS, and H. Wheeler, "Long-term survival and quality of life following ruptured abdominal aortic aneurysm," *Arch. Surg.*, vol. 123, no. 10, pp. 1213-1217, Oct. 1988.
- [7] R. B. King, "Quality of Life After Stroke," *Stroke*, vol. 27, no. 9, p. 1467 LP-1472, Sep. 1996.
- [8] S. Yusuf, S. Reddy, S. Ôunpuu, and S. Anand, "Clinical Cardiology : New Frontiers Global Burden of Cardiovascular Diseases," pp. 2746-2753, 2001.
- [9] L. C. Sousa, C. F. Castro, and C. Conceic, "Blood Flow Simulation and Applications," vol. 1, pp. 67-86, 2012.
- [10] V. D. Butty, K. Gudjonsson, P. Buchel, V. B. Makhijani, Y. Ventikos, and D. Poulidakos, "Residence times and basins of attraction for a realistic right internal carotid artery with two aneurysms.," *Biorheology*, vol. 39, pp. 387-393, 2002.
- [11] G. Fortner and K. Johansen, "Abdominal Aortic Aneurysms," *West. J. Med.*, vol. 140, no. 1, pp. 50-59, Jan. 1984.
- [12] B. Lindblad, A. Eriksson, and D. Bergqvist, "Autopsy-verified pulmonary embolism in a surgical department: analysis of the period from 1951 to 1988.," *Br. J. Surg.*, vol. 78, no. 7, pp. 849-852, Jul. 1991.
- [13] D. A. Sandler and J. F. Martin, "Autopsy proven pulmonary embolism in hospital patients: are we detecting enough deep vein thrombosis?," *Journal of the Royal Society of Medicine*, vol. 82, no. 4. pp. 203-205, Apr-1989.
- [14] E. Previtali, P. Bucciarelli, S. M. Passamonti, and I. Martinelli, "Risk factors for venous and arterial thrombosis," *Blood Transfus.*, vol. 9, no. 2, pp. 120-138, 2011.
- [15] S. B. Miniño, AM Heron MP, "Deaths: Preliminary Data for 2004.," *Natl. Vital Stat. Reports.*, vol. 54, no. 19, pp. 1-49, 2006.
- [16] R. Vinoth, R. Adhikari, and D. Kumar, "Computational simulation of blood flow in normal and diseased artery: A review," *Indian J. Sci. Technol.*, vol. 9, no. 15, pp. 1-15, 2016.
- [17] K. B. Chandran, A. P. Yoganathan, and S. E. Rittgers, *Biofluid Mechanics. The Human Circulation*, 1st ed. Boca Raton: CRC Press, 2007.
- [18] D. Rubenstein, W. Yin, and M. D. Frame, *Biofluid Mechanics: An Introduction to Fluid Mechanics, Macrocirculation, and Microcirculation*. Elsevier Academic Press, 2012.
- [19] T. Sochi, "Non-Newtonian Rheology in Blood Circulation," *arXiv Prepr. arXiv1306.2067*, p. 26, 2013.
- [20] O. K. Baskurt and H. J. Meiselman, "Blood Rheology and Hemodynamics," *Semin. Thromb. Hemost.*, vol. 29, no. 5, pp. 435-450, 2003.
- [21] B.-K. Lee, S. Xue, J. Nam, H. Lim, and S. Shin, "Determination of the blood viscosity and yield stress with a pressure-scanning capillary hemorheometer using constitutive models," *Korea-Australia Rheol. J.*, vol. 23, no. 1, p. 1, 2011.

- [22] B. Das, P. C. Johnson, and A. S. Popel, "Computational fluid dynamic studies of leukocyte adhesion effects on non-Newtonian blood flow through microvessels.," *Biorheology*, vol. 37, no. 3, pp. 239-258, 2000.
- [23] J. Jung, R. W. Lyczkowski, C. B. Panchal, and A. Hassanein, "Multiphase hemodynamic simulation of pulsatile flow in a coronary artery," *J. Biomech.*, vol. 39, no. 11, pp. 2064-2073, 2006.
- [24] E. W. Errill, "Rheology of blood," *Physiol. Rev.*, vol. 49, no. 4, p. 863 LP-888, Oct. 1969.
- [25] A. Qiao, Z. Gu, and X. Meng, "Simulation of hemodynamics in bypassed aortic dissection," *2nd Int. Conf. Bioinforma. Biomed. Eng. iCBBE 2008*, pp. 1851-1854, 2008.
- [26] S. Applications, "Biofluid dynamics."
- [27] O. C. Zienkiewicz and R. L. Taylor, *The finite element method: solid mechanics*, vol. 2. Butterworth-heinemann, 2000.
- [28] O. Pironneau, "Finite element method for fluid," vol. 1988, p. 176, 1988.
- [29] T. J. Chung, *Finite element analysis in fluid dynamics*. McGraw-Hill International Book Co., 1978.
- [30] R. Temam, *On the theory and numerical analysis of the Navier-Stokes equations*, vol. 2. University of Maryland, Dept. of Mathematics, 1973.
- [31] J. D. Anderson, *Modern Compressible Flow: With Historical Perspective*. McGraw-Hill Education, 2003.
- [32] O. AXELSSON, V. A. BARKER, O. AXELSSON, and V. A. BARKER, "CHAPTER 2 - Variational Formulation of Boundary Value Problems: Part I," in *Finite Element Solution of Boundary Value Problems*, 1984, pp. 64-100.
- [33] K. Baba and M. Tabata, "On a conservation upwind finite element scheme for convective diffusion equations," *ESAIM Math. Model. Numer. Anal. - Modélisation Mathématique Anal. Numérique*, vol. 15, no. 1, pp. 3-25.
- [34] I. Babuska and W. C. Rheinboldt, "Error Estimates for Adaptive Finite Element Computations," *SIAM J. Numer. Anal.*, vol. 15, no. 4, pp. 736-754, 1978.
- [35] I. Babuška, "The p and h-p Versions of the Finite Element Method: The State of the Art BT - Finite Elements: Theory and Application Proceedings of the ICASE Finite Element Theory and Application Workshop Held July 28-30, 1986, in Hampton, Virginia," D. L. Dwoyer, M. Y. Hussaini, and R. G. Voigt, Eds. New York, NY: Springer New York, 1988, pp. 199-239.
- [36] G. K. Batchelor, *An Introduction to Fluid Dynamics*. Cambridge University Press, 2000.
- [37] Z. El Zahab, "Meshless Hemodynamics Modeling and Evolutionary Shape Optimization of Bypass Grafts Anastomoses," University of Central Florida, 2008.
- [38] Z. El Zahab, E. Divo, and A. J. Kassab, "A localized collocation meshless method (LCMM) for incompressible flows CFD modeling with applications to transient hemodynamics," *Eng. Anal. Bound. Elem.*, vol. 33, no. 8-9, pp. 1045-1061, 2009.
- [39] A. J. Katz, "Meshless Methods for Computational Fluid Dynamics," no. January, p. 131, 2009.
- [40] J. Belinha, *Meshless Methods in Biomechanics: Bone Tissue Remodelling Analysis*, vol. 2. 2014.
- [41] J. Belinha, L. M. J. S. Dinis, and R. M. N. Jorge, "The natural neighbour radial point interpolation method: dynamic applications," *Eng. Comput.*, vol. 26, no. 8, pp. 911-949, 2009.
- [42] O. C. Zienkiewicz, Y. C. Liu, and G. C. Huang, "Error estimation and adaptivity in flow formulation for forming problems," *Int. J. Numer. Methods Eng.*, vol. 25, no. 1, pp. 23-42, Jan. 1988.
- [43] Y. P. Chui and P. A. Heng, "A meshless rheological model for blood-vessel interaction in endovascular simulation," *Prog. Biophys. Mol. Biol.*, vol. 103, no. 2-3, pp. 252-261, 2010.
- [44] F. Yilmaz and M. Y. Gundogdu, "A critical review on blood flow in large arteries; relevance to blood rheology, viscoisty models and physiologic conditions," *Kore-Australia Rheol. J.*, vol. 20, no. 4, pp. 197-211, 2008.
- [45] "Fluid Flow." [Online]. Available: http://www.learneasy.info/MDME/MEMmods/MEM23006A/fluid_mech/lab-windtunnel.html. [Accessed: 04-Feb-2017].
- [46] L. Wexler, D. H. Bergel, I. T. Gabe, G. S. Makin, and C. J. Mills, "Velocity of blood flow in normal human venae cavae.," *Circ. Res.*, vol. 23, no. 3, pp. 349-359, 1968.
- [47] "Flow in pipes and around objects." [Online]. Available:

- http://www.bg.ic.ac.uk/research/k.parker/homepage/Mechanics_of_the_Circulation/Chap_05/_Chapter_05.htm. [Accessed: 18-Jun-2017].
- [48] M. W. Siebert and P. S. Fodor, "Newtonian and Non-Newtonian Blood Flow over a Backward-Facing Step - A Case Study," *Proc. COMSOL Conf. 2009 Bost.*, 2009.
- [49] L. He and J. Pan, "Hemodynamics simulation of the intracranial bifurcation vessel with different shape," *Proc. - 2010 3rd Int. Conf. Biomed. Eng. Informatics, BMEI 2010*, vol. 1, no. Bmei, pp. 298-301, 2010.
- [50] F. Pico, J. Labreuche, I. Gourfinkel-An, and P. Amarenco, "Basilar artery diameter and 5-year mortality in patients with stroke," *Stroke*, vol. 37, no. 9, pp. 2342-2347, 2006.
- [51] C. Cantu, M. Yasaka, T. Tsuchiya, and T. Yamaguchi, "Evaluation of the Basilar Artery Flow Velocity by Transcranial Doppler Ultrasonography," *Cerebrovasc. Dis.*, vol. 2, no. 6, pp. 372-377, 1992.
- [52] M. Razzaq, H. Damanik, J. Hron, A. Ouazzi, and S. Turek, "FEM multigrid techniques for fluid-structure interaction with application to hemodynamics," *Appl. Numer. Math.*, vol. 62, no. 9, pp. 1156-1170, 2012.
- [53] N. F. Mohammad, M. N. Nassriq, B. Electronic, E. Program, and M. E. Program, "Analysis of Blood Flow , Pressure and Velocity in a Stented Abdominal Aortic Aneurysm Model," no. October, pp. 11-13, 2009.